Title
Studies on Irradiation and Electric Potential Effects toward Mineral Atomic Structure and Chemical Reactivity

Author
Hsiao, Yi-Hsuan

Publication Date
2019

Peer reviewed|Thesis/dissertation

UNIVERSITY OF CALIFORNIA

Los Angeles

Studies on Irradiation and Electric Potential Effects toward Mineral Atomic Structure and Chemical Reactivity

A dissertation submitted in partial satisfaction of the

requirements for the degree Doctor of Philosophy

in Civil Engineering

by

Yi-Hsuan Hsiao

2019

ABSTRACT OF THE DISSERTATION

Studies on Irradiation and Electric Potential Effects toward Mineral Atomic Structure and Chemical Reactivity

by

Yi-Hsuan Hsiao

Doctor of Philosophy in Civil Engineering

University of California, Los Angeles, 2019

Professor Mathieu Bauchy, Co-Chair

Professor Gaurav Sant, Co-Chair

First, we focus on the effect of neutron irradiation on the durability of silicate and carbonate mineral aggregates. Comparisons of mineral dissolution rates, as a function of pH, temperature, or surface potential, were performed at pristine or Ar^{+} ion irradiated state. The experimental results were coupled with MD simulations of atomic scale alteration in the crystallographic structure of the mineral and any resulting changes in physical properties that result. In detail, albite ($NaAlSi_3O_8$), a 3D framework silicate, is compared with a less polymerized silicate (i.e., almandine) and carbonates (e.g. calcite, and dolomite), which are also often present in the mineral aggregates that compose concrete. When exposed to radiation, the crystal structures of minerals have possibilities to undergo significant alterations. These alterations may perhaps enhance its chemical durability, and thus degrade the infrastructure

durability. This relatively higher enhancement in the dissolution rate of silicates compared to carbonates following irradiation has significant impacts on the durability of concrete containing them up on their exposure to radiation in nuclear power plant environments.

Second, the effect of electric potential to calcite dissolution kinetics is examined. The accelerated ion transportation by potential further enhances calcite dissolution, whereas the extent of induced dissolution depends on the pH, ionic strength, and temperature. Calcite dissolution rate is enhanced in acidic to neutral pH solution, but remains constant in alkaline pH. From this, it reveals that the potential-induced dissolution rates are governed by the rate-limiting step in the dissolution mechanism. In addition, by varying solution ionic strength, stronger ionic strength results in less dissolution rate enhancement due to the lower ion diffusivity. As from the examination of the temperature effect, the potential-induced dissolution rate enhancement shows that electric potential does not increase calcite dissolution rate significantly compared to temperature.

In sum, it can be concluded that the mineral chemical reactivity can be enhanced by introducing external stimulus, and the magnitude of the rate enhancement depends highly on the solid atomic structure and the solvent properties. The conclusion and proposed future perspective of these works can be helpful to enhance the durability of concrete infrastructures and the relevant engineering applications.

The dissertation of Yi-Hsuan Hsiao is approved.

Scott Joseph Brandenberg

Mark S. Goorsky

Dwight Christopher Streit

Mathieu Bauchy, Committee Co-Chair

Gaurav Sant, Committee Co-Chair

University of California, Los Angeles

2019

To my parents and family,

for their love, endless support and encouragement

TABLE OF CONTENTS

LIST OF FIGURES

LIST OF TABLES

ACKNOWLEDGEMENT

My Ph.D. study in UCLA would not be accomplished without the guidance, support, and companionship from my lovely family, advisors, colleagues and the other supporters. I want to thank all the people who substantial my faith and guide my research in the last four years.

My first acknowledgement goes to my Ph.D. advisors, Professor Gaurav Sant and Professor Mathieu Bauchy, for their guidance, mentorship, and help over the past 4 years. Their continued mentorship has not only transformed me into a skilled scientific researcher, but also an individual that can communicate effectively and think critically. The work presented in this dissertation would not be possible without their continuous support.

Furthermore, I'd like to express my gratitude to Professor Scott Brandenberg, Professor Mark Goorsky, and Professor Dwight Streit for serving as my committee members for my qualifying exam and dissertation defense. Their guidance and suggestions have been valuable for the completion of this dissertation.

I appreciate the help of current and past members in Laboratory for the Chemistry of Construction Materials (LCC) and Physics of AmoRphous and Inorganic Solids Lab (PARIS). I would like to specifically thank Dr. Erika Callagon La Plante, Dr. Xin Chen, and Dr. Isabella Pignatelli, who were very patient to guide me through scientific research. To Shiqi, thank you for the companionship in the lab, I enjoyed sharing our personal lives and the discussions regarding mineral dissolution during our Ph.D. study.

In addition, I am really fortunate to have so many fantastic friends either in US or back in Taiwan, thank you for all for the support and companionship. First, I would like to thank Linda and Leah for hosting me when I first arrived LA from San Diego. To great people I met in UCLA, Chia-Yin, Sandy, Iris, Shin-Hung, Sheng-Yung, Ting-Chiang, Yu-Sheng, Yueh-Ning,

Hui-Ying, Chiao, Nonnon, thank you for all the coffee break, companies, bad jokes and support. To other friends from USC, thank you for inviting me to all the great parties, escape room experiences and BBQ. To all my friends in Taiwan (Wan-Ting, Vanessa, Candice, Virginia, Ching, Rita), thank you for all the encouragement, and did not abandon me when I am far away. Wen-Feng, who always has my back whenever I encounter difficulties or tough decisions, thank you for all the companionship, and for tolerating my temper or negative energy.

Finally, this dissertation is dedicated to my wonderful family. To my parents, thank you for all the love and support; I would not be able to become who I am today without what you have provided. To my sister Stephanie, thank you for all the cosmetics, clothes and mental support, which makes me still feel like a young girl during my busy Ph.D. life. I am sincerely delighted to be in this family, and the completion of this dissertation would not have been possible without their love.

VITA

2013	B.S., Materials Science Engineering
	National Tsing Hua University (NTHU)
	Hsinchu, Taiwan
2014	M.S., Materials Science Engineering
	University of California, San Diego (UCSD)
	La Jolla, CA
2019	Ph.D. Candidate, Civil and Environmental Engineering
	University of California, Los Angeles (UCLA)
	Los Angeles, CA

PUBLICATIONS AND PRESENTATIONS

E.C. La Plante, T. Oey, **Y.H. Hsiao,** L. Perry, J. W. Bullard, G. Sant, Enhancing Silicate Dissolution Kinetics in Hyperalkaline Environments. *J. Phys. Chem. C* (2019) 123, 6, 3687-3695.

Z. Wei*, **Y.H. Hsiao*,** X. Chen, E.C. La Plante, I. Mehdipour, D. Simonetti, N. Neithalath, L. Pilon, M. Bauchy, J. Israelachvili, G. Sant, Isothermal Stimulation of Mineral Dissolution Processes by Acoustic Perturbation. *J. Phys. Chem. C* (2018) 122, 50, 28665-28673. *(*Equal-contribution authors)*

Y.H. Hsiao, E.C. La Plante, N.M.A. Krishnan, H. A. Dobbs, Y. Le Pape, N. Neithalath, M. Bauchy, J. Israelachvili, G. Sant, Role of Natural Electrochemical Surface Potential and Irradiation Induced Disordering on Garnet-type Almandine Dissolution. *J. Phys. Chem. C* (2018) 122, 17268-1727.

Y.H. Hsiao, E.C. La Plante, N.M.A. Krishnan, Y. Le Pape, N. Neithalath, M. Bauchy, G. Sant, Effects of Irradiation on Albite's Chemical Durability. *J. Phys. Chem. A* (2017) 121, 7835-7845.

T. Oey, **Y.H. Hsiao,** E.C. La Plante, B. Wang, M. Bauchy, G. Sant, Rate Controls on Silicate Dissolution in Cementitious Environment. RILEM Technical Letters (2017) 2, 67-73.

Y.H. Hsiao, B. Wang, I. Pignatelli, N.M.A. Krishnan, Y. Le Pape, N. Neithalath, M. Bauchy, G. Sant, The Effect of Irradiation on the Atomic Structure and Chemical Durability of Calcite and Dolomite. (Submitted to *npj* Materials Degradation)

Y.H. Hsiao, E.C. La Plante, X. Chen, M. Bauchy, G. Sant, Electric Potential-induced Dissolution Kinetics of Calcite in Salt Solutions. (In preparation)

Chapter 1 Introduction

1.1. Motivation and Background

Concrete is used for the construction of nuclear power plants (NPPs), e.g., the containment building, biological shielding and spent-fuel handling buildings, in particular. NPPs, which is more than 40 years and beyond, is expected to be affected by concrete degradation that may definitely reduce its functionality and infrastructure durability. [1–3] Concrete, the primary support structure for the infrastructure, is exposed to neutron radiation during normal operation in nuclear power plant (NPP). During operation, the interaction of neutron irradiation with the concrete's constituents may cause degradation of the concrete performance, as emphasized by a review of concrete properties in nuclear power plant (NPP) environments. Neutron irradiation may cause amorphization of the crystalline components of concrete, i.e., mineral aggregates, or volume alteration, which are typically expansive in nature. Volume expansion can generate tensile or compressive stresses within concrete which can induce microcracking and/or result in debonding of aggregate with the matrix. On the other hand, atomic structural disordering can further result in alteration in the chemical stability of the phase in highly alkaline aqueous environments, which is suggested as the same conditions as pore solution in cement paste.

A recent report of the U.S. Nuclear Regulatory Commission/Department of Energy has identified irradiation effects, alkali-silica reaction (ASR) or alkali-carbonate reaction (ACR) as two of the major key degradation mechanisms that require priority research in the context of license renewals. [4] ASR/ACR gels are generated due to the progressive dissolution of reactive aggregates into the concrete's caustic pore solution (pH> 13) and the continuous water hydration of the gels. Following aggregate dissolution, precipitated hydrates that are rich in alkaline ions, water and silica, ASR gels with varying compositions are formed. This hydrate upon formation

within the concrete's or aggregates porosity, can result in deleterious microcracking, and the loss of mechanical properties due to internal volume expansion.

Although there are several past and ongoing studies, [5–9] comprehension of the effects of irradiation on the chemical stability properties of aggregates inside the concrete remains very limited. Mineral aggregates used in concrete are often composed of fragments of rocks including: granite or limestone, whose constituents include aluminosilicates and carbonates, respectively. As per the Streckeisen diagram, [10] granites can contain between 20–60% of quartz (SiO_2). On the other hand, limestone is mainly composed of calcite and minor amounts of clay and/or dolomite. Though the reactivity of quartz are shown to be affected by radiation heavily from previous studies, [11] the dissolution behavior of other aluminosilicates and carbonate minerals before and following irradiation are still unidentified.

Irradiation damage caused to minerals, by neutrons or, analogously, heavy-ions such as Ar^+ ions has been noted to be similar. [12, 13] Such damages have been described as the so-called "cascade" models wherein interactions between irradiated ions and mineral atoms cause the displacements of the primary knock-on atoms (PKAs). As these atoms absorb sufficient kinetic energy from the incident atoms, they generate "displacements cascades" consecutively [14] within the atomic network. While the deposited energy imparted into the system reaches a threshold value, amorphization localizes and causes the atomic disordering. Disordering indicates the formation of defects and imperfections in initially crystalline mineral structures including the random movement of atoms to positions far removed from their original positions, due to collision from the incident atoms. Following irradiation, the crystal structure of mineral can progressively lose its structural periodicity. [15–17]

Evidence demonstrating that radiation-induced volumetric expansion of concrete aggregate and the ASR process are the major source of damage in the concrete degradation. [18, 19] Such mechanical damage resulting from the expansion affects the structural properties of the concrete more intensely than direct irradiation effects on the concrete itself. The effects of radiation damage on silicates and carbonates (i.e., common minerals in aggregates in concrete) have been described in terms of changes in chemical reactivity and atomic structure (i.e., physical properties related to volume density). [20–22] Of these, both chemical instability and the volume change are thought to be prominent in silicates, but less significant for carbonates even for higher neutron fluence from literature. [23] However, the conclusion for the aggregate selection for NPP environments needs to be further confirmed by various compositions for silicate or carbonate minerals.

Broadly speaking, the disordering or the amorphization of mineral aggregates is expected to result in (1) volume changes of mineral aggregates, [24, 25] and (2) increases in chemical reactivity of mineral aggregates. [6, 7] These effects would be problematic in the context of concrete durability as the mechanical degradation of concrete due to microcracking of the binding cement paste matrix, and the chemical degradation of the concrete due to the onset of alkali-silica reaction (ASR). Therefore, this work elucidates how irradiation alters the chemical reactivity and the atomic structures of both silicate and carbonate minerals that are commonly used as aggregates in concrete. Focus is placed on contrasting how irradiation may or may not influence the chemical reactivity of a mineral with aqueous solutions, quantified in terms of its dissolution rate in nanoscale. The outcomes have significant implications on specifying radiation resistant aggregates for use in NPP concretes, and for assessing the risk-profiles of which

concretes and hence NPPs may be possibly more sensitive, to radiation-induced damage, than others.

1.1.1. Materials Selection

Minerals were selected on the basis of their abundance in common technical aggregates used in concrete in the U.S. (Figure 1-1). These minerals include: calcite ($CaCO_3$) and dolomite ($CaMg(CO_3)_2$), which are the main constituents of carbonate rocks on the Earth's surface; quartz (SiO_2), which is one of the most common rock-forming minerals, and is found in rocks including sandstone, quartzite, granite, and gneiss, among several others; and albite ($NaAlSi_3O_8$) and anorthite ($CaAl_2Si_2O_8$), which are the end-members of the plagioclase group of minerals typical of magmatic and metamorphic rocks. Almandine ($Fe_3Al_2Si_3O_{12}$) is one of the end-members in garnet group, and occurs as porphyroblast in schists. The minerals albite, anorthite, dolomite, and almandine were obtained from Ward's Natural Science Company, whereas synthetic samples ("single crystals") of quartz (001) and calcite (100) surfaces were sourced from MTI Corporation.

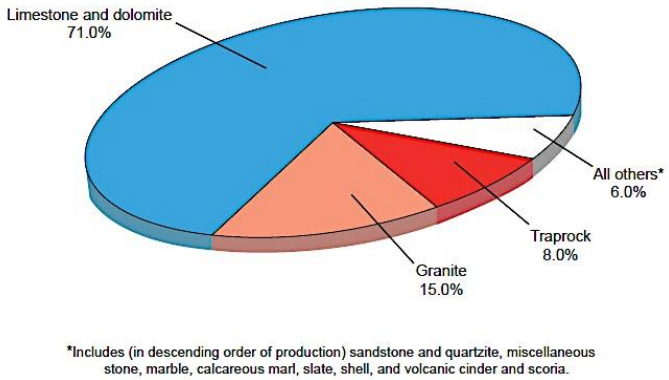

Figure 1-1: An illustration of the most common aggregates used in United States. (ASTM C125). [26]

1.2. Alkali-Silica Reaction (ASR) and Alkali-Carbonate Reaction (ACR)

The degradation of concrete by irradiation is not simply due to individual deteriorations of cement past and aggregates themselves, but due to the complex reactions between cement and aggregates. The decrease of concrete durability from nuclear radiation is strongly relating to the acceleration of alkali-aggregate reaction of concrete, or alkali-silica reaction (ASR) of siliceous aggregates in concrete, or alkali-carbonate reaction (ACR) of carbonaceous, by nuclear radiation. Since the ASR gels prevent the deformation of the aggregates, the expansion pressure generated by the penetration of the solution is accumulated in the aggregates. The accumulated pressure have possibilities to crack the aggregates and the surrounding concrete, as the pressure exceeds its maximum tolerance, which triggers the cracking propagation, and thus reduce the concrete life-time.

1.2.1. Alkali-Silica Reaction (ASR)

The alkali-silica reaction is the reaction of silica-rich aggregates with alkaline solution in the micropores of concrete, which is one of the main reactions causing severe deterioration of concrete. Due to the high volume of silica on earth such as quartz, fumed silica, and silicate minerals, it is used as one of the common aggregates in concrete. As the dissolved silicon ions from the silicate aggregates into high pH pore solutions in concrete, the deleterious and undesirable chemical reactions can take place, and gradually impact the concrete infrastructure by microcracking generation from the expansive reaction product (i.e., ASR gel).

In general, ASR mechanism can be discussed from two aspects: (1) the dissolution and precipitation reactions from silicate aggregates to form expansive ASR gels; and (2) the water absorption properties of expansion ASR gels. First of all, silica dissolution happens as the

reactive silica phases interact with high pH solvents, the hydroxyl ions (OH^-) from the liquid continuously attack the silicon oxygen bond (e.g. Si-O-Si, SiO_2 in aggregates) and therefore generate alkali silicate and silicic acid (i.e., Si-O-H bonds, hydration of SiO_2) on the silicate surface. [27, 28] The silicic acid is a weak acid, and therefore, it reacts with OH- rapidly and converts to alkali silicate, which can expand by hydration.

Previous studies have indicated that the dissolution rates of the majority silica phases increase with the activity of hydroxyl ions in solution, [29, 30] therefore, the silica dissolution rates increase with the solvent pH. In addition, the consumption of OH^- ions further leads to the dissolution of Ca^{2+} ions into the solution, even though a little amount of dissolved calcium or aluminum ions in pore solution reacts with hydrated SiO_2 gels to generate calcium silicate, as expressed in Equation (1-1). [31] Gaboriaud *et al.* [32] reported that calcium ions on the right-hand side of Equation (1-1) only acts as a catalyst and can be abandoned in the end of gelation reaction, following as Equation (1-2). Therefore, the siloxane bonds (e.g. Si-O-Si) form and the colloidal gels keep growing by continuous the condensation process of Si ions after the formation of ASR nuclei. [33] Figure 1-2 is the indication of the ASR gels formation in the cracking of concrete.

$$2((HO)_3 \equiv Si - O^-)_{aq} + Ca_{aq}^{2+} \leftrightarrow ((HO)_3 \equiv Si - O \cdots Ca \cdots O - Si(OH)_3)_{sol} \quad \text{Eq. (1-1)}$$

$$(\equiv Si - O \cdots Ca \cdots O - Si \equiv) + H_2O \leftrightarrow (\equiv Si - O - Si \equiv) + Ca^{2+} + 2OH^- \quad \text{Eq. (1-2)}$$

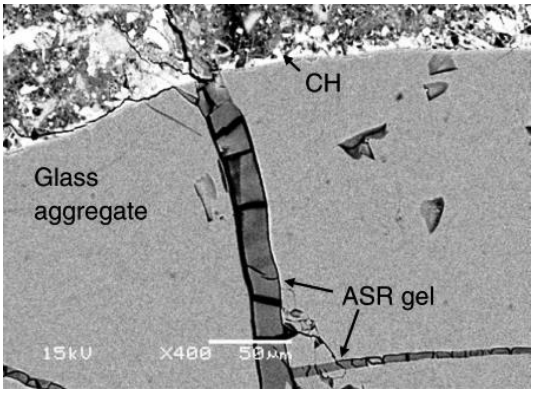

Figure 1-2: The ASR gels formed in the interior of aggregate crack. [34]

The expansion of silica gels is due to the absorption of large amount of water molecules, and the colloidal ions inside the ASR gels are weekly bonded, [34] therefore, the amorphous ASR gels are amorphous and lack of long-range ordered. The swelling properties of ASR gels as time could cause serious damage on the concrete by applying tensile stress and cracking. However, the mechanism of the gel swelling is still under investigated so far, although several models were proposed in the past few decades.

1.2.2. Alkali-Carbonate Reaction (ACR)

Alkali-carbonate reaction (ACR) is a combined reaction of deleteriously expansive ASR of cryptocrystalline quartz, and harmless dedolomitization of dolomitic aggregate. [35] Since ACR was first recognized and defined in 1957 in many cases of concrete deterioration due to such expandable gel formations were reported. [36] However, the expansion mechanism of the product of ACR are not fully understood. Up to now several theories have been proposed to explain the expansive force underlined this deleterious process. [37–39] The two noticeable explanations came from Gillott *et al.* who suggested that the absorption of water by clays of

newly exposed clay containing in reactive carbonate rocks are the main reason of the expansion, [37] who proposed that the formation and growth of brucite due to dedolomitization was expandable.

From previous studies, [40] it was suggested that the two reactions such as alkali-dolomite and alkali-magnesite reaction can cause expansion of concrete and specially prepared compacts. Microstructural study also showed that the microcracking was due to the formation and expansion of the reaction products from ACR in a confined space. The mechanisms of the two reactions and can be listed as follows:

(1) Alkali-dolomite reaction (ADR, i.e., dedolomitization):

$$Ca,Mg(CO_3)_2 + 2MOH = Mg(OH)_2 + CaCO_3 + M_2CO_3 \quad \text{Eq. (1-3)}$$

(2) Alkali-magnesite reaction (AMR):

$$MgCO_3 + 2MOH = Mg(OH)_2 + M_2CO_3 \quad \text{Eq. (1-4)}$$

, where M represents alkalis such as Na, K or Li that are common in concrete's pore solution. Although it is not suggested that all reaction products will attribute to the expansion, it is reasonable to assume that the acting part is proportion to the amount of reaction products formed. Therefore, the reaction as a whole will be correlated with the expansion.

Based on the investigation of the product expansion and the alkali-carbonate reaction, it is suggested that dedolomitization is expandable though it is a solid-volume-reducing process. [41] Similar to the case of ASR mentioned previously, it is reasonable to understand that the reaction in the interface between carbonate crystals and the surrounding liquid matrix in reactive carbonate aggregates will attribute to the expansion of concrete.

1.3. Mineral Dissolution Kinetics

1.3.1. Kinetics and Thermodynamic Relationship of Dissolution Reaction

Minerals with different solubilities may dissolve at different dissolution rates. Solubility and dissolution rate are thermodynamic and kinetic properties, respectively. The dissolution rate of the same mineral may either be transport-limited or surface controlled, depending on the solvent pH. The rate equation of the mineral dissolution process is proposed by Lasaga *et al.* [42] using the equation:

$$Rate = kA_{surf}(t)\,f(\Delta G) \qquad \text{Eq. (1-5)}$$

, where *Rate* is the overall dissolution rate of the reaction, k is the rate constant, A_{surf} is the surface area that is in contact with the solution during the dissolution process, and ΔG is the difference in Gibbs free energy between the material surface and dissolved ions in solution. From Equation (1-5), there are two parameters which cannot easily be determined: (1) the quantification of the surface area A_{surf} which involved in the reaction, and (2) the dependence of the dissolution rate on ΔG, since creating a surface area is associated with the changing Gibbs free energy. Therefore, there exists another proposed equation which can also describe the distance of reaction from equilibrium, using the parameter called chemical affinity (A). Chemical affinity (A) is the energy required to drive the reaction to from reactant to product, and is defined using Equation (1-6):

$$A = RT\ln(\frac{Q}{K}) = -RT\ln(\Omega) \qquad \text{Eq. (1-6)}$$

, where R is gas constant, T stands for temperature, and Ω represents the saturation index, which is equivalent to Q/K, which Q represents the activity quotient and K is the equilibrium constant for the reaction under a certain environment such as temperature, pressure…etc. In addition, Ω is less than 1 as the solution is undersaturated (i.e., mineral dissolving process), and becomes

greater than 1 when the solution is supersaturated, which will lead minerals to precipitate. Accordingly, chemical affinity (A) can be related to ΔG by adding a negative sign (i.e., $\Delta G = -A$). ΔG is the driving force or the energy for the reaction to process. Burch *et al.* [43] has fitted experimental data and proposed a model following the mineral dissolution process using two ΔG terms, as shown in Equation (1-7):

$$Rate = -k_1[1-\exp(-\frac{n\Delta G}{RT})^{m_1}] - k_2[1-\exp(-\frac{n\Delta G}{RT})^{m_2}] \quad \text{Eq. (1-7)}$$

, whereas Lasaga and Luttge *et al.* [44] modified Equation (1-7), which is able to take into account more factors:

$$Rate = v_\infty(1-\exp(\frac{\Delta G}{RT}))\tanh(\frac{1}{2x_s f(r_{pit})}) f(r_{pit}) \quad \text{Eq. (1-8)}$$

$$f(r_{pit}) = (1-\frac{1-\exp(-\frac{\sigma\bar{v}}{rkT})\exp(\frac{u(r)\bar{v}}{kT})}{1-\exp(\frac{\Delta G}{kT})}) \quad \text{Eq. (1-9)}$$

, where σ is the surface free energy and $u(r)$ is the strain energy at radius r, and $\bar{v}$ is the molar volume. The dissolution stepwave model proposed by Lasaga and Luttge *et al.* in 2001 used Equation (1-8) to indicate that rate-limiting step of crystal dissolution shifts from the creation of etching pits to the surface step growth for calcite. These variables are related to mineral itself and also the solutions.

1.3.2. Temperature Dependence of Reaction Rates

To extrapolate reaction rates, the temperature dependence of the rate constant must be understood. The Arrhenius equation is generally used to describe the temperature dependence of the rate constant (k): $k = B \exp(-E_a/RT)$. Here, B is referred to as the pre-exponential term, E_a is

the activation energy, R is the gas constant and T is temperature in degrees Kelvin. The slope of a plot of ln(k) versus 1/T for the dissolution yields the activation energy (E_a). In general, experimental activation energies for mineral-water reactions range from 10 kcal/mol to larger than 100 kcal/mol. Arrhenius proposed that the activation energy is the minimum amount of energy required to initiate a reaction. The magnitude of this activation energy is often interpreted with respect to the reaction mechanism. For example, activation energies for mineral dissolution that are as low as 10 kcal/mol have been interpreted to demonstrate reactions that are diffusion controlled, which its rate-limiting step is by the diffusion of reactants to the mineral or products away from the mineral. In contrast, activation energies of approximately 50 kcal/mol are generally represented as surface reaction controlled, which the dissolution process is determined by the bond-breakage during the atom detaching process.

In a dissolution process, a dissolved atom becomes displaced from the solid phase. The processes generally comprise multiple reactions or steps between solid and aqueous phase components. [45] The steps include transport processes (i.e., the displacement of dissolved atoms to the liquid phase) in addition to chemical reactions (i.e., the rupture of chemical bonds from the solid surface). The comprehensive dissolution mechanism at the mineral–water interface: (1) a hydrated ion approaching the solid surface via diffusion, (2) the hydrated ion may form a complex, (3) detaching the solid surface atoms by desorption, and (4) diffusing away from the solid–water interface. As outlined above, the macroscopic measurement of overall dissolution kinetics includes both physical transport steps and chemical reaction. [45] Formulation of rate laws should reflect the relative importance of transport versus chemical reaction if one or the other process is rate limiting. For example, dissolution rates of highly soluble and insoluble minerals tend to be relatively fast and slow, respectively. Dissolution of highly soluble minerals

therefore have a greater likelihood of becoming transport-limited as compared to low solubility minerals which are likely to be interface-limited.

1.3.3. Silicate Mineral Dissolution Mechanism

Besides quartz (SiO_2), An understanding of the dissolution of silicate minerals is necessary due to the high content of silicate minerals on the earth crust. The dissolution rate of feldspar minerals involves three successive steps: [46] (1) exchange of alkali or alkali earth ions by protons to form hydrogen feldspar, (2) the formation of alkali or alkali earth ions-depleted layer enriched in Si and/or Al, (3) slow dissolution of the residual layer at the interface. In addition, the solvent pH and dissolved ions in solutions determine the compositions and the concentrations of activated surface complexes, which are one of the rate-limiting factors in the last step.

The alkali depleted layers formed on the mineral surfaces due to their slower silicon/aluminum release as compared to cations during the dissolution process. After reaching steady state, as the ion diffusion times for the dissolved cations and Si ions to pass through the alteration layer are equivalent, the dissolution process becomes stoichiometric for silicate minerals. [46] Since the dissolution rate is generally determined by measuring the Si content in solution, the mechanism of breaking Si-O bond is relatively important. Although the dissolution process accompanies with the precipitation simultaneously, the hydrolysis of bridging oxygens (i.e., the oxygen connecting two silicon atoms) reduces the network of silicates, from Q4 to Q3 to Q2 and to Q1, so that the silicon atoms are able to release into the solution. [47, 48] The notation Q_i represents the occupied tetrahedral sites surrounding the silicon atom.

The dissolution rate of silica is related to the concentration of protons and hydroxyls within the solutions as expressed by:

$$r = k_H a_{H^+}^n + k_{OH} a_{OH^-}^m \qquad \text{Eq. (1-10)}$$

, where k_H and k_{OH} are rate constants for proton-promoted and hydroxyl-promoted dissolution respectively, a_i is the activity of species *i* in solution, and n and m stand for the partial orders of the reaction, which varies with the composition of the mineral. The effect of solvent pH can be interpreted as the sorption of H^+ on the oxide surface, which polarizes the bonding between metal atoms and oxygen, [49] thus the bonds connected to it will be weakened. From this point of view, the relationship between the silicate dissolution rates and the concentration of the positive and negative charged of the surface complexes (e.g. $[\equiv SOH_2^+]$ from proton adsorption and $[\equiv SO^-]$ from hydroxyl adsorption) can be calculated using the following equation:

$$r = k_H [\equiv SOH_2^+]^{q1} + k_{OH} [\equiv SO^-]^{q2} \qquad \text{Eq. (1-11)}$$

, where q_1, q_2 are fitting constants, and q_1 infers as the step numbers of protonation to release cations from the surface, and vice versa. To simplify, the value of q_1 is basically representing the metal oxidation number. From previous studies, the value of q_1 for albite ($NaAlSi_3O_8$) and anorthite ($CaAl_2Si_2O_8$) are suggested to be closed to 0.3. [50] As we increase the solvent pH to greater than 7, the enhancement in dissolution rate is due to the increasing density of the de-connected Al sites created by the hydroxyl adsorption. [50]

In general, the dissolution rates for silicates is lowest at the neutral solvent pH, which has a zero net surface charge (pH_{ppzc}). Equations (1-10) and (1-11) are widely used to calculate the dissolution rate, and also they provide a fundamental concept of the dissolution process that covers both acid and basic regime.

1.3.4. Carbonate Mineral Dissolution Mechanism

The influence of pH on the rate of dissolution of various carbonates (i.e., calcite, aragonite, witherite, magnesite and dolomite) has been well studied at room temperature using various reactors. In general, the carbonate dissolution rate dependence on pH observed for the simple carbonates is in agreement with the results observed for calcite and aragonite by Plummer *et al*. However, the rate of dissolution of magnesite is approximately four orders of magnitude lower than calcite, and that's the reason why dolomite ($CaMg(CO_3)_2$) has a lower dissolution rates.

For simple carbonates, Plummer *et al.* suggested that the following steps occur in parallel during the dissolution reaction: [51]

$$MCO_3 + H^+ \leftrightarrow M^{2+} + HCO_3^- \quad \text{Eq. (1-12)}$$

$$MCO_3 + H_2CO_3^* \leftrightarrow M^{2+} + 2HCO_3^- \quad \text{Eq. (1-13)}$$

$$MCO_3 \leftrightarrow M^{2+} + CO_3^{2-} \quad \text{Eq. (1-14)}$$

, where M represents the metal ion which can be Ca or Mg for calcite and dolomite, respectively. According to the stoichiometry of the three reaction steps and the thermodynamic constraints, the total forward and backward rates are expressed as:

$$R_f = k_1 a_{H^+} + k_2 a_{H_2CO_3^*} + k_3 \quad \text{Eq. (1-15)}$$

$$R_b = k_{-1} a_{M^{2+}} + k_{-2} a_{M^{2+}} a_{HCO_3^{2-}} + k_{-3} a_{M^{2+}} a_{CO_3^{2-}} \quad \text{Eq. (1-16)}$$

, where k_1/k_{-1}, k_2/k_{-2}, and k_3/k_{-3} are rate constants and a_i refers to the activity of the relevant species. These three reactions occur at the same time and the slowest reaction should therefore be rate-limiting. Importantly, as noted earlier, even under ambient conditions, calcite dissolution is

fast and can become transport controlled. At higher temperatures, different mechanisms may become important or the rate-limiting step may change.

1.4. Molecular Dynamic Simulation

1.4.1. Simulation Method

Realistic MD simulations of irradiation-induced damage in minerals were carried out in the open-source LAMMPS [52] package, following a well-established methodology. [53] First, a randomly chosen atom is accelerated with a kinetic energy equivalent to that of the targeted incident neutron, 600 eV in the present case. Weighted probabilities based on the neutron cross-sections of the respective elements (see Table 1-1) are considered when choosing the incident atom. The accelerated atom then collides with other atoms, thereby resulting in a ballistic cascade. Subsequently, a spherical region is created around the impacted zone, outside which atoms are kept at a constant temperature of 300 K by a Berendsen thermostat. [54] In contrast, the dynamics of the atoms inside the sphere is treated in the NVE ensemble to avoid any spurious effects of thermostat. A variable timestep is used during the ballistic cascade to avoid potential numerical errors associated with excessive collisions and overlapping of atoms; a timestep of 0.5 fs is used otherwise. The dynamics of the cascade is simulated for 15 ps, which was found to be sufficiently long to ensure the convergence of both temperature and energy. Finally, after each collision, the system is further relaxed in the NPT ensemble at 300 K and zero pressure for another 5 ps. This enables the system to adjust its density upon irradiation. This process is then repeated in an iterative fashion, with different knock-on atoms, until the system exhibits saturation in both enthalpy and density. Note that the damage produced by such

sequential irradiation is essentially similar to that of simultaneous particle irradiation, [55] such that the generality of the results is maintained.

Due to the large region that is affected during each ballistic cascade, large system sizes are required to avoid potential spurious self-interactions arising from the periodic boundary conditions. Herein, the system size was determined by repeatedly knocking each atom of the primitive cell, with the target radiation energy and in random directions. The study was conducted on all the different species of atoms present in the system. The maximum distances travelled by each of the impacted atoms were then recorded. Eventually, the size of the system was chosen to be at least twice as large as the maximum distance among all the recorded ones. It is worth noting that, to offer realistic results, MD simulations require the use of accurate inter-atomic potentials. In particular, in the case of irradiation simulations, the inter-atomic potential must correctly describe both the pristine and disordered structures of the relevant system with a fixed set of parameters. Although using a single "universal" potential would constitute an ideal option, such a potential is presently unavailable. Rather, each potential is specifically parametrized to optimally predict the properties of a family of materials. As such, for each family of aggregates, we selected the best available potential based on its ability to predict a realistic density, structure, and elastic tensor, both for the pristine mineral and its glassy counterpart. For quartz, we used the ReaxFF potential, with parameters taken from Manzano *et al.* [56] For other silicate minerals, a Buckingham potential parametrized by Teter was used, splined with ZBL potential to ensure realistic short-range repulsive interactions during the ballistic cascades (Table 1-2). [57] The carbonate minerals (calcite and dolomite) were simulated using the potentials from Raiteri *et al.*, [58] which were parameterized specifically for dolomite and calcite and which can simulate both the ordered and disordered phases.

Table 1-1: Neutron cross-sections of the elements found in the considered aggregate minerals.		
Sl. No.	**Element Name**	**Neutron cross-section (barn = 10^{-28} m2)**
1	Aluminum (Al)	1.35
2	Silicon (Si)	2.00
3	Sodium (Na)	3.15
4	Oxygen (O)	3.83
5	Calcium (Ca)	2.55
6	Magnesium (Mg)	3.91
7	Iron (Fe)	9.97
8	Carbon (C)	5.55

Table 1-2: Teter potential parameters for X–O interactions, where X= Si, Ca, Al, Mg, Na, Fe, O.					
Sl. No.	**Element**	**Charge**	**A (eV)**	**ρ (Å)**	**C (eV/ Å^6)**
1	Si	2.40	13702.910	0.194	54.681
2	Ca	1.20	7747.183	0.253	93.109
3	Al	1.80	12201.420	0.196	31.997
4	Mg	1.20	7063.491	0.211	19.210
5	Na	0.60	4383.756	0.244	30.700
7	Fe	1.20	19952.000	0.183	4.658
8	O	-1.20	2029.220	0.344	192.580

1.4.2. Results

1.4.2.1. Albite ($NaAlSi_3O_8$)

Albite is a tectosilicate mineral belonging to the tectosilicate feldspar family, which consists of Al and Si tetrahedra in the molar ratio of 1:3. Na^+ act as charge-balancing cations, leaving all O atoms in the structure as bridging oxygen (BO). The Si–O–Al and Si–O–Si bond angles are distributed in the ratio of 1:1. The evolution of density upon irradiation is plotted in Figure 1-3(a). During irradiation, albite exhibits a reduction in density from 2.61 g/cm^3 to 2.44 g/cm^3. Further, an investigation of the final irradiated structure of albite reveals a broadening in the distribution of the Si–O–Si bond angles. In contrast, the coordination numbers of Si and Al

are not significantly affected by irradiation. Hence, the overall increase of the volume primarily arises from the expansion of the silicate network, due to irradiation-induced disordering.

1.4.2.2. Anorthite ($CaAl_2Si_2O_8$)

Anorthite is the calcium-rich end-member of the feldspar family, which like albite is characterized by a framework silicate network. Since the amount of Al and Si atoms present in the mineral are equal, anorthite has alternate Al and Si tetrahedra connected by BO atoms to form a 3-D packed structure. Interestingly, anorthite exhibits a slight increase in density upon irradiation, as shown in Figure 1-3(b). This increase is not linked to any significant change in the short-range order (e.g., coordination number or bond length). However, as opposed to the pristine structure, we note the appearance of Si–O–Si and Al–O–Al bond angles upon irradiation, which results in a more compact structure.

1.4.2.3. Almandine ($Fe_3Al_2Si_3O_{12}$)

Almandine is a nesosilicate which consists of isolated SiO_4^{4-} tetrahedra connected by cations. Aluminum is present with an octahedral environment, i.e., connected to six O atoms. During irradiation, almandine exhibits a reduction of density, from 4.2 g/cm^3 to 3.4 g/cm^3, as shown in Figure 1-3(c). An analysis of the final structure revealed that all of the Al atoms underwent a transition from octahedral to tetrahedral coordination environments upon irradiation, which induces the observed expansion – since the tetrahedral structure features a lower packing fraction than the octahedral structure.

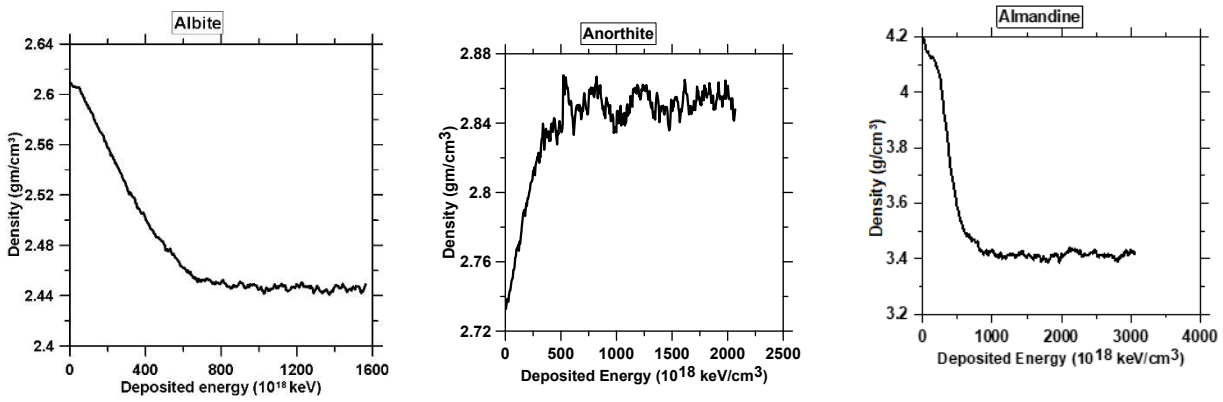

(a) **(b)** **(c)**

Figure 1-3: Evolution of the density of **(a)** albite, **(b)** anorthite **(c)** almandine under irradiation.

1.4.2.4. Calcite ($CaCO_3$)

Calcite belongs to the carbonate family of minerals, with an ionic bond between Ca atoms and CO_3 groups. As shown in Figure 1-4(a), calcite does not exhibit any notable change in density. This can be attributed to the non-directional nature of the ionic bonds, which, as such, can easily reorganize after irradiation. Although the final structure exhibits a slightly disordered nature as compared to that of the pristine calcite, we observe that the mineral remains largely unaffected by irradiation.

1.4.2.5. Dolomite ($CaMg(CO_3)_2$)

Dolomite, which belongs to the carbonate family, has a structure similar to calcite with alternate Ca atoms being replaced by Mg. The density of pristine dolomite is higher than that of calcite. Under irradiation we observed that similar to calcite, dolomite does not exhibit any notable changes in density (from 2.895 g/cm^3 to 2.863 g/cm^3), as shown in Figure 1-4(b).

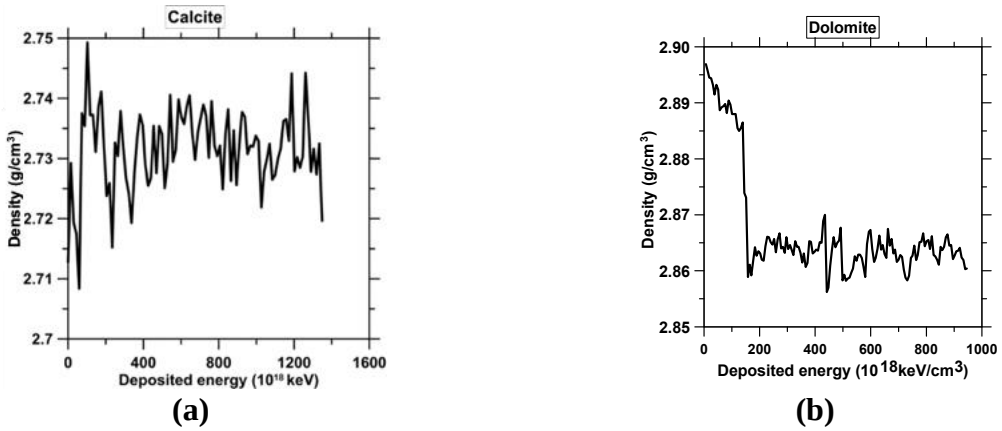

Figure 1-4: Evolution of the density of **(a)** calcite and **(b)** dolomite under irradiation.

We now assess the effect of irradiation on the atomic topology, which serves as an input for a model which enables predictions in changes in dissolution rate within the framework of topological constraint theory (TCT).

1.5. Topological Constraint Theory (TCT)

1.5.1. Calculation Method

TCT reduces complex atomic networks into simple trusses of nodes (atoms) connected by mechanical constraints (chemical bonds). As such, TCT captures the important atomic topology, while filtering out less relevant details that ultimately do not affect macroscopic properties. [59] Specifically, the rigidity of a network is assessed by determining the number of topological constraints per atom, n_c. In atomic networks, the constraints comprise the radial bond-stretching (BS) and angular bond-bending (BB) chemical atomic bonds, which maintain the bond lengths and angles fixed around their average values, respectively. As per Maxwell's stability criterion, [60] atomic networks can then be described as (1) flexible (n_c < 3), showing floppy internal modes of deformation, (2) stressed-rigid (n_c > 3), featuring eigenstress due to mutually

incompatible constraints, or (3) isostatic (n_c = 3), being rigid but free of eigenstress. Note that, here, the value "three" corresponds to the number of degrees of freedom per atom in a three-dimensional network.

Elucidating the effect of irradiation on the rigidity of the atomic network requires the enumeration of the number of constraints acting between the atoms. For fully a connected homogeneous network, the constraints enumeration is straightforward and depends only on the coordination number (CN, *r*) of each species. Thus, each atom features *r*/2 BS constraints, each constraint being shared by two atoms, and 2*r* – 3 BB constraints, which corresponds to the number of independent angles required to define a polyhedron. Therefore, the total number of constraints per atom n_c is given by:

$$n_c = \frac{< r >}{2} + 2 < r > - 3 \qquad \text{Eq. (1-17)}$$

, where <*r*> is the average coordination number of the atoms. In contrast, enumerating constraints in an irradiated mineral is complicated by the following difficulties: (1) A given species can feature various coordination numbers due to the formation of defects, [53] resulting in varying number of constraints for the same species, (2) the angular BB constraints, e.g., Si–O–Si bonds in quartz, are associated with lower energies than radial BS constraints, and, as such, can become broken upon irradiation. To tackle these issues, we enumerated the number of constraints by relying on MD simulations. This method is based on an inverse approach, wherein the trajectory of an atom is used to deduce the number of underlying constraints constraining its motion. The basic idea of this method is that an active constraint would maintain bond lengths or angles fixed around their average values, whereas a broken or missing constraint would allow large atomic motion. Hence, to obtain the number of BS and BB constraints acting on a given

atom, we estimate the radial and angular excursions of each of its neighbors, respectively.

1.5.2. Results

The constraints enumeration is first detailed for the case of quartz. The radial excursion of each neighbor was evaluated by computing the partial pair distribution functions (PDFs) of O and Si atoms, as well as the contributions of each neighbor 1, 2, ..., 6, where neighbors are ranked with respect to their distances from the central atom. Note that, here, the choice of the value 6 is arbitrary, although it must be large enough to ensure that it encompasses all potential constraints formed around a given atom. The radial excursions of the neighbors are then estimated from the second moments of these distributions. Such radial excursions, as computed in quartz, are plotted as a function of neighbor number N in Figure 1-5(a). We observe a clear shift from low to high radial excursions, which correspond to intact and broken BS constraints, respectively. As expected, the number of intact BS constraints corresponds here to the coordination of each species, i.e., 4 and 2 for Si and O, respectively. In a similar fashion, the angular excursion of each neighbor is evaluated by computing the partial bond angle distribution of each triplet of atoms (i, 0, j), where 0 denotes the central atom considered, and (i, j) all the 15 possible pairs formed among the 6 nearest neighbors. The angular excursion is then assessed by calculating the second moments of these distributions. Once again, as shown in Figure 1-5(b), we observe a clear jump between low and high angular excursions, which represent intact and broken BB constraints, respectively. Here, we find 1 and 5 intact BB constraints per O and Si, which fixed the inter- and intra-tetrahedral angles, respectively. Altogether, this method provides a robust and non-arbitrary enumeration of the number of constraints in quartz.

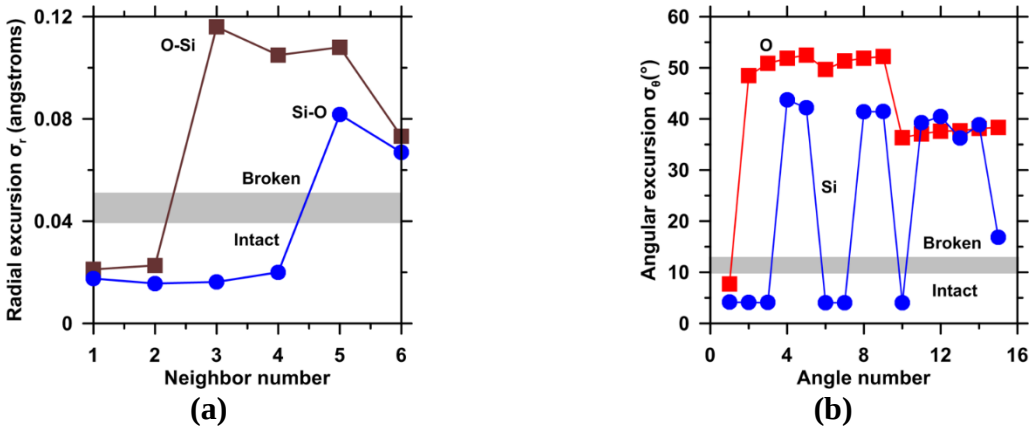

Figure 1-5: (a) Radial excursions of each neighboring atom with respect to central Si and O atoms. Note that intact and broken BS constraints are associated with significantly different (low and high, respectively) radial excursions. **(b)** Angular excursions around central Si and O atoms. Note that, as in the case of BS constraints, the angular excursions associated with intact and broken BB constraints significantly differ.

This methodology can be used to track the irradiation-induced variation in n_c, as shown in Figure 1-6. First, we observe that, upon irradiation, n_c decreases towards $n_c = 3$, which is the value expected for glassy silica, as the high glass transition temperature induces the breakage of the Si–O–Si BB constraints. Second, n_c is noted to cross the value of three at about 1.2×10^{21} keV/cm^3 deposited energy, which effectively separates a stress-rigid from a flexible domain. As shown in the inset in Figure 1-6, this transition arises primarily from the decrease in the number of angular BB constraints upon irradiation, which results from the breakage of Si–O–Si bonds, as well as a small fraction of O–Si–O BB constraints. This suggests that irradiation preferentially affects these weaker angular constraints, while it has little, if any, effect on the stronger radial Si–O BS constraints. Note that the trend in the evolution of n_c follows a similar trend as that of the density upon irradiation. Since n_c controls the reactivity of minerals, these results suggest

that fully irradiated quartz features a dissolution rate fairly similar to that of glassy silica.

Similar constraints enumerations were carried out for the other minerals considered herein. Overall, we observe that, in most cases, the radial BS constraints are unaffected by irradiation, except in the case of almandine, wherein the coordination number of Al atoms is reduced from 6 to 4, thereby reducing the number of active BS constraints. In silicate systems, Si–O–Si bond-bending constraints are found to become consistently broken upon irradiation, as in the case of quartz. In contrast, in carbonate minerals, all constraints (BS and BB) are found to remain intact, [11] so that no variations in n_c are observed. The calculated change in n_c (Δn_c) for all considered minerals are shown in Table 1-3. Interestingly, as shown in Figure 1-7, we observe a linear correlation between Δn_c and the relative variation of density upon irradiation. Note that the constraints that are broken upon irradiation (Δn_c) correspond to the "weaker constraints" of the networks, that is, those associated to a lower energy. This demonstrates that the number of weak constraints per atom, Δn_c, can be used as metric to predict the extent of irradiation-induced swelling.

Table 1-3: Variation of the number of constraints per atom upon irradiation (Δn_c).

Mineral	**Weak constraints per atom (Δn_c)**
Albite	-0.307
Anorthite	0.113
Almandine	-0.650
Quartz	-0.617
Calcite	0
Dolomite	0
Diopside	-0.388
Enstatite	-0.272

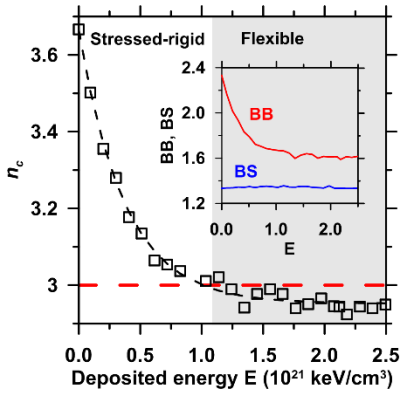

Figure 1-6: The evolution of the number of constraints per atom, n_c, in irradiated quartz as a function of the deposited radiation energy. The data are fitted by an exponential function. The dashed red line indicates the position of the rigidity transition ($n_c = 3$), which effectively separates the stressed-rigid from the flexible domain (shaded region). The inset shows the repartition of radial BS and angular BB constraints.

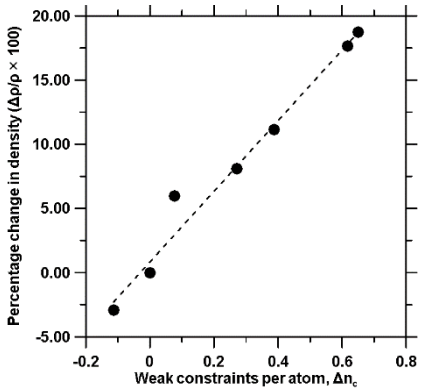

Figure 1-7: Percentage change in structural density of each mineral upon irradiation with respect to the corresponding weak constraints per atom.

Chapter 2 The Effects of Irradiation on Albite's Chemical Durability

2.1. Introduction and Background

Due to their widespread abundance, concrete – a mixture of cement, sand, stone (i.e., fine and coarse aggregates, respectively), and water – is often composed using siliceous mineral aggregates (e.g., granite). But, recent studies have shown that siliceous minerals such as quartz, upon exposure to radiation in the form of neutrons, may experience deleterious volume expansions, [6, 7, 11, 61] and reductions in their chemical durability – caused due to alterations, including disordering of their crystal structures. [6, 11, 62] This latter issue of compromised chemical durability is problematic as the progressive dissolution of silica from the aggregate into the concrete's pore-fluid – an alkali rich environment – has the potential to induce alkali-silica reaction (ASR) [63, 64] which degrades the mechanical integrity of the concrete. [34, 65] Both of these issues, i.e., of mineral aggregate expansion, or reductions in a mineral's chemical durability are problematic as they have the potential to compromise the mechanical integrity of concrete, and in turn, the safety and shielding functions of structures that are constructed thereof in nuclear power plants (NPPs). [6, 7, 11, 61]

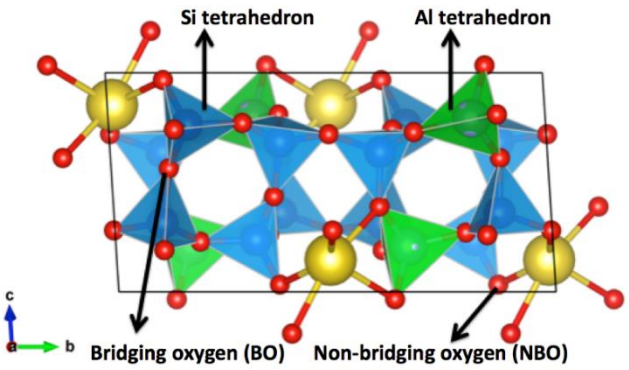

Figure 2-1: The crystal structure of albite ($NaAlSi_3O_8$) showing Si tetrahedra (blue), Al tetrahedra (green), Na atoms (yellow) and O atoms (red) visualized using VESTA. [66]

Albite ($NaAlSi_3O_8$; see Figure 2-1), a tectosilicate mineral of the plagioclase feldspar family is often found in siliceous aggregates (i.e., sand and stone) used to compose concrete including granite, rhyolite, etc. [67–69] Therefore, as part of a larger goal to examine the effects of irradiation on the chemical durability of minerals that compose siliceous aggregates, and therefore of concrete itself – this work seeks to quantify the extent to which, radiation exposure, and alterations in atomic structure induced therein, may alter albite's chemical reactivity (i.e., dissolution rate in alkaline, aqueous environments). [70, 71] As such, this work builds on the previous studies of Hamilton *et al*. [72] who showed that the dissolution rate of disordered albite may differ from that of crystalline albite, by up to a factor of 30 times in alkaline solutions. By a pioneering combination of nanoscale analytics based on vertical scanning interferometry (VSI) and molecular dynamics (MD) simulations, special focus is paid to reveal: (i) how radiation exposure may alter the atomic structure of albite, and its network connectivity, and, (ii) how changes in atomic structure correlate with alterations in mineral dissolution rates (chemical durability).

2.2. Materials and Methods

2.2.1. Sample Preparation

Natural (rock) albite samples were obtained from Ward's Natural Science Company. [73] The albite samples were sectioned using a low speed diamond saw (IsoMet™ 1000, Buehler Inc.). Following sectioning to a sample size on the order of 1 cm x 1 cm x 0.1 cm, the samples were embedded in a cold-cured inert acrylic resin (EpoxiCure Resin, PN 203430128: Buehler Inc.). The resin-embedded sample was then progressively mechanically polished using 600, 800 and 1200 grit SiC abrasives and diamond abrasion pastes (from 6 µm down to ¼ µm), and fixed on a THOR-LABS© kinematic mount to facilitate handling during the dissolution studies. After the final polishing step, the surface roughness of the pristine albite sample was assessed (using VSI, e.g., see Figure A for representative images) by the parameter, S_a, i.e., a measure of the absolute distances of the profile heights from a given central area which is written as, $S_a = \frac{1}{A}\iint_A |Z(x,y)|dxdy$, where, A is the actual surface area, and x,y are the corresponding lateral coordinates. Based on such analysis $S_{a,p} \approx 70$ nm for the pristine sample for a field of view (FoV) of 1.3 µm x 1.3 µm on the mineral surface.

Ar^+ implantation of planar, polished albite samples was carried out at the Michigan Ion Beam Laboratory (MIBL). [74] Ion-beam irradiations were performed at room temperature using an implantation energy of 400 keV with Ar^+-ions to a total fluence (dose) of 1.0 x 10^{14} ions/cm^2. Based on these implantation characteristics, the disordered mineral zone is estimated to be on the order of 600 nm deep, based on knowledge of albite's density, and calculations carried out using the Stopping and Range of Ions in Matter (SRIM) (see Figure 2-2). [75] SRIM is a widely used Monte Carlo simulation code that is often applied to predict the transport of ions in matter. [75]

It can also be used to calculate the magnitude of radiation damage (in terms of displacements per atom, dpa) that is caused by ion implantation to a material. Specifically, using as inputs the energy of the incident Ar^+ ions (400 keV), and the density (≈2.61 g/cm^3) and the composition of the target material (albite, $NaAlSi_3O_8$), SRIM can be used to calculate the concentration of incident ions as a function of depth. As compared to the penetration depth of Ar^+ ions in quartz under similar irradiation conditions, as determined using SRIM, [11] if the albite samples were assumed to be perfect single crystals (i.e., similar to single crystal quartz), the end-of-range of the implanted Ar^+-ions in albite is observed to exist 100 nm deeper than in quartz (i.e., the depth corresponding to the implanted depth is observed at 500 nm and 600 nm for quartz and albite, respectively). In a defected, impure albite sample as used in this study, the depth of the ion-implanted layer should be larger than 600 nm.

It should be noted that Ar^+ ion irradiation was selected rather than neutron irradiation because the former features more precise temperature and dose controls, and since both ion- and neutron-irradiation result in a similar end-state, i.e., in terms of their effects on altering a mineral's crystal structure. [12, 76] While the implanted samples were mounted on the resin as mentioned above, mechanical polishing of their surfaces after irradiation was not carried out so as to maintain the integrity of the disordered near-surface layer that forms following Ar^+ irradiation. The surface roughness of the implanted samples ($S_{a,i}$, nm) is found to be around 100 nm after irradiation within a FoV of 1.3 μm x 1.3 μm, similar to the case of pristine albite above. As such, it can be concluded that the surface roughness values of the pristine and irradiated samples are nominally similar.

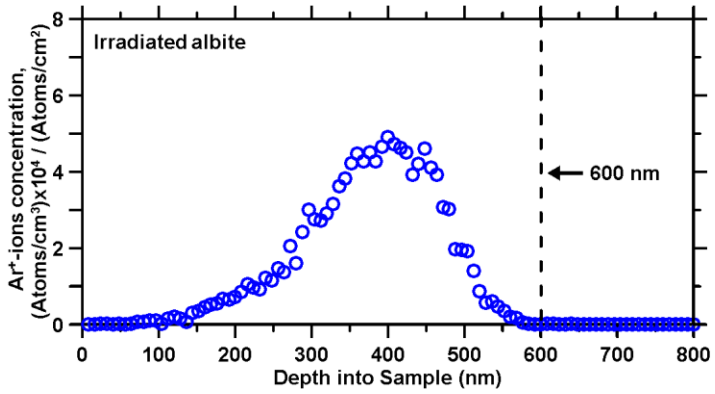

Figure 2-2: The implanted concentration of Ar^+-ions as the function of depth from the albite surface. The unit on the Y-axis ((atoms/cm^3)/(atoms/cm^2)) when multiplied by the implantation fluence (10^{14} ions/cm^2) reveals the concentration of implanted Ar^+-ions (atoms/cm^3) as a function of depth. This calculation assumes that the albite sample is a perfect (defect-free, stoichiometric) single crystal.

2.2.2. Scanning Electron Microscopy-Energy Dispersive X-ray Spectroscopy (SEM-EDS)

SEM imaging was carried out on albite particulates with an average diameter of around 20 μm as measured using static light scattering (SLS), see Figure 2-3(a). The particulates were gold-coated to a thickness of around 6-to-7 nm and then examined using secondary and backscattered electrons using a FEI Nova NanoSEM 230 (7 kV, 80 pA). The elemental composition (as simple oxides) of the sample as measured using SEM-EDS is given in Figure 2-3(b). On account of its natural origin, traces of Fe_2O_3 and K_2O (< 3.0 mass %) were detected in the albite, which may suggest the presence of muscovite impurities.[22] The field-of-view (FoV) selected was larger than 10000 μm^2, and the measurements were repeated at least 3 times, with > 10 sampling points in each measurement.

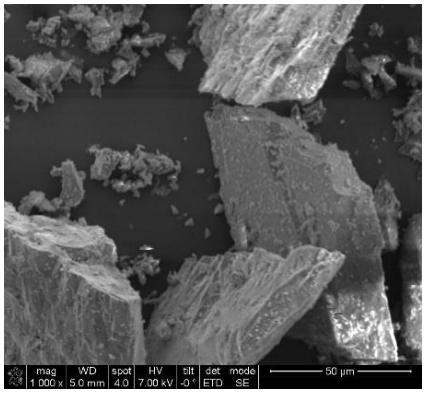

(a)

Simple oxide	Albite sample	Pure albite
	mass %	mass %
SiO_2	73.6 ± 0.9	68.7
Al_2O_3	14.7 ± 0.6	19.4
Na_2O	8.8 ± 0.5	11.8
Fe_2O_3	1.9 ± 1.0	-
K_2O	1.0 ± 0.2	-

(b)

Figure 2-3: (a) Representative SEM images of the albite particulates, and, **(b)** The (average) simple oxide composition of the albite samples as measured using SEM-EDS.

2.2.3. X-ray Diffraction (XRD)

The natural albite samples were finely powdered using an agate mortar and pestle – to ensure that 100 mass % passed through a 53 µm (No. 270) sieve – and then analyzed using powder X-ray diffraction (XRD). XRD patterns were recorded using a Bruker D8-Advance powder X-ray diffractometer in θ-θ Bragg-Brentano geometry, using Cu-K_α radiation (λ = 1.5406 Å) at an accelerating voltage of 40 kV, and a beam intensity of 40 mA. A 2θ range of 10° to 70°, a 2θ scan step size of 0.02°, and an exposure time of 0.5 seconds per step were used. The powdered samples were mounted on a rotating sample holder to acquire statistically averaged data, and the sample's surfaces were textured to minimize preferred orientation errors. The XRD pattern of the sample is qualitatively similar to that of albite reported in the literature [77] and by the International Centre for Diffraction Data (ICDD Code: 01-075-1142, [78] see Figure 2-4).

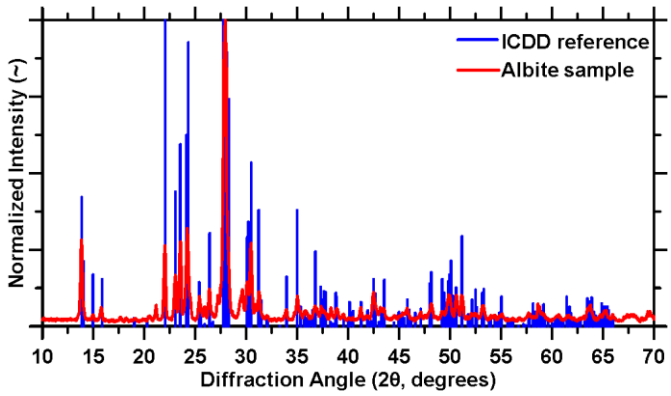

Figure 2-4: The X-ray diffraction patterns of the powdered albite sample shown alongside the ICDD reference for comparison.

2.2.4. Fourier Transform Infrared Spectroscopy (FTIR)

Fourier transform infrared spectroscopy (FTIR) was used to examine surface chemical bonds, and structural ordering in pristine and irradiated albite. Both pristine and implanted samples were analyzed using an attenuated total reflectance FTIR (ATR-FTIR; PerkinElmer Spectrum Two) at room temperature. Finely milled powders of pristine and irradiated albite (100 mass % passing a 53 µm sieve opening) were placed onto the sample holder that was provisioned with a pressure applicator (the applied pressure is on the order of 70 N), and a diamond/ZnSe composite crystal at an incidence angle of 90°. Prior to the measurements, a background measurement of the empty sample holder was collected. The powder sample was placed on the surface of ATR crystal and pressed by a lever to ensure tight and constant contact over the course of the measurement. Each spectrum acquired was the average of 4 scans in the range of 4000-450 cm^{-1} with a spectral resolution of 1 cm^{-1}. The influence of H_2O was subtracted automatically. Specific peak assignments were carried out within Spectrum v6.0 (PerkinElmer,

Waltham, MA) based on previous studies of silicate and aluminosilicate minerals and their specific vibrational modes. [79–81]

2.2.5. Measuring albite dissolution rates using vertical scanning interferometry (VSI)

The dissolution rates of albite were measured at 25 ± 3 °C, 45 ± 1 °C and 65 ± 2°C in NaOH solutions having concentrations of: 0.1 mM NaOH (pH 10), 10 mM NaOH (pH 12) and 100 mM NaOH (pH 13). The pH levels were selected to simulate conditions prevalent in ordinary portland cement (OPC) concrete which hosts a mature-state pH ≥ 12.5. [6, 61] This high pH in OPC environments originates from the presence of alkali ions such as potassium and sodium, which typically exist in an abundance that is up to one order of magnitude higher than calcium ions (e.g., on the order of 2-to-20 mM in mature systems). [82] Since the objective herein is to isolate the effect of pH on dissolution in OPC-like environments, adjusting the pH using NaOH is an appropriate selection. The NaOH pellets used were of ACS reagent grade, which were subsequently dissolved into Milli-Q deionized water (18 MΩ cm). The pH of the solutions was measured using a ThermoFisher Scientific Orion Versa Star Pro pH Benchtop Multiparameter Meter calibrated over the range $7 \leq pH \leq 14$ at the relevant measurement temperature.

To relate atomic-scale alterations and disordering resulting from irradiation to albite's chemical durability, the dissolution rates of pristine and ion-implanted albite samples were measured using vertical scanning interferometry (VSI). VSI offers the ability to acquire 3D-visualizations of reacting surface topographies with nanoscale vertical resolution (≈1-2 nm) over sample areas on the order of 10s of mm^2. Herein, a 50x Mirau objective was used (N.A. = 0.55) in the imaging, resulting in a lateral resolution of 163 nm wherein a single image field

encompasses a field of view (FoV) of 170 μm x 170 μm. For a stitched image grid consisting of A x B (where A = 10, and B = 3) images, the cumulative, lateral field of view (FoV) is on the order of 1236 μm x 441 μm, e.g., see Figure A. Importantly, by directly tracking the surface retreat (i.e., change in height vis-à-vis an unchanging reference) following immersion in a solution as a function of time, VSI can be used to precisely measure the dissolution rate of a solid. [70, 71] This technique has significant advantages over other methods that are based on the analysis of solution compositions. For example, dissolution rates obtained from VSI do not require normalization to the surface area of the reacting solid. Furthermore, VSI measures the surface retreat rates, which can be directly related to molar dissolution through the molar volume, while being indifferent to the fate of dissolved species, and the stoichiometry therein (e.g., due to potential incongruency in dissolution, etc.).

The imaging was carried out such that a "reference area" on the albite surface was covered with an inert silicone mask (Silicone Solutions SS-38). [83] As a result, the masked area remains unaffected upon contact with the solution, while the unmasked area dissolves – thereby showing a reduction (retreat) in height. Dissolution rates were quantified using a procedure wherein a plane, polished albite sample was submerged in a static solution over a period of time – resulting in a liquid-to-solid ratio (l/s, mass basis) of around 500. In other words, the solvent (50 ml) contacted a surface with a nominal area of 10 mm x 5 mm resulting in a surface (solid)-to-volume (liquid) ratio of 0.001 mm^{-1} (S/V). Due to the very slow dissolution rate of albite (i.e., estimated to be on the order of 10^{-4} $\mu mol/m^2/s$ at pH 12), [84] and the high-dilution level, the pH and composition of the solution (i.e., the undersaturation level), [85] and in turn, albite's dissolution rate is not greatly affected by ongoing dissolution (see discussion below). Before contact with the solution ('time-zero' image), and after pre-defined solution contact times, the

albite's surface was imaged using VSI. Special care was taken to: (i) evacuate any residual solution from the albite surface by exposure to a stream of compressed N_2 prior to imaging, and, (ii) minimize contact of the immersion solution with CO_2 in air which could alter its pH due to carbonation.

The VSI images thus acquired after nulling the surfaces were analyzed in Gwyddion (version 2.47) [86] to assess the change in height of the dissolving surface, with respect to the unchanging reference as a function of the time. The change in height as a function of time ($\Delta h/\Delta t$, nm/h) when normalized by the molar volume of albite yields its molar dissolution rate. Dissolution rates determined in this manner are expected to have a maximum uncertainty of up to 10%, due to the various sources of uncertainty and variability inherent in the VSI measurements, e.g., low-frequency vibrations that may not be fully damped by the vibration isolation system, or the effects of temperature variations in the environment.

Intermittently over the course of the VSI measurements, selected immersion solutions were analyzed in terms of their elemental compositions using inductively coupled plasma optical emission spectrometry (ICP-OES; Perkin Elmer Avio 200) for species including: Na, Si, and Al. Ion speciations in solutions with the measured compositions were subsequently calculated in PHREEQC© [87] to determine the degree of undersaturation of the solution with respect to albite (i.e., quantified in terms of the change in the Gibbs free energy that results with increasing dissolution, over time, $\Delta G_d = RT\ln[IAP/K_{sp}]$ in kJ/mol, where R is the gas constant, T is temperature in K, IAP is the ion-activity product, given by $IAP = ([Na^+][Al^{3+}][H_4SiO_4]^3)/[H^+]^4$, and K_{sp} is the solubility product of albite at the relevant temperature and atmospheric pressure). [33] This equation was used to calculate ΔG_d and confirm that the dissolution rates represented

"far-from-equilibrium" conditions and that they were thus unaffected by the presence of ions in solution that are released from the progressive dissolution of albite. [88–91]

2.3. Results and Discussion

2.3.1. Albite dissolution rates

The dissolution rates of pristine and irradiated albite were acquired at far-from-equilibrium conditions. This was ascertained by quantifying ΔG_d of the solution by using the measured concentrations of albite's solubilized species to calculate its saturation level in solution (i.e., IAP/Ksp). It was thus determined that ΔG_d < -60 kJ/mol across the majority of dissolution scenarios selected; with only one dissolution scenario featuring a slightly lower absolute value of ΔG_d (-52 kJ/mol at 25°C and pH 10; see Figure 2-5(a)). The dissolution of albite is characterized by three regimes, based on the dependence of rates with ΔG_d: [88, 89, 91] far-from-equilibrium (ΔG_d < -60 kJ/mol), in which dissolution rates are independent of ΔG_d; transition equilibrium (-60 ≤ ΔGd ≤ -25 kJ/mol), in which the dissolution rate changes sharply with ΔG_d, and near-equilibrium conditions (-25 ≤ ΔG_d ≤ 0 kJ/mol), in which the rate varies less severely with ΔG_d as solution saturation is approached towards the asymptotic limit. Simply, since ΔG_d is an indicator of the proximity (or lack thereof) to equilibrium, analysis of ΔG_d helps confirm that the dissolution of albite is indeed independent of the saturation state of the solution. As such, albite dissolves at a near-constant rate. It has been suggested that at far-from-equilibrium conditions, albite achieves steady-state dissolution rates in a time interval of ≥ 1 day. [90] Therefore, herein, albite dissolution was sampled at intervals of exactly 2 days to ensure that steady-state rates were obtained.

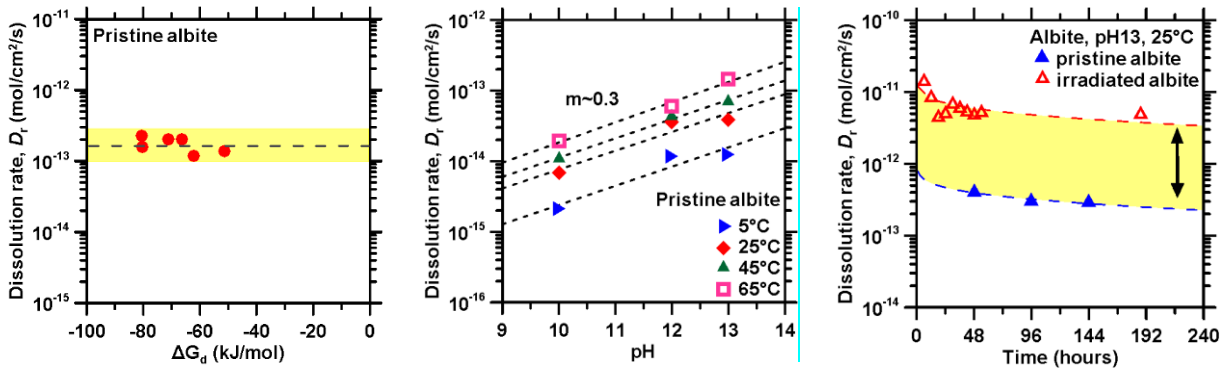

(a) **(b)** **(c)**

Figure 2-5: (a) The dissolution rates of pristine albite at pH 10 and 12, and at different temperatures assessed using VSI as the function of ΔG_d, kJ/mol, calculated from the composition measured by ICP-OES of the solution after 10 days of reaction. **(b)** The far-from-equilibrium dissolution rates of pristine albite assessed using VSI at different temperatures and solution pH levels. In both (a, b), the dissolution rates, and undersaturation levels were assessed following 12 days of solution contact ensuring that dissolution rates sampled at shorter contact times were at "far-from-equilibrium". **(c)** A representative comparison of dissolution rates of pristine and irradiated albite assessed using VSI as a function of time at T = 25 ± 3°C and pH = 13. The dissolution rate of irradiated albite is around 15x higher than that of pristine albite (shown by the bidirectional arrow).

The dissolution rates of albite increase with pH and temperature (Figure 2-5(b)), as also noted elsewhere. [84] Importantly, across the range of temperatures considered, the trends of (log10) dissolution rate as a function of pH can be fitted by an equation of the form: $y = mx + c$; wherein $m \approx 0.3$. Blum and Lasaga *et al.* [92] reported that albite's dissolution rates are proportional to the surface concentration of OH^- sites; and the number density of OH^- sites depends on the pH of the solution. Since the density of negative sites on albite's surface is noted

to correlate with the solution pH with a slope of 0.3 ($m \approx 0.3$), in turn, it is expected that albite's dissolution rate should show a similar scaling with the solution pH as shown in Figure 2-5(b). It should be noted, however, that albite's dissolution rate achieves a dissolution rate minimum around $pH \approx 7$, i.e., in proximity of its isoelectric point (IEP). [84] Therefore, dissolution rates show a symmetric $m \approx 0.3$ scaling on either side of the IEP, as the pH reduces, or increases. [84]

Figure 2-5(c) shows the dissolution rates of pristine and irradiated albite as a function of time at 25 ± 3°C and pH = 13. It is noted that the dissolution rate of irradiated albite is systematically higher than that of its pristine counterpart. Moreover, fitting of the dissolution trends by an equation of the form $D_r = Aexp(Bx)$, where D_r is the dissolution rate and A and B are fitting constants, shows that the dissolution rate of irradiated albite is around 15 times higher than that of its pristine variant. Thus, a constant y-offset would superimpose the two dissolution trend-lines. Indeed, this result, i.e., where the dissolution rates of irradiated albite are around 15-to-25 times higher than that of pristine albite is consistent across all solution pH's, and reaction temperatures considered (see also Figure B). This observation of elevated dissolution rates for irradiated albite, compared to pristine albite is comparable with the results of Hamilton *et al.*[72] who showed that dissolution rate of a 'glass' compositionally equivalent to crystalline albite, is consistently higher than that of crystalline albite under alkaline solutions. Such 'albite glass' has similar short-range order (SRO) and a more disordered structure at longer range as compared to crystalline albite, thereby being more similar to irradiated albite. [52, 57, 93, 94] Specifically, it is suggested that within the irradiated region, the damage to the atomic structure of albite (e.g., since Al-O-Si and Si-O-Si bonds are destabilized), eases the detachment of Al and Si atoms from the solid – resulting in a higher dissolution rate for irradiated albite vis-à-vis pristine albite. Furthermore, it should be noted that, even following dissolution of the surficial "600 nm"

damage zone which is expected to be consumed after 48 hours of dissolution for the data shown in Figure 2-5(c), the dissolution rate of the implanted sample still exceeds that of pristine albite. This suggests that the influence of Ar^+ bombardment on albite extends deeper into the structure than initially estimated, e.g., perhaps due to the persistence of misfit strains caused due to the volumetric expansion of the surface-layers vis-à-vis the bulk sample.

2.3.2. Assessing structural alterations following irradiation using FTIR spectra

FTIR spectra of silicate minerals usually show peaks in two regions: (1) > 2500 cm-1, which corresponds to the vibrations induced by hydroxyl groups, and (2) < 1300 cm-1, which features vibrations of the silicate network. Our analysis focuses on this latter wavenumber region. [79–81]To carefully analyze the data, the FTIR spectrum was separated and magnified into two groups: a low wavenumber region (450-to-800 cm^{-1}) and high wavenumber region (800-to-1200 cm^{-1}), as shown in Figure 2-6. It has been previously noted that these two spectral ranges exhibit peaks that are closely correlated with the structural features of albite's network and its degree of disorder. [93] For clarity, vibration modes corresponding to each peak are listed in Table 2-1. [94–97]

Previously, [79, 80, 93]it has been shown that the change in the degree of structural ordering in silicate minerals can be established based on the increase in intensity, number and sharpness, and also based on the shifts in band frequencies of the peaks. The two most obvious peaks in silicate minerals are those centered at 450 cm^{-1} and 780 cm^{-1}, [94]which represent the rocking motion of the Si-O-Si bridging oxygen (BO) in siloxane bonds and the bending of Si-O-Si bonds, respectively. In aluminosilicates, the peak centered at 650 cm^{-1} [79–81] represents tetrahedral ring vibrations. The presence of Na atoms in the network enables charge-

compensation of 4-fold coordinated $[AlO_4]^{5-}$ units or the depolymerization of the network through the formation of non-bridging oxygen (NBO) atoms. In turn, these structural features affect the vibration modes of the rest of the aluminosilicate network. [79–81] In particular, the peak centered at 540 cm^{-1} [79–81] represents the coupling of the bending of O-Si-O bonds within $[SiO_4]^{4-}$ tetrahedra and Na-O bonds.

Table 2-1: The relevant FTIR peak positions and the assignment of their corresponding vibration modes for aluminosilicates, and specifically pristine and irradiated albite.

		Pristine albite	**Irradiated albite**	**δω**
Reference peaks (cm^{-1})	**Vibration mode**	**Peaks (cm^{-1})**	**Peaks (cm^{-1})**	
450	Si-O-Si rocking (vibration of the bridging oxygen in the direction normal to the initial Si-O-Si plane) [94]	463	461	2
540	Coupling of the bending of O-Si-O bonds within silicate tetrahedra and Na-O stretching [80, 93]	531	523	8
650	Tetrahedral ring vibration [93]	648	645	3
780	Si-O-Si bending (vibration of the bridging oxygen in the direction perpendicular to Si-Si axis within the initial Si-O-Si plane) [94, 95]	761	759	2
900-1200	Bridging-stretching modes of SiO_4 tetrahedra [94–96]	1096	1044	52

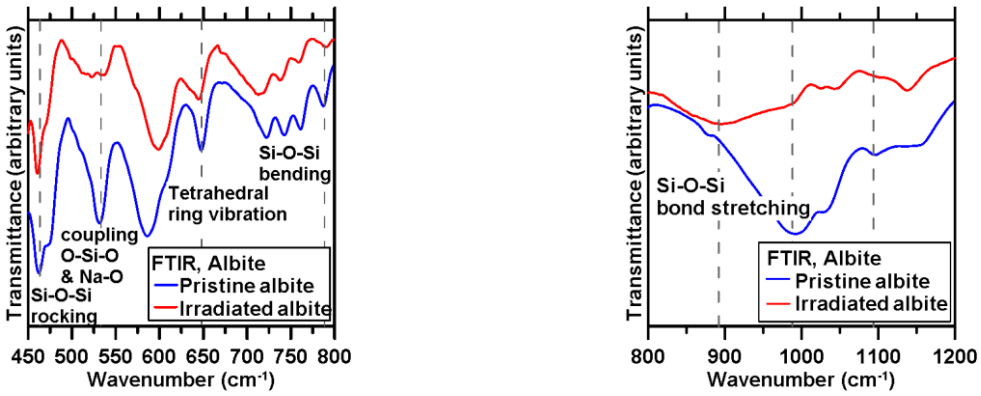

(a) **(b)**

Figure 2-6: Representative FTIR spectra of the albite samples in the: **(a)** lower wavenumbers region, and, **(b)** higher wavenumbers region.

Upon irradiation, the peaks present in the low wavenumber region (450-800 nm^{-1}) are systematically shifted toward (yet) lower wavenumbers, indicating a decrease in the degree of structural ordering. [93] The same trend is observed in the case of peaks in the higher wavenumber region that correspond to Si-BO and Si-NBO bond stretching modes. The extent of (incremental) peak shift can be calculated as: $\delta\omega = \omega_{pristine} - \omega_{irradiated} \propto \Delta Q^2$, where, ΔQ is the difference in the degree of structural ordering between the irradiated and pristine (reference) samples, [79] and $\omega_{pristine}$ and $\omega_{irradiated}$ represent the wavenumbers of a given vibrational mode in pristine and irradiated albite, respectively (see Table 2-1). Since the peak shift is related to the degree of disordering within the aluminosilicate network, in general, the larger the peak shift or reduction in peak intensity, the larger the extent of disorder in the structure. These trends are explained in further details in conjunction with the results of molecular dynamics (MD) simulations below.

2.3.3. Using MD simulations and topological constraint theory to assess structural alterations following irradiation and their implications on chemical durability

Since MD simulations provide direct access to the trajectory of atoms, these results can be used to complement the FTIR data and assess, in detail, the effects of irradiation on the atomic structure of albite. First, Figure 2-7(a) shows the evolution of albite's density with increasing irradiation. Following irradiation, albite exhibits a progressive decrease in its density, from 2.61 g/cm^3 to 2.44 g/cm^3, which indicates a decrease in the compactness of its atomic network; as also suggested by the data of Dennisov *et al.* [98] However, this decrease is smaller compared to that seen in quartz, whose density decreases from 2.65 g/cm^3 to 2.27 g/cm^3 upon irradiation. This is consistent with the fact that alkali aluminosilicate glasses typically feature higher densities than their alkali-free counterparts. [54] This arises from the fact that, although vitrification- or irradiation-induced disordering results in the formation of large, poorly packed silicate rings, alkali atoms tend to fill the voids that persist within these rings, thereby somewhat enhancing the atomic packing efficiency. [99] It should be noted that because the depth of the implantation zone is very small (around 600 nm, see Figure 2-2) in comparison with the thickness of the sample, which is on the order of 1 mm, it is challenging to directly measure the associated change in density of the irradiated layer using traditional density measurement techniques (e.g., X-ray diffraction, or He pycnometry).

The disordering of the atomic network resulting from the exposure to radiation can be assessed from the pair distribution function (PDF, g(r), i.e., the probability of finding an atom as the function of the distance from a central atom, normalized by the average atomic density). Figure 2-7(b) shows the PDF's of pristine and irradiated albite. First, it is noted that these two systems exhibit similar short-range order (SRO, < 3 Å), which shows that the bond lengths and

coordination numbers of each atomic species remains fairly unaffected by irradiation. In contrast, their medium-range order (MRO, > 3 Å) differs significantly, namely, the peaks observed at larger distances in the PDF of pristine albite disappear upon irradiation, as often observed upon vitrification. [100, 101] This shows that the progressive accumulation of irradiation-induced defects (damage) results in the loss of the long-range periodicity of the structure of (pristine) crystalline albite.

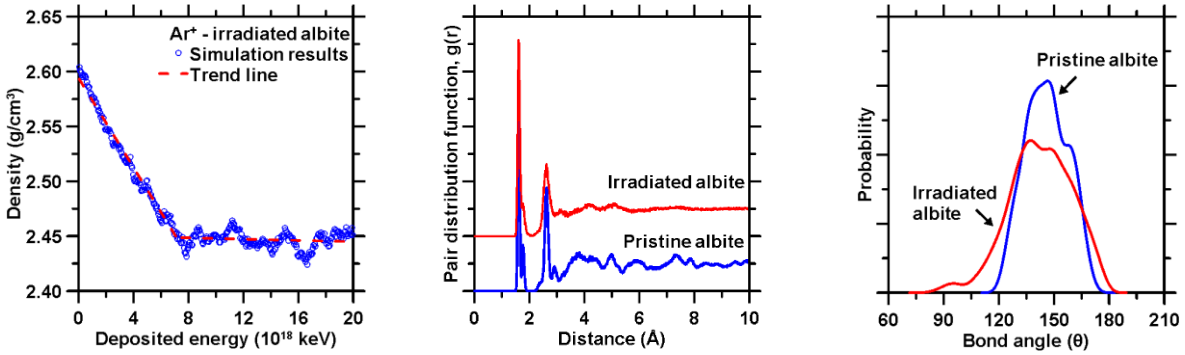

Figure 2-7: (a) The evolution of the density of albite with increasing irradiation that is described herein by the deposited energy. **(b)** The pair distribution functions (g(r)) of pristine and irradiated albite. **(c)** The bond angle distributions (BADs) of the Si-O-Si inter-tetrahedral angle for pristine and irradiated albite.

Furthermore, it is observed that the disordering of albite's structure is reflected in two main structural features: (1) a distortion of Si-O-Si angles, and, (2) the formation of NBO atoms. First, as shown in Figure 2-7(c), the Si-O-Si inter-tetrahedral bond angle distribution (BAD) becomes broader and shifts toward lower angular values. These trends are also observed in irradiated quartz. [102] Such broadening of the Si-O-Si angle is also associated with a shift

toward lower wavenumbers of the peak associated with the Si-O-Si bending mode in the FTIR spectrum (see Figure 2-6 and Table 2-1). This shows that the energy (and bending frequency) of the Si-O-Si bond angle decreases upon irradiation. Second, although pristine albite only features BO atoms (wherein Na atoms compensate the charge of AlO_4 units), irradiation results in the formation of NBO atoms (i.e., Si-O-Na bonds), which eventually represent around 6 % of all O atoms. The formation of NBO atoms results in a decrease in the degree of polymerization of albite's network. This induces a shift of the higher wavenumber (800-1200 cm^{-1}) peaks of the FTIR spectrum, which are associated with stretching modes of Si-BO and Si-NBO bonds. It should be noted, however, that besides the formation of NBO species (Si-O-Na bonds), irradiation also results in the formation of other defects, for example: around 12% and 0.3% of Al atoms display 3- and 5-fold coordination, respectively, and 4% of O atoms are 3-fold coordinated, i.e., forming tricluster units.

To elucidate the linkages between the effects of irradiation on the structure of albite and its chemical durability, topological constraint theory (TCT) is used. [103, 104]TCT reduces complex atomic networks into simple trusses of nodes (atoms) connected by mechanical constraints (chemical bonds). As such, TCT captures the significant features of the atomic topology while filtering out less relevant details that do not significantly affect macroscopic behavior. [59] In TCT, the rigidity of an atomic network is assessed by determining the number of topological constraints per atom, n_c. In atomic networks, the constraints comprise the radial bond-stretching (BS) and angular bond-bending (BB) variants, which maintain the bond lengths and bond angles fixed around their average values, respectively. As per Maxwell's stability criterion, [60] atomic networks can be described as being: (1) flexible ($n_c<3$), showing floppy internal modes of deformation, [105] (2) stressed-rigid ($n_c>3$), featuring eigenstress due to

mutually incompatible constraints, [106, 107] or, (3) isostatic (n_c=3), being rigid but free of eigenstress. In the latter case, the value "three" corresponds to the number of degrees of freedom per atom in a 3D-network. By capturing the atomic topology within a simple metric (n_c), recently, TCT has been shown to offer a consistent framework which links dissolution rates, to the number of atomic constraints as follows: [108] $D_r = D_{r0} \exp(\frac{- n_c E_0}{RT})$, where, D_r is the dissolution rate, D_{r0} is a rate constant that depends on the chemistry of the solution, and E_0 is the energy required to rupture a single atomic constraint.

Expectedly then, the dissolution rate decreases as n_c increases, which is in agreement with the idea that solids featuring low-energy internal modes of deformation (floppy modes) would be more unstable and dissolve faster than more rigid systems. To understand the role of irradiation-induced structural disordering on amplifications in albite's dissolution rate, the number of BS and BB constraints present in the networks of pristine and irradiated albite were compared. First, a slight decrease in the number of radial BS constraints is noted in irradiated albite. This is a direct consequence of the depolymerization of the network resulting from the formation of NBO atoms. Second, a more pronounced decrease in the number of angular BB constraints is observed. This arises from the breakage of the Si-O-Si BB constraints upon irradiation. Namely, in pristine albite, the Si-O-Si bond angle distribution is sharp, which denotes the existence of an underlying BB constraint that maintains bond angles fixed around their average value. In contrast, as shown in Figure 2-7(c) and as supported by the FTIR spectrum (Figure 2-6), this distribution significantly broadens upon irradiation, which indicates the breakage of the underlying constraint. Such breakage of the Si-O-Si inter-tetrahedral BB constraints has also been observed in irradiated quartz [102] and glassy silica. [109]

Altogether, irradiation results in a decrease in the number of constraints per atom in albite by 0.307 units (i.e., Δn_c = 0.307, wherein n_c equals 3.077 and 2.770 in pristine and irradiated albite respectively). Given topological controls on mineral dissolution rates, the change in the dissolution rate of irradiated albite vis-à-vis pristine albite can be estimated as: $\frac{D_r^{irr}}{D_r^{prist}} = \exp(\frac{-\Delta n_c E_0}{RT})$, where, D_r^{irr} and D_r^{prist} are the dissolution rates of irradiated and pristine albite, respectively, and the preexponential term, D_{r0}, is assumed to only be a function of the solution chemistry hence independent of the structure of the dissolving solid. Therefore, the preexponential term is eliminated when considering the ratio of the dissolution rates of pristine and irradiated albite under the same conditions of pH and temperature. Based on previous estimates of E_0, quantified as being on the order of 25 ± 5 kJ/mol for a range of silicates, independent of the solution pH or measurement temperature, [108, 110] the topological framework predicts that the dissolution rate of irradiated (disordered) albite should be around 20 times higher than that of pristine albite (i.e., $D_r^{irr} / D_r^{prist} \approx 20$, as calculated from the equation above and based on the Δn_c value calculated herein), a finding which is in excellent agreement with the ratios of the experimental dissolution rates of irradiated and pristine albite samples (see Table 2-2). It should be noted that the applicability of the present dissolution expression is justified a posteriori by the fact that the obtained dissolution enhancement ratios (DERs) indeed remain fairly constant (i.e., in the range of 15-to-20) over a broad range of pH and temperatures as considered herein. Furthermore, it should be noted that, as described in Pignatelli *et al.*, [108] E_0 corresponds to the energy that is required to rupture a unit atomic constraint, i.e., to initiate the dissolution. Indeed, as noted in Ref [110] and [111] (and Figure 2-5 therein), it is evident that the value of E_0, on the order of 20 kJ/mole, does not depend on the solution pH (for pH > 2). It

should also be clarified that the surface roughness (S_a) increase of a factor of 1.4 in the irradiated sample is not sufficient to explain the increase in dissolution rate of the irradiated samples vis-à-vis the pristine samples by a factor of 20. This is significant as taken together, these outcomes provide for the first time, a rational means to link irradiation (or pressure-, and temperature-) induced structural (atomic) alterations to changes in the chemical durability of minerals.

Table 2-2: The dissolution enhancement ratio, $DER = D_r^{irr} / D_r^{prist}$, as calculated from the measured dissolution rates (i.e., the decrease in chemical durability) of irradiated albite vis-à-vis pristine albite across a range of solution pH's and reaction temperatures. The topological framework for mineral dissolution kinetics predicts that $D_r^{irr} / D_r^{prist} \approx 20$, which is in excellent agreement with experimental data.

$DER = D_r^{irr} / D_r^{prist}$	**pH 10**	**pH 12**	**pH 13**	**Average**
25°C	22.45 ± 17.62	19.77 ± 5.60	14.49 ± 2.73	16.77 ± 3.52
45°C	14.15 ± 7.99	13.98 ± 8.37	15.79 ± 9.87	
E_0 (kJ/mole)	**pH 10**	**pH 12**	**pH 13**	**Average**
25°C	25.14	24.11	21.60	23.38 ± 1.23
45°C	22.87	22.77	23.82	

2.4. Conclusion

The outcomes of this study clarify that radiation (and heavy ion) exposure irreversibly alters albite's atomic structure, and in turn its physical (reduction of density, volume expansion etc.) and chemical properties (dissolution rate, or chemical reactivity). Albite's chemical durability (i.e., dissolution rate) is shown to be strongly correlated to the number of constraints per atom (nc), quantified via topological constraint theory (TCT). Significantly, it is observed that the disordering of albite's crystal structure following irradiation is reflected in two main structural features including: (1) a distortion of Si-O-Si angles, and, (2) the formation of NBO atoms. First, the distortion of Si-O-Si angles is confirmed by a broadening of the Si-O-Si inter-tetrahedral bond angle distribution and the FTIR peak shifts toward lower angular values. This

indicates that the energy ("bond strength") of the Si-O-Si bond angle decreases following irradiation. Second, the formation of NBO atoms results in a decrease in the degree of polymerization of the silicate network, as also indicated by the FTIR spectra. Taken together, these factors result in a decrease in the number of constraints (nc) of irradiated albite via-à-vis pristine albite. This reduction in the number of constraints when considered within the framework of topological controls on mineral dissolution kinetics predicts that, in general, irradiated albite would dissolve around 20 times faster than pristine albite, in excellent agreement with dissolution rates measured using vertical scanning interferometry (VSI). This enhancement of albite's dissolution rate (i.e., reduction in its chemical durability) following radiation exposure indicates a response similar to quartz, and one that is likely shared by numerous other silicate- and aluminosilicate-minerals. This suggests a need to improve our understanding of the role of irradiation exposure on mineral dissolution kinetics and progressive changes therein on alkali-silica reaction (ASR), and its evolution, and the consequent impacts on concrete durability in irradiated (nuclear power plant) environments.

Chapter 3 Role of Electrochemical Surface Potential and Irradiation on Garnet-type Almandine's Dissolution Kinetics

3.1. Introduction and Background

Almandine ($Fe_3Al_2(SiO_4)_3$) – a nesosilicate mineral and an end-member of the garnet family ($X_3Y_2(SiO_4)_3$), consists of isolated silicate tetrahedra connected by cations of mixed valence ($X = Fe^{2+}$, $Y = Al^{3+}$). It is found in abundance in metamorphic [112, 113] and igneous rocks. [114] For this reason, garnet-containing sands find extensive use in engineering applications, [115–119]e.g., in the form of siliceous mineral aggregates (sand and stone) in concrete – a mixture composed of cement, aggregates and water, [115] in water filtration [116] and as abrasives in waterjet cutting. [117, 118] Since the durability of composites such as concrete depends on the durability of its constituents, there is a need to understand how the chemical environment (e.g., solution pH), and external stimuli (e.g., radiation), which may induce changes in its structure, may affect its properties. This is of special relevance in facilities such as nuclear power plants (NPPs) wherein environmental variables – e.g., exposure to irradiation and the alkaline environment – could compromise concrete's chemical durability.[6, 7, 61, 120]

Almandine is composed of mixed-valence cations (Fe^{2+} and Al^{3+}) and isolated silicate tetrahedra and aluminate octahedra, wherein no O atoms are shared between two Si atoms or two Al atoms (see Figure 3-1). Due to the isolated (non-percolating) nature of the silicate tetrahedra, almandine is substantially less polymerized than framework silicates such as quartz and albite. [121]As a result, during dissolution, isolated silicate tetrahedra and aluminate octahedra in nesosilicates are released intact from reacting surfaces following protonation (or hydrolysis) of bonds between Fe^{2+} and structural oxygens. [122] This is unlike the case of tectosilicates (i.e.,

which feature percolated silicate tetrahedra in which all O atoms are shared between Si atoms) such as quartz and feldspar wherein bond hydrolysis needs to occur in the silicate tetrahedra to release aqueous silicon species. In addition, almandine's dissolution is also induced by ion-exchange or hydrolysis in acidic or caustic media, respectively, processes which control its dissolution behavior as a function of the pH, as typical of complex silicates. [123]

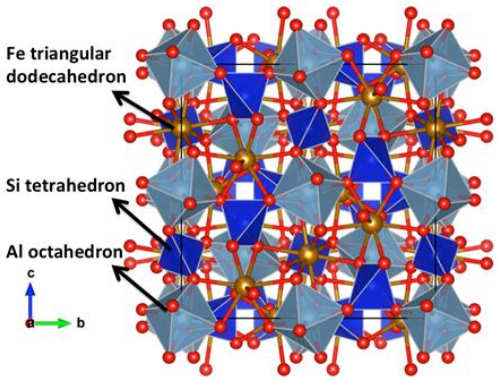

Figure 3-1: The crystal structure of pristine almandine ($Fe_3Al_2(SiO_4)_3$) showing isolated Si tetrahedra (dark blue), Al octahedra (light blue), Fe atoms (yellow) and O atoms (red) as visualized using VESTA. [66]

The rate of release of aqueous Si is typically regarded as reflecting a mineral's dissolution rate. [124] Several studies have shown similarities between the mechanisms of nesosilicate's dissolution, wherein hydrated cations leave a dissolving mineral surface, and ligand exchange reactions, in which a hydrated cation complex exchanges with protons or hydroxyls in water. [122] In almandine, Fe^{2+} cations detach earliest producing an appropriate charge on almandine's surface due to the remaining Si and Al sites. As such, the observed rates of dissolution reflect the combined effects of cation release and pH-dependent hydrolysis. This is

significant as surface charge variations as a function of pH may offer guidance regarding almandine's pH-dependent dissolution rates.

Usually, the disordering of a silicate's atomic structure, when induced at constant composition (e.g., due to pressure, temperature or ballistic shocks), is expected to result in elevations of chemical reactivity, as indicated by aqueous dissolution rates—although there are exceptions depending on the solution's composition or the silicate's atomic structure. [72] The vast majority of such disordering-induced reactivity amplifications have been studied in framework (i.e., percolated) silicates wherein silicate tetrahedra are intimately connected to each other. It is unknown whether silicates consisting of isolated (non-percolating) silicate tetrahedra may show similar sensitivity to atomic disordering. In order to better understand these aspects, the dissolution behavior of disordered (irradiated) almandine was examined using vertical scanning interferometry (VSI) from observations of surface retreat. Molecular dynamics (MD) simulations and topological constraint theory (TCT) were used to explain the dissolution trends in the context of changes in atomic structure, e.g., in terms of the coordination number, bond length, and bond angle distributions. It is shown that nesosilicates feature relatively small changes in chemical reactivity following irradiation – since their isolated silicate tetrahedra show little if any change in structural connectivity. This behavior is consistent with the dissolution mechanism revealed from pH-dependent measurements of dissolution rates. Taken together, these new insights offer guidance regarding the role of the electrochemical and ballistic environment on affecting the durability of garnet-type silicates in aggressive environments.

3.2. Materials and Methods

3.2.1. Sample Preparation and Ion Irradiation

Naturally occurring almandine was sourced from Ward's Natural Science Company. [73] The samples were sliced using a low speed diamond saw (IsoMet^{TM} 1000, Buehler Inc.) into a size of 1 cm × 1 cm × 1 mm. The pristine (non-irradiated) samples were embedded in a cold-cured inert acrylic resin (EpoxiCure Resin, PN 203430128: Buehler Inc.). After 24 hours, the resin-mounted samples were successively mechanically polished using 400, 600, 800 and 1200 grit SiC abrasives, and then using diamond paste (starting from 6, 3, 1 down to 0.25 µm). The polished almandine samples had a surface roughness (S_a) of 100 nm over a field of view (FoV) of 1.3 µm × 1.3 µm as assessed using vertical scanning interferometry (VSI).

In addition, polished samples prepared for Ar^+ ion implantation were sent to the Michigan Ion Beam Laboratory (MIBL). [74] Ion implantation was conducted using 400 keV Ar^+ ions at room temperature to a total fluence (dose) of 1.0×10^{14} ions/cm^2. Ar^+ ion irradiation was selected to simulate neutron irradiation in nuclear power plants because it offers precise control of the temperature and dose, and is known to result in similar alterations to the crystal structure at terminal disordering. [12, 76]The Ar^+ implantation depth was calculated using "Stopping and Range of Ions in Matter" (SRIM) to be on the order of 420 nm, assuming the samples are defect-free single crystals. The calculation assumes that the density of almandine is 4.30 g/cm^3, and that it features a composition of $Fe_3Al_2(SiO_4)_3$. It should be noted however that the natural almandine used herein contains minor impurities such as biotite and amphibole as detected using polarized light microscopy (Figure 3-2), which is expected to result in a penetration depth greater than 420 nm. The irradiated almandine samples were then adhered to a cylindrical resin mount to facilitate handling.

3.2.2. X-ray Diffraction (XRD)

Finely powdered almandine was mounted on a rotating sample holder, and analyzed using powder x-ray diffraction (XRD). The diffraction patterns were collected using a Bruker D8-Advance powder x-ray diffractometer in θ-θ Bragg-Brentano geometry, using Cu-Kα radiation (λ = 1.5406 Å) at an accelerating voltage of 40 kV, and a beam intensity of 40 mA. Each pattern was recorded for a total duration of 16 minutes at a step size of 0.02° in the range of scattering angles, θ, between 10° to 70°. The XRD pattern of the almandine sample is similar to that of pure almandine reported in the literature, [125] albeit showing the presence of biotite and amphibole impurities (see Figures 3-2).

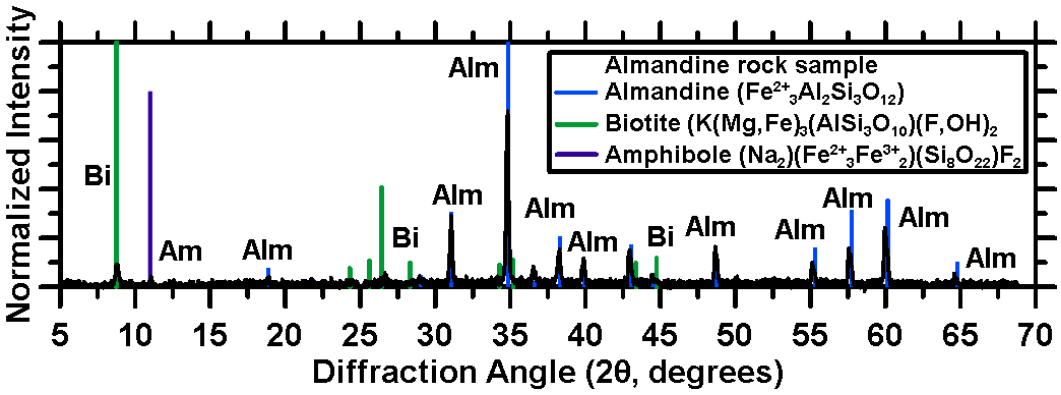

Figure 3-2: The x-ray diffraction patterns of the natural (non-irradiated) almandine powder showing the presence of biotite and amphibole impurities.

3.2.3. Thin section analysis using polarized light microscopy

The almandine sample was sectioned and trimmed to a thickness of 30 μm (Wagner Petrographic) and examined using a polarized light microscope (Leica DM750P). [126] This analysis revealed impurities in the almandine matrix in the form of biotite and amphibole (Figure 3-2), in agreement with the x-ray diffraction patterns shown in Figure 3-3.

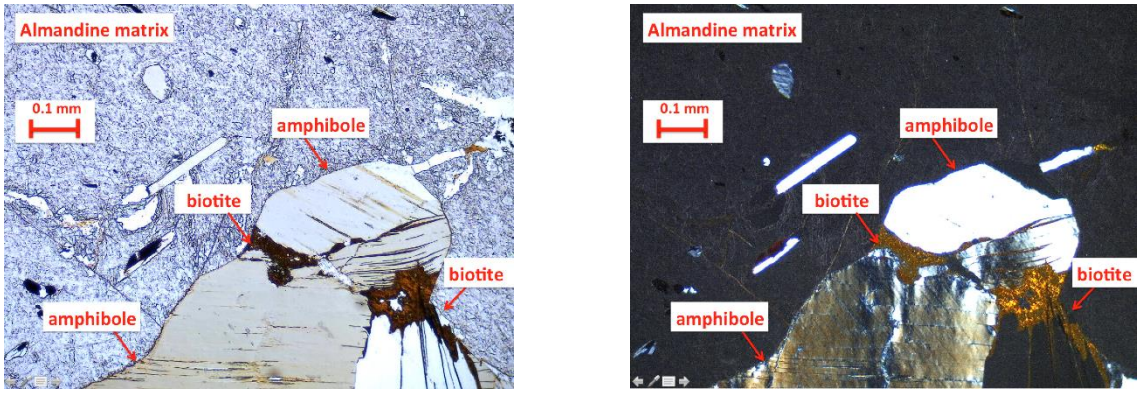

(a) **(b)**

Figure 3-3: Representative polarized light microscopy images of a thin section of the almandine sample shown in: **(a)** plane-polarized light, and, **(b)** cross-polarized light showing impurities of biotite and amphibole. The sample is dominantly composed of almandine, as evidenced from petrographic analysis. However, the images shown here represent a magnified region selected to demonstrate the presence of impurities.

3.2.4. Zeta potential measurement

The zeta potential of finely powdered almandine particulates ($d_{50} \approx 20$ μm) was measured by suspending 1 g of particulates in 100 mL Milli-Q deionized water (>18 MΩ·cm) that was conditioned to an appropriate pH (1, 2, 4, 6, 10, 12 and 13) using NaOH (basic regime) or HCl (acidic regime). The suspensions were sonicated for 1 minute after which 1.5 mL of the suspension containing the particulates was placed into a cuvette for zeta potential measurements. Zeta potentials were measured using a ZetaPALS analyzer from Brookhaven Instruments Corporation [127] that used an acoustic electrophoresis (i.e., streaming potential) method. At each pH, ten discrete measurements of the zeta potential were obtained which were then averaged to obtain statistically representative data.

3.2.5. Measuring almandine's dissolution rates using vertical scanning interferometry (VSI)

Almandine was dissolved under flowing conditions using a flow-through cell (in-line diffusion cell, PermeGear) at 25 ± 3 °C at each solution pH. The solutions were prepared by adding NaOH or HCl to Milli-Q water (>18 MΩ·cm), and the pH of each solution was measured using a ThermoFisher Scientific Orion Versa Star Pro pH Benchtop Multiparameter Meter calibrated over the range $1 \leq pH \leq 13$ at 25 ± 3 °C. The solutions were pumped into the flow-through cell using a peristaltic pump (Bio-Rad) [128] at flow rates ranging between 0-to-18 mL/minute.

To correlate atomic (structural) alterations following irradiation to dissolution rates, the dissolution rates of pristine and irradiated almandine were measured using vertical scanning interferometry (VSI) by quantifying the surface retreat due to dissolution following contact with flowing solutions. It should be noted that a portion of the sample surface was covered with an inert silicone mask (Silicone Solutions SS-38) to offer a "reference/inert area" from which the extent of surface retreat of the dissolving (unmasked) area was measured. Following contact of the almandine samples with the flowing solution for a selected contact time, the samples were removed from the flow cell, and their surfaces were evacuated of any residual solution by exposing them to a stream of compressed air. Thereafter, the silicone mask was peeled off to expose the unreacted surface. In the last step, the sample's surface topography was measured using VSI (in air).

The nanoscale vertical resolution (1-2 nm) of VSI offers the ability to directly track the change in height of the reacting surface with respect to a masked reference, as a function of the solution exposure interval. This allows us to assess dissolution rates of reacting (dissolving,

precipitating, or corroding) materials at unparalleled resolution. VSI images were acquired using a 50× Mirau objective (numerical aperture, N.A. = 0.55) which offers a lateral resolution of around 163 nm. A single image field acquired using this objective features lateral dimensions of 170 μm × 170 μm. However, by stitching partially overlapping adjacent images, the field of view (FoV) can be virtually expanded such that, herein, a stitched image field with dimensions of 1236 μm × 441 μm was acquired (N.B.: the image grid consisted of 10 × 3 images). All images were acquired while accounting for the effects of tilt, i.e., by nulling the surfaces. The fringes on the sample surface correspond to the light and dark bands that are produced by the – constructive (amplitude enhances) or destructive (amplitude diminishes) – interference of the light source. The operation of nulling the surfaces minimizes and distinguishes the number of fringes that are visible inside the field of view (FoV) by adjusting the pitch (P) and roll (R) of the stage, thus ensuring that the sample surface is level and is oriented perpendicular to the light source. The analyses of acquired VSI images were carried out using Gwyddion (version 2.48) [86] which quantified the change in height of the un-masked surface area with respect to the "reference area". The change in height (Δh, nm) was divided by the solution contact time (Δt, h) to reveal the dissolution rate ($D_R = \Delta h/\Delta t$, nm/h). The uncertainty in dissolution rates acquired in this manner is estimated to be on the order of 10% due to inherent uncertainties in VSI measurements, e.g., low-frequency vibrations that may not be fully damped, or the effects of temperature variations in the surrounding environment.

3.3. Results and Discussion

3.3.1. The dissolution behavior of pristine almandine in acidic and basic environments

The steady-state dissolution rates of pristine and irradiated almandine were measured using VSI at a flow rate of 13.5 mL/min after a total solution contact time of 6 hours. This flow rate was selected following measurements of dissolution rates over a wide range of flow rates since it is known that both the flow rate and period of solution contact affect attainment of the steady-state dissolution condition (see Figure 3-4(a)). The flow rate dependent dissolution analysis indicated that: (a) for flow rates greater than 8 mL/min, the dissolution rate of almandine became invariant with flow rate (e.g., see Figure 3-4(a)) indicating that steady-state dissolution has been achieved; wherein the rate of release of constituent species from almandine is constant, and, (b) flow rates greater than 8 mL/min were sufficient to prevent the formation and accumulation of aluminum hydroxide ($Al(OH)_3$) and ferrous hydroxide ($Fe(OH)_2$) precipitates [129] on almandine's surface which could compromise measurements of surface topography, and surface retreat using VSI. This is because, when causticity is abundant, following the equation $M^{2+} + nOH^- \rightarrow M(OH)_{n(s)}$, where, M is a metal ion, almandine's dissolution results in the precipitation of $Al(OH)_3$ and $Fe(OH)_2$ on account of their low solubilities.

While dissolution is noted to be incongruent at short solvent contact times, at steady-state, dissolution is congruent, i.e., stoichiometric, as evidenced by separate measurements of elemental compositions of reacted solutions at acidic pH by inductively coupled plasma-optical emission spectrometry (ICP-OES), consistent with Walther *et al.* (1996). [130] The observed incongruency during initial stages of dissolution is typical to aluminosilicates, and the preferential release of either Al [84, 130, 131] or Si [132] initially has been previously observed at acidic pH. The enhanced rate of Si release relative to Al in the almandine sample may be on account of the size differences of silicate tetrahedra and aluminate octahedra, and the prevalence of isolated silicate tetrahedra in almandine's structure.

The dissolution of nesosilicates such as Ca_2SiO_4, Mg_2SiO_4, Be_2SiO_4, Ni_2SiO_4 and Co_2SiO_4 occurs through mechanisms including the rupture of cationic bonds and release of silicate tetrahedra, and hydrolysis of Si-O bonds within the silicate structural units. [133, 134] In general, the dissolution rates in acidic media of silicates consisting of a single framework cation have been found to scale in ascending order with the size of the framework cation (Figure 3-4(b)). [133] Westrich *et al.* explained this scaling in acidic solutions as being indicative of the relative ease of exchanging the framework cation with protons during ion-exchange controlled dissolution. [133] In proton-promoted dissolution, bridging oxygens at the mineral surface are replaced by water molecules or hydroxyl ions; the replaced hydrated ions are ultimately released from the mineral to the aqueous solution. The rate of solvent exchange correlates with size of hydrated ions, particularly since, larger cations have a larger surface area to accommodate more protons in associative exchange, which make them easier to detach. A comparison of almandine's dissolution rate, a mixed-cation nesosilicate, with single-cation nesosilicates shows a trend that is consistent with this concept (Figure 3-4(b)). This is indeed suggested by the work of Westrich *et al.* which estimated dissolution rates for mixed-cation nesosilicates by a linear rule of mixtures for solid-solution compositions (e.g., analogous to Vegard's law) [135] as shown in Equation (3-1 and 3-2):

$$r\left(A_xB_y(SiO_4)_z\right) = A_{at.\%}[r(A_a(SiO_4)_c)] + B_{at.\%}[r(B_b(SiO_4)_d)] \quad \text{Eq. (3-1)}$$

$$D_r\left(A_xB_y(SiO_4)_z\right) = A_{at.\%}[D_r(A_a(SiO_4)_c)] + B_{at.\%}[D_r(B_b(SiO_4)_d)] \quad \text{Eq. (3-2)}$$

, where, r is the cation radius, D_r is the dissolution rate, A and B are metal cations, and *at.%* represents the atomic fraction of a given cation in the mixed-cation composition. Of course, the implicit condition that needs to be satisfied in the case of mixed-cation nesosilicates is that the cations feature similar sizes. A similar relationship can be expected at high pH, such that cations

with a larger field strength (i.e., ratio of charge to radius) induce faster dissolution because of their tendency to concentrate OH^-, which causes bond polarization. The cation influence detailed above describes the variation in rates for a given pH. Steady-state dissolution rates of almandine also vary with pH, as shown in Figure 3-5(a). In general, it is seen that dissolution rate achieves a minimum at around pH 5 – featuring increases on either side of this dissolution minimum. Such dependencies of (alumino)silicate dissolution rates on solution pH have been observed extensively wherein the dissolution rate scales as a function of $\{a\}^n$ [87–89] where '{a}' denotes the activity of an ion *a*, typically H^+ or OH^- species depending on the solution pH, and *n* is an empirical fitting coefficient. When the logarithm of the dissolution rates is plotted as a function of the solution pH – *n* is often noted to vary between $0.3 \leq n \leq 0.5$ for silicates. [130, 136]

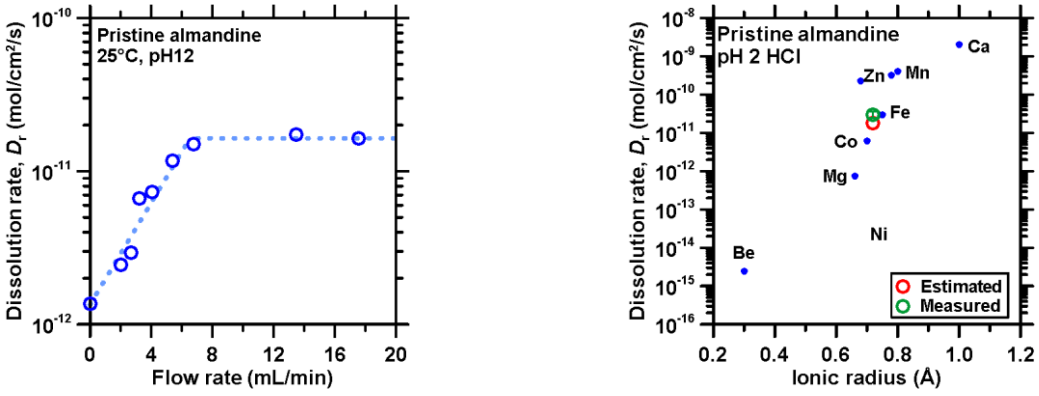

(a) **(b)**

Figure 3-4: (a) The dissolution rate of almandine as a function of flow rate quantified using vertical scanning interferometry (VSI). Beyond a flow rate of 8 mL/min the dissolution rate plateaus demonstrating a flow rate independence. **(b)** The dissolution rates of nesosilicates as a function of their cationic radii. Taking into account the average cationic radius (Fe^{2+}, Al^{3+}) of almandine, the dissolution rate of almandine (i.e., a mixed cation nesosilicate) estimated using Equation (3-2) (red) closely matches its measured dissolution rates (green) in agreement with the broader trend that relates dissolution rates and ionic radii for nesosilicates (blue).

Furthermore, it is noted that almandine's zeta potential decreases systematically from acidic to basic regimes with the point of zero charge (PZC) – sited around pH 5 – corresponding to the point at which the surface charges of Al and Si surface sites are minimized. [130] Due to the presence of H_2O, an oxide mineral's surface is generally covered in varying degrees with "surface hydroxyl groups", e.g., Si–OH. [137] For the case of pure silica, the minimum total surface charge is affected only by H^+ and OH^- in the solution, without any specific adsorption on the surface, and hence the PZC and isoelectric point (IEP) are equivalent. In acidic solutions, the reaction between a silicate surface and the solution interface can be written as:

$$Si\text{-}OH + H^{+} \rightarrow Si\text{-}OH_2^{+}$$ Eq. (3-3)

Therefore, positive charges are present on the mineral surface. When the surface contacts alkaline solutions, the reaction can be written as:

$$Si\text{-}OH + OH^{-} \rightarrow H_2O + Si\text{-}O^{-}$$ Eq. (3-4)

This explains the origin of the negative surface charge of silicates in basic solutions. [137]Based on studies on quartz and aluminum oxide, Walther *et al.* [130, 131]observed that the minimum in the dissolution rate occurs at the pH where the sum of absolute charge from Si in quartz or Al in aluminum oxide is minimized—i.e., pH 2.5 and 8.4 for quartz and corundum, respectively. [130]

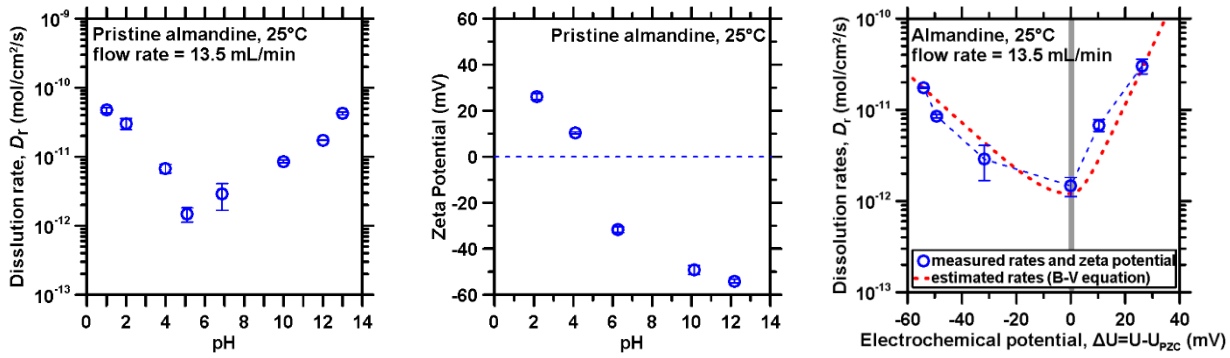

(a) **(b)** **(c)**

Figure 3-5: (a) The dissolution rates of pristine almandine measured at a flow rate of 13.5 mL/min showing the dissolution minimum in the mid-pH region (pH 5). **(b)** The zeta potential of pristine almandine measured as a function of solution pH. **(c)** The dissolution rate of pristine almandine as a function of its zeta potential showing that the dissolution minimum occurs at the pH where the sum of the absolute value of surface charge (Al and Si) is minimized; i.e., the point of zero charge (PZC, pH 5) is achieved. Also shown is a comparison of measured (blue circles) and estimated dissolution rate for pristine almandine (dashed red line) using Equation (3-5).

As such, for aluminosilicates, the dissolution minima are expected to be determined by composition, i.e., the Al/Si ratio, which dictates the pH at which the surface features minimum (zero) surface charge. Since alkalis and alkaline earth cations tend to leach rapidly from aluminosilicates and be replaced by protons, it is the residual Al and Si left on the surface that determine the value of this pH. [130, 138] For example, for Al/Si < 1 (e.g., almandine; Al/Si = 0.67) the surface charge and dissolution rate minimum is observed at a pH between 4 and 6, as noted in Figure 3-5(a-b). This pH-dependence of dissolution rate is controlled by the electrosorption of H^+ and OH^- ions on terminal surface Al or Si sites. Since pure SiO_2 and Al_2O_3

exhibit a dissolution minimum at pH 2.5 and 8.4, respectively, it is expected that, in acidic regimes (pH < 7), the surface charge for SiO_2 is close to 0, and is relatively low in magnitude compared to its value in high pH conditions. The opposite is true for Al_2O_3, which exhibits high surface charge at low pH compared to SiO_2, and while it becomes increasingly negative in alkaline conditions, it remains smaller than of SiO_2. [130, 139, 140] This analysis affords the use of surface charge, as indicated by zeta potentials, to estimate the dissolution kinetics of silicates. It should be noted however that zeta potential does not discriminate the identity of surface sites, and is only sensitive to the total charge arising from both Si or Al sites on the mineral surface.

Recently, Kristiansen *et al.* showed that the dissolution kinetics of silica enhanced with applied potential. [141, 142] Such a dissolution rate-applied potential scaling can be described using the Butler-Volmer equation as shown in Equation (3-5) below:

$$D_r = -Ce^{-\alpha\frac{e}{k_BT}\Delta U} \quad \text{Eq. (3-5)}$$

$$C = \frac{M_m zp}{N_a A\rho} e^{-\frac{1}{k_B}E_{a,0}} \quad \text{Eq. (3-6)}$$

, where, D_r is the mineral dissolution rate (mol/cm^2/s), α is a transfer factor, and the product $\alpha\cdot\Delta U$ (mV) reveals the surface potential (note that in the fitting below, ΔU is the zeta potential, mV), [143] e/k_BT is the "thermal voltage" which equals to 1/25.8 (mV^{-1}) at room temperature (K), where e is the charge on an electron, k_B is Boltzmann's constant (eV/K), T is the temperature (K), and C (mol/cm^2/s) is a material specific constant based on its molar mass (M_m, 497.75 g/mol) and density (ρ, 4.30 g/cm^3), and where E_a is the activation energy of the dissolution reaction (kJ/mol), z is the collision frequency (z, s^{-1}), p is a steric factor (1/6), and A denotes the surface area that is available for dissolution (m^2). It should be noted that the negative sign preceding the transfer factor is eliminated if the surface potential is positive.

By regression, Equation (3-5) can be fitted to the dissolution rates of pristine almandine in acidic and basic regimes, separately, to recover *C* (2.5) and α (3.8 and 1.6), respectively, as shown in Figure 3-5(c). The fitting applies a transfer factor to describe the difference between the surface potential and zeta potential (i.e., if the surface potential and zeta potential were equal, α = 1). [143] The difference in numerical values of α reflects a change in dissolution mechanism (e.g., ion exchange in acidic solution or hydrolysis in basic solution) with pH. The reasonableness of the fitted values of the transfer factor can be assessed from knowledge of the electrical potential as a function of distance from the particle surface as shown in Equation (3-7): [144, 145]

$$j = j_0 e^{-kx} \qquad \text{Eq. (3-7)}$$

$$k = \left(\frac{1}{e_r e_0 kT} \sum_{1}^{M} z_i^2 e^2 n_i^{\infty} \right)^{1/2} \qquad \text{Eq. (3-8)}$$

, where, φ_0 (mV) is the surface potential at x = 0 (i.e., at the mineral surface, nm), κ is the inverse of the Debye length [146] (nm^{-1}) which depends on the solution's ionic strength, $\varepsilon_r\varepsilon_0$ is electrical permittivity, z_i is the valence of the ionic species, $n_i^{¥}$ is the number density in the bulk solution, and M is the number of species (Na^+, OH^-, H^+, Cl^-). As such, $1/e^{-\kappa x}$ = α, i.e., the transfer factor in Equation (3-5). At pH 13, for a 0.1 mol/L NaOH solution, setting x ≈ 0.3 nm to describe the position of the slip results in a transfer factor: $1/e^{-\kappa x}$ = 1.47 which is similar to the value suggested by fitting Equation (3-5) to the data in Figure 3-5(c) under alkaline conditions (α = 1.6). This is a significant finding that supports the use of electrical surface potentials (or alternatively, zeta potential) as a proxy of mineral dissolution rates. As such, it is evident that the dissolution rate of a mineral correlates with the surface potential as described by a modified Butler–Volmer equation. This suggests that mineral dissolution is fundamentally linked to the

electrochemistry of surfaces. Not only does this finding provide new insights into dissolution dynamics in general, but it offers a means to potentially estimate dissolution rates from measured zeta potentials, and vice versa. The universality of the observed relationship between zeta potentials and dissolution rate is an important aspect that needs to be further clarified. Nonetheless, taking the examples of the oxide surfaces of Al_2O_3 and SiO_2, [130] and of mica, silica and zircon, [141] it can be argued that the observed relationship is indeed – general, and broadly applicable – i.e., to both simple, and complex oxide surfaces.

3.3.2. Using MD simulations and topological constraint theory to assess dissolution rate alterations following structural changes induced by irradiation

To elucidate the effects of irradiation on chemical durability, the dissolution rate of irradiated almandine was measured in acidic and basic media. In general, irradiation resulted in an increase (up to 2x, where x is the dissolution rate of pristine almandine at a given pH) in dissolution rate across all pH levels (Figure 3-6(a)). Importantly, the slope of the dissolution rate-pH trendline is unaffected, whether almandine may be irradiated or not, indicating that electrochemical controls on dissolution remained unaffected by radiation (see Section 4.1). This also highlights that while irradiation can alter absolute dissolution rates, it does not alter the rate controlling step(s) in dissolution (i.e., the dissolution mechanism/pathway). Previously, Pignatelli *et al.* and Hsiao *et al.* have shown that silicate dissolution rates substantially elevate following a mineral's exposure (e.g., quartz, albite) to irradiation. [11, 120] This is on account of the structural disordering/amorphization that is induced. However, both quartz and albite feature highly polymerized structures wherein their silicate tetrahedra are intimately connected to each other – forming a periodic framework. Consequently, irradiation induces substantial

depolymerization as a result of which quartz's dissolution rate can elevate by up to 3 orders of magnitude and albite's dissolution rate can increase by up to 20 times at a fixed pH. [120] Conrastingly, almandine shows a comparatively marginal increase (doubling) of its aqueous dissolution rate following irradiation.

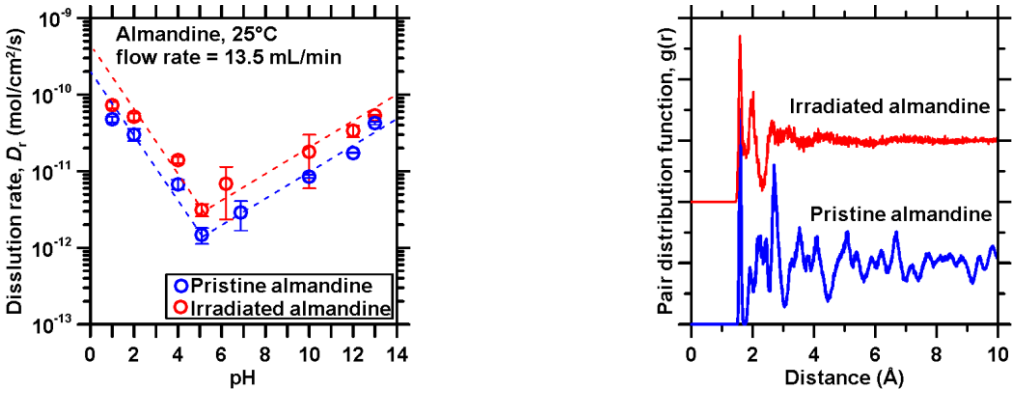

(a) **(b)**

Figure 3-6: (a) The dissolution rates of pristine and irradiated almandine as a function of the solution pH. The similar slopes in acidic and basic regimes clarify that irradiation does not induce a change in the dissolution mechanism, and the elevation in dissolution rates simply arises from a reduction in cation coordination. **(b)** The pair distribution functions (g(r)) of pristine and irradiated almandine.

Since MD simulations provide direct access to the trajectory of atoms, they offer direct insight into the nature of atomic alterations induced in almandine's structure following irradiation. Analysis of the pair distribution functions (PDF, g(r)), before and following irradiation, as shown in Figure 3-6(b) indicates that almandine's short-range order (SRO, <3 Å), bond lengths and coordination numbers of each atomic species remain unaffected following

irradiation. But, for scales at and beyond medium-range order (MRO, >3 Å), a substantial smoothening/dissipation of the PDF is observed, indicative of vitrification. [100–102]

The effects of vitrification on structural connectivity/rigidity can be quantified within the framework of topological constraint theory (TCT). [103, 104] TCT reduces complex atomic networks to a simple network consisting of nodes (atoms) and rigid-members (atomic bonds). [59] This allows computation of the rigidity of an atomic network as described by the average number of topological constraints placed on a given atom in the network (n_c, unitless). The constraints herein include: (a) the radial bond-stretching (BS), and, (b) the angular bond-bending (BB) variants which maintain bond lengths and bond angles fixed around their average values, respectively. Following Maxwell's stability criterion, [60] atomic networks can be categorized as: (1) flexible ($n_c < 3$), showing floppy internal modes of deformation, [105] (2) stressed-rigid ($n_c > 3$), featuring eigenstress due to mutually incompatible constraints, [106, 107] or (3) isostatic ($n_c = 3$), being rigid but free of eigenstress. This nature of analysis reveals that the number of constraint per atom (n_c) for almandine decreased from 2.85 to 2.18, from the pristine to the irradiated state, respectively. This reduction in the number of constraints, or network rigidity, as also reflected by the smoothening of the MRO is on account of: (1) a change in the coordination of 87.8% of Al atoms from octahedral to tetrahedral coordination, (b) a change in the coordination of 74.4% of Fe-species from being 8-coordinated Fe to becoming 5-or-6 coordinated, and, (3) the formation of non-bridging oxygen (NBO) atoms, by an amount equivalent to 33% of all O atoms, which do not exist in pristine almandine.

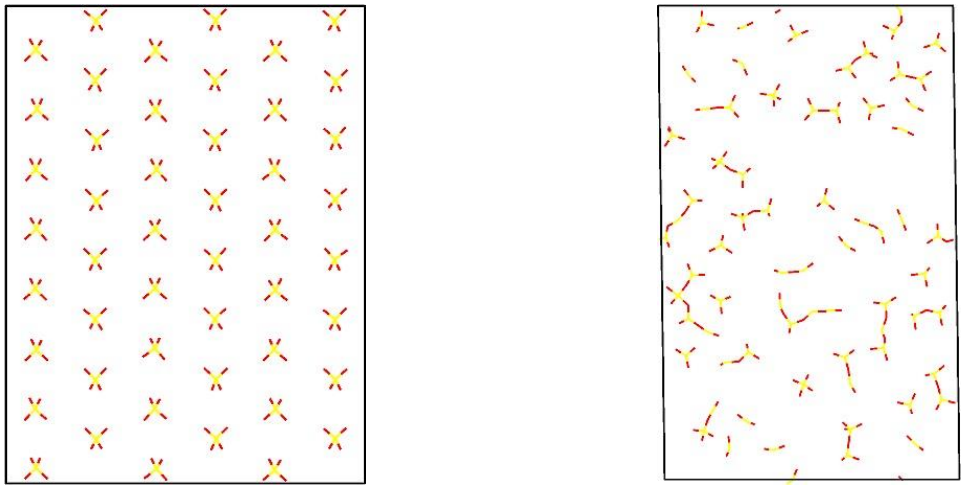

(a) **(b)**

Figure 3-7: Representative snapshots of the simulated atomic structure of: **(a)** pristine and **(b)** irradiated almandine. For clarity, only SiO_4^{4-} units are shown (Si: yellow, O: red) to highlight the state of silicate connectivity through the network.

It is important to note, the decrease in the number of constraints (Δn_c = 0.67) in almandine results mostly from a decrease in cationic coordination number(s) rather than a change in the atomic connectivity of silicate tetrahedra (e.g., a change in Si–O bond length or Si–O–Si bond angle in the case of framework silicates). This is significant as, following Hsiao *et al.* (2017), Δn_c = 0.67 should result in an increase of dissolution rate by around 200 times for typical silicate-based materials. [120] However, a much more modest increase in dissolution rates (and hence decrease in chemical durability) is noted. The breakdown of the previously suggested relationship between dissolution rate and number of constraints per atom can be understood from the fact that, in contrast to more polymerized silicates, [147] irradiation does not induce changes in the connectivity of almandine's silicate backbone – but rather only eases the breakage of cationic (Fe^{2+} and Al^{3+}) bonds in the structure. In silicates, dissolution implies the breakage of

high-energy Si–O bonds, which often serves as the rate-limiting step of dissolution. [110, 148] As shown in Figure 3-7(a), pristine almandine initially exhibits isolated SiO_4 units (i.e., no Si–O–Si bonds are present). Both before and following irradiation, dissolution can proceed without requiring the breakage of Si–O bonds. As such, SiO_4^{4-} units are directly transferred into solution as rigid blocks.

Upon the disordering of almandine's network following irradiation although some Si–O–Si bonds form, they are limited. Hence, many SiO_4^{4-} units remain isolated or form small clusters (see Figure 3-7(b)) so that silicate chains (i.e., –Si–O–Si– bonds) do not percolate throughout the atomic network. This is partially on account of the composition which tends to form Si–O–Al bonds rather than Si–O–Si or Al–O–Al bonds – in partial compliance with Loewenstein's "Al-avoidance" rule. [149, 150] Consequently, dissolution can also occur through another path such as breakage of cationic bonds rather than Si–O bonds. It is the former process that is enhanced by irradiation, particularly through changes in the cation's coordination numbers. It should be noted that the small silicate clusters (i.e., with 2 or 3 Si atoms) that form upon irradiation are expected to be released into solution as rigid units (rather than individual SiO_4^{4-} groups), which explains the slight increase (around 2x) in dissolution rate. Hence, in nesosilicates, dissolution rates are enhanced by facilitated extraction of their cations rather than by affecting the connectivity of the silicate network.

3.4. Conclusion

This study presents new insights into almandine's dissolution behavior in acidic and basic regimes; and following exposure to radiation. First, dissolution kinetics are shown to be correlated with a mineral's surface charge. In particular, it is shown that the minimum

dissolution rate is achieved at pH 5, corresponding to the pH at which almandine, which has a garnet-type structure, achieves a minimum (absolute) value of total Al and Si surface charge. This allows the dissolution rates of almandine to be estimated using a modified Butler-Volmer equation, highlighting the critical role of surface electrochemistry on dissolution processes. Second, it is highlighted that almandine experiences relatively small elevations in dissolution rates following irradiation, as compared to percolated silicates such as quartz and albite with feature higher levels of polymerization. Molecular dynamics simulations show that unlike framework silicates, silicate connectivity in the garnet-type almandine remains broadly unaffected upon irradiation. Instead, the coordination numbers of the cations Fe^{2+} and Al^{3+} decreases, causing a modest, but constant, enhancement in rates across the entire solution pH range. Thus, the mechanisms of dissolution, which include both breakage of cationic bonds and subsequent release of intact silicate tetrahedra as well as pH-dependent hydrolysis of Si–O bonds, are reflected in the observed irradiation effect on overall dissolution rate. As such, the outcomes of this work offer new insights into the origin of, and rate controls on the reactivity of non-percolated garnet-type silicates across a wide range of solution pH's and specifically highlight how surface electrochemistry and surface potential, and network polymerization affect dissolution processes in natural and engineered material systems. This understanding gained, i.e., of electrochemical controls on dissolution processes can be applied not only within an earth science perspective, but also to a diversity of engineered and biological systems including: nuclear waste disposal, glass corrosion, cementation processes, hard tissue systems, and micro- and nanofluidic systems, in which an understanding of the controls on reactivity of oxide surfaces is of considerable importance.

Chapter 4 The effect of irradiation on the atomic structure and chemical durability of calcite and dolomite

4.1. Introduction and Background

Carbonates are common minerals that make up nearly 20% of the sedimentary rocks at the Earth's surface.[151] Limestone, a sedimentary rock composed mainly of calcite ($CaCO_3$) and dolomite ($CaMg(CO_3)_2$), often finds use as a mineral aggregate in concrete.[152–155] Recent studies have shown that aggregates (e.g., limestone) may be altered upon exposure to irradiation, resulting in decreases in compressive strength and elastic modulus of concrete at fluence levels above 1.0×10^{19} n/cm^2.[8] Under prolonged neutron irradiation, aggregates, and their mineral constituents may feature volume expansions or enhancements in their reactivity, e.g., enhanced dissolution rate.[11] The cement paste, because of its poor crystallinity, has been shown to be relatively less affected by neutron irradiation.[156] Such alterations can detrimentally affect the structural integrity of concrete – an issue of particular importance in NPPs.[8, 11, 120, 157, 158]

Volume changes produced in nuclear power plant (NPP) concretes may result from expansion, drying shrinkage, and radiation (e.g., neutron, and γ–rays) effects on the aggregate and cement paste. Aggregates and the minerals therein, which occupy more than 70% of the volume of concrete and are disproportionately affected by radiation exposure, dominantly affect volume changes and the durability of concrete. Thus, damage and cracking of concrete can occur due to mechanical expansive stresses resulting from the irradiation-induced volume changes of the aggregates and the onset of dissolution-facilitated alkali-silica reaction (ASR) or alkali-carbonate reaction (ACR) for siliceous or carbonaceous aggregates[159, 160]

Studies of irradiation-induced alterations of the atomic structure and reactivity of minerals have mainly focused on silicates; e.g., quartz: SiO_2, albite: $NaAlSi_3O_8$, and almandine: $Fe_3Al_2Si_3O_{12}$—which were observed to form disordered structures following their irradiation.[11, 120, 157] However, the effects of irradiation on carbonates remain less clear. For example, for calcite, whereas some studies reported negligible changes both in its atomic structure and dissolution kinetics,[11, 161] others indicate the evolution toward an *amorphous* atomic structure with increasing fluence.[162, 163] Analogous studies on dolomite have not been undertaken. Dolomite and calcite exhibit similar structures, wherein layers of carbonate (CO_3^{2-}) groups separate layers of different cations (Ca^{2+} in calcite, or Ca^{2+} and Mg^{2+} in dolomite) (see Figure 4-1). Both minerals can be described by a rhombohedral unit cell, but the alternating Ca-Mg arrangement in dolomite reduces its symmetry, i.e., vis-à-vis calcite, from $R\bar{3}c$ to $R\bar{3}$. Despite the structural similarity of these two light-metal carbonates, significant differences have been observed with respect to their dissolution kinetics,[164, 165] solubility,[166] and thermal expansion behavior.[167] These differences have been explained in terms of the differences in the properties of the C–O, Ca–O, and Mg–O bonds (e.g., bonding energy, interatomic distance, etc.).[167] As such, it may be envisioned that irradiation influences the structure and properties of these two carbonate minerals distinctly.[168] Therefore, this study examines and compares the effects of irradiation on calcite and dolomite's atomic structures and reactivities in aqueous solutions. Vertical scanning interferometry (VSI) provides high vertical resolution (~ 2 nm) topographical data of reacting surfaces, enabling measurements of dissolution rates of irradiated layers with thickness < 500 nm. The combination of nanoscale (VSI) analytics and molecular dynamics (MD) simulations implemented herein allowed for direct comparison, and analysis of how the atomic structures of mineral, and changes therein result in changes in their chemical

durability. The outcomes of this study offer new insights into the mechanism of irradiation damage of light-metal carbonates at the atomic scale and inform the selection of durable mineral aggregates for the production of concrete that may find use in both nuclear-energy/-waste disposal applications.

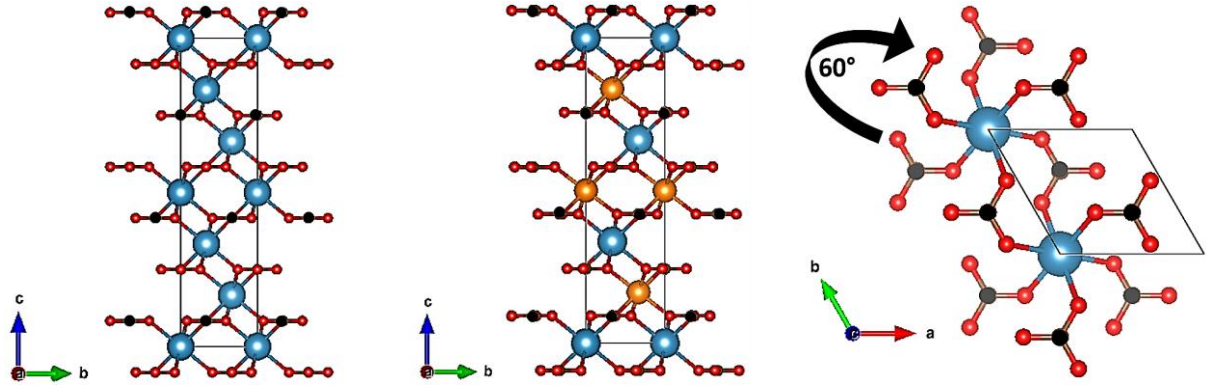

(a) **(b)** **(c)**

Figure 4-1: The crystal structure of **(a)** pristine calcite and **(b)** pristine dolomite projected along the [100]-plane as visualized using VESTA.[66] Ca, Mg, C, and O atoms are shown in blue, orange, black, and red, respectively. The unit cell is outlined in black. **(c)** The unit cell viewed from the [001] orientation.

4.2. Materials and Methods

4.2.1. Sample Preparation and Ion Irradiations

Synthetic single-crystals of (100)-oriented calcite with dimensions of 1 cm × 1 cm × 1 mm (l × w × h) were sourced from MTI Corporation. Naturally occurring dolomite from Sussex County, NJ was obtained from Ward's Science and sectioned to dimensions of 1 cm × 1 cm × 1 mm using a low-speed diamond saw (IsoMet^{TM} 1000, Buehler Inc.). One side of the dolomite

coupons was successively polished using 400, 600, 800, and 1200 grit SiC abrasives and then with diamond paste from 6, 3, 1, and ¼ µm prior to ion implantation.

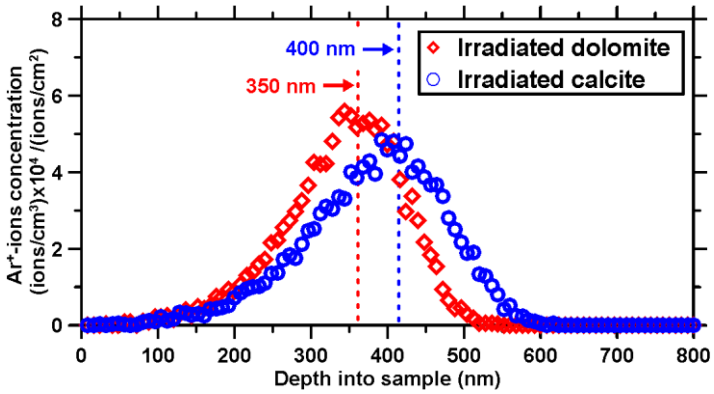

Figure 4-2: The representative Ar^+ ion concentrations as a function of the distance from the implantation surface (located at x = 0 nm). The ion concentration when multiplied by the implantation fluence (10^{14} ions/cm^2) reveals the number density of implanted Ar^+ ions per unit volume. This calculation assumes defect-free, stoichiometric single crystals.

To simulate neutron irradiation, calcite and dolomite were exposed to Ar^+ ions, which induce similar damage as neutrons while offering precise beam control and ease of handling.[12] The as-received calcite and polished dolomite samples were irradiated at the Michigan Ion Beam Laboratory (MIBL) at ambient temperature using a 400 keV Ar^+ ion beam to a total fluence of 1.0 x 10^{14} ions/cm^2. The ion or neutron fluence and the system's temperature determine the extent of irradiation-induced damage and disordering that is produced (e.g., displacements per atom: dpa).[169] For example, a typical neutron fluence after 40 years of operation in nuclear power plants is around 10^{19} n/cm^2.[8] To induce the same extent of disordering via ion bombardment, the fluence must be around 10^5 times lower.[169] Thus, an Ar^+ fluence of 10^{14}

ions/cm^2 was chosen herein. Further, increasing the incident energy beyond 100 eV has been shown to not affect lattice distortion and atomic density.[170, 171] It is noted that the medium recoil energy for 400 keV Ar^+ ions is a factor of 4 lower than for neutrons, although the damage recovery rates of the two are similar.[172] The concentration of implanted Ar^+ ions as a function of depth was calculated using SRIM (Stopping and Range of Ions in Matter) using the "detailed calculation with full damage cascade method" based on the incident energy of the ion beam (400 keV), the displacement energies for each atom, i.e., Ca, Mg, C, and O which are 25, 25, 28, and 28 eV, respectively, and the ideal compositions and densities of the solids (calcite: 2.71 g/cm^3 and dolomite: 2.87 g/cm^3). These calculations indicate ion-influenced depths of around 500 nm and 430 nm for calcite and dolomite, respectively (see Figure 4-2). The presence of impurities and defects that may affect the actual ion-implanted depths were not considered in the SRIM calculations.

4.2.2. Scanning Electron Microscopy-Energy Dispersive X-ray Spectroscopy (SEM-EDS)

To ascertain the composition of dolomite, SEM-EDS analysis was carried out on powdered samples with an average particle diameter around 20 μm. The particulates were gold-coated to a thickness of around 6-to-7 nm and examined using backscattered electrons using a Phenom G-2 SEM (15 kV, 80 pA). The field-of-view (FoV) selected was larger than 10000 μm^2 and more than three repeat measurements were carried out for each the same sampling area (see Table 4-1). The slightly higher concentration of Ca (1-to-2 mol%) that is observed likely arises from the presence of 1-2 mol % $CaCO_3$ as vaterite (a hexagonal polymorph of $CaCO_3$),[173] as confirmed by X-ray diffraction.

Table 4-1: The composition of the dolomite used as compared to a reference composition.		
Simple carbonate	**Dolomite sample**	**Reference values for pure dolomite**
	mol %	**mol %**
$CaCO_3$	56.80 ± 3.4	54.35
$MgCO_3$	43.20 ± 3.4	45.65

4.2.3. X-ray Diffraction (XRD)

The mineral composition of the natural dolomite was examined using a Bruker D8-Advance powder x-ray diffractometer in θ-θ Bragg-Brentano geometry, using Cu-*K*α radiation (λ = 1.5406 Å) at an accelerating voltage of 40 kV and a beam intensity of 40 mA. A 2θ range of 20° to 75°, a step size of 0.02°, and an exposure time of 0.5 s/step were used. The XRD pattern of the sample is qualitatively similar to the International Centre for Diffraction Data (ICDD) reference for dolomite (Code: 00-001-0942) as shown in Figure 4-3. The presence of vaterite impurity was identified from the diffraction peak at 2θ = 26.64°.[174]

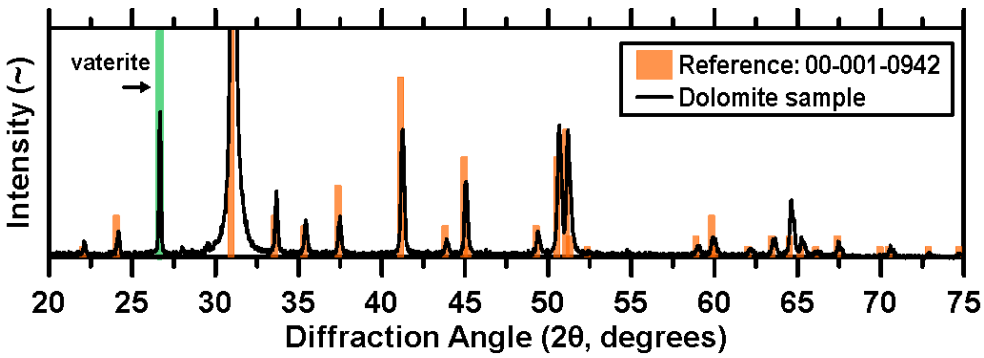

Figure 4-3: Representative X-ray diffraction patterns of powdered dolomite shown alongside the ICDD reference. The diffraction peak at 27° indicates the presence of vaterite impurity.

4.2.4. Fourier-transform infrared spectroscopy (FTIR) and Raman spectroscopy

FTIR was carried out on the pristine and irradiated calcite and dolomite samples using Attenuated Total Reflectance Fourier-Transform Infrared Spectroscopy (ATR-FTIR, PerkinElmer Spectrum Two) at room temperature. Here, polished calcite and dolomite surfaces were pressed using around 90 N of force onto a diamond/ZnSe composite crystal to ensure good contact and generate total internal reflection. The spectra reported herein were obtained by averaging 4 scans over the wavenumber range of 2000-400 cm^{-1} at a resolution of 1 cm^{-1}.

The peaks observed in a Raman spectrum arise from specific molecular vibration or rotation modes. Both the pristine and implanted dolomite samples were probed using a Renishaw inVia confocal Raman microscope with a laser beam of near-infrared wavelength of 532 nm. The laser penetration depth in Raman spectroscopy depends on the wavelength of the incident beam. The penetration depth for the spectra shown is around 0.7 μm for a wavelength of 532 nm, implying that the acquired signal is dominated by the material in the irradiation-affected (damaged) region. The spectra were obtained at 1 cm^{-1} resolution over 10 s of exposure of the CCD detector in the wavenumber region 0-2000 cm^{-1}. Three spectra were collected at 2 different areas on the mineral surfaces (each having a spot diameter of 100 μm).

4.2.5. Vertical scanning interferometry (VSI) for quantifying mineral dissolution rates

The dissolution rates of pristine and irradiated calcite and dolomite surfaces were measured using a flow-through cell (PermeGear) at room temperature (22 ± 1 °C). Alkaline solutions with pH 10, 12, and 13 – i.e., to mimic the chemical environment in concrete – were prepared by adding reagent-grade NaOH to deionized water (>18 MΩ·cm). The pH of the solutions was measured using a ThermoFisher Scientific Orion Versa Star Pro pH Benchtop Multiparameter Meter calibrated over the range of $2 \leq pH \leq 13$. The solutions were injected into

the cell (volume = 0.708 mL) at a flow-rate of 1.0 mL/min using a peristaltic pump. These flow conditions have been shown to be sufficient to prevent supersaturation with respect to phases such as $Ca(OH)_2$, $Mg(OH)_2$, $CaCO_3$, and $MgCO_3$.[175–179] The dissolution rates of calcite and dolomite were measured using vertical scanning interferometry (VSI) by observing the surface retreat after 2 hours of reaction for pristine calcite, 4 hours for irradiated calcite and 6 hours for pristine and irradiated dolomite. These periods of solution contact resulted in dissolution depths < 300 nm across all samples. This implies that the zone of the mineral that dissolves is well-within the ion-influenced regions as simulated using SRIM. A 50× Mirau objective (N.A. = 0.55, lateral resolution 0.163 μm) was used to measure surface height (change) over a total field of view (FoV) of 1374 μm × 974 μm. To offer a height reference for the VSI measurements, a portion of the sample surface was covered with an inert silicone mask (Silicone Solutions SS-38). Thus, the masked area that is revealed after peeling off the silicone mask serves as an unreacted "reference." The topographical images acquired were analyzed using Gwyddion (ver. 2.48). The absolute height difference between the reacted (dissolved) and masked areas when divided by the molar volume, and the period of dissolution reveals the molar dissolution rate. The error bars shown signify one standard deviation of the average dissolution rate for three unique samples. The dissolution rate for each sample is the average of at least three measurements made across different areas on the sample. Additional details on the VSI methodology can be found elsewhere.[120, 157]

4.3. Results and Discussion

4.3.1. Dissolution behavior of pristine and irradiated carbonates in alkaline solutions

Figure 4-4 shows the dissolution rates of calcite and dolomite before and following irradiation. Other dissolution rates of pristine calcite and dolomite as reported by Plummer *et al.* (1978), Busenberg *et al.* (1986), Chou *et al.* (1989), Shiraki *et al.* (2000), and Dolgaleva *et al.* (2005) are shown for comparison.[51, 164, 179–181] In general, it was observed that the dissolution rate remained unchanged for $6 \leq pH \leq 10$, and decreased thereafter as the pH increased, in relation to the increase in the carbonate-ion activity in solution.[182] The dissolution rate of carbonates in alkaline solutions is controlled by the pH-dependent concentrations of dissolved $H_2CO_3^*$, HCO_3^- and CO_3^{2-} at the solid-water interface.[183] In highly alkaline solutions, the sorption of hydroxyl ions by the mineral surface leads to a higher surface pH due to the formation of negatively-charged surface groups, which may reduce the rate of carbonate detachment.[183] It should be noted that although the literature data considered herein were obtained under the same pH,[51, 164, 179–181] the dissolution rates, especially of calcite, show considerable variability on account of differences including: particle size distribution, solution chemistry, sample source, etc.[179, 184] Nevertheless, our measured dissolution rates lie within typical ranges observed previously, and in fact agree closely with the data of Chou *et al.* obtained at 25°C.[51, 164, 179–181]

Overall, it was observed that the dissolution rate of dolomite is lower than that of calcite over the entire range of pH considered.[164] The slower dissolution kinetics of dolomite have been attributed to the rapid release of Ca^{2+}, which leaves the solid enriched in the $MgCO_3$ component whose protonation and hydrolysis control the overall dissolution rate.[185, 186] Although the dissolution rates for both the pristine and irradiated calcite are within the range of published values (see Figure 4-4), upon irradiation, a uniform decrease in, especially the dissolution rates of calcite, over the entire pH range probed was observed. This is postulated to

be on account of ion implantation, at the energies and fluence implemented herein inducing the reorganization of existing dislocations in the crystal structure in an effect similar to annealing,[187] which would result in a consequent reduction in the dissolution rate (and elsewhere, has been observed to result in an increase in calcite's hardness).[188, 189] This effect is more prominent in the case of calcite, i.e., rather than dolomite on account of the calcite being a pure and phase-oriented single crystal as compared to the natural dolomite sections. In the case of dolomite, irradiation appears to impose no effect on its dissolution behavior. Thus, it can be concluded that irradiation affects carbonate mineral dissolution rates in a much more limited manner than observed for silicates.[188, 190] For example, quartz, albite, and almandine have shown increases in their dissolution rate upon irradiation by a factor of 1000 times, 20 times, and 2 times, respectively.[11, 120, 157]

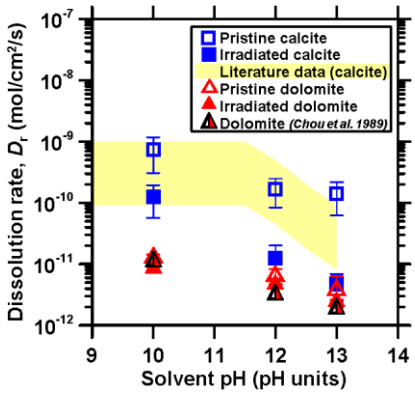

Figure 4-4: The dissolution rates of calcite (blue squares) and dolomite (red triangles) as a function of the solvent pH before (open symbols) and following (solid symbols) irradiation. The shaded region denotes the range of dissolution rates reported by Plummer *et al.* (1978), Busenberg *et al.* (1986), Chou *et al.* (1989), Shiraki *et al.* (2000), and Dolgaleva *et al.* (2005) for calcite dissolution under similar conditions (i.e., pH, flow rate, temperature).

4.3.2. Effect of irradiation on the atomic structure of carbonate minerals

Irradiation can significantly affect the crystal structure of minerals by altering: (i) coordination numbers, (ii) bond lengths, (iii) bond angles, and/or (iv) their medium-range order.[11, 120, 157] Such alterations, and defect formation can produce substantial structural changes, such as the loss of crystallinity, i.e., amorphization. Here, vibrational (FTIR and Raman) spectroscopy techniques were used to evaluate disordering. The main difference between these two techniques lies in the nature of molecular bonding that they assess. Specifically, whereas Raman spectroscopy measures the change in the polarizability of the molecular bond during vibration, FTIR measures the change in the dipole moment during vibrations.[191] The degree of structural disordering can be revealed using FTIR from (i) the number and the intensity of peaks, and (ii) the displacement of a given peak from its *reference* position.[93] For example, disordering is associated with a decrease in the number of FTIR peaks, and a shift of their positions toward lower wavenumbers.

Figure 4-5 shows the FTIR spectra of calcite and dolomite, before and following irradiation. The FTIR spectra of these carbonate minerals revealed known major peaks at 1435-1450, 876-881, and 712-730 cm^{-1} and minor peaks at 2530-2550 and 1812-1818 cm^{-1},[192] which are related to the stretching and bending modes of the CO_3^{2-} groups.[162, 192, 193] The similarity in the atomic structures of dolomite and calcite is reflected in their FTIR spectra. Notably, the two major absorption peaks of dolomite (i.e., around 876-881 and 712-730 cm^{-1}) lie between those of calcite and magnesite ($MgCO_3$).[193] Broadly speaking, the FTIR spectra of the irradiated carbonates are indistinguishable from those of the non-irradiated samples, especially for dolomite. Although some minor peak broadening at 876 and 712 cm^{-1} was

observed in the case of irradiated calcite (see Figure 4-5(a)), it is postulated to be on account of the ion implantation-induced reorganization of existing defects in the crystal structure,[187] which could have resulted in the observed reduction in dissolution rate as noted above. Previously, Nagabhushana *et al.*[162] showed a trend of reduction in the peak intensity and peak broadening upon ion implantation in calcite for peaks corresponding to the CO_3^{2-} group's bending and stretching modes. This was attributed to the breakage of carbonate bond (–C–O–) or changes in the crystallite size due to irradiation-induced volume expansion.[162] However, it should be noted that the implantation energy used by Nagabhushana *et al.* was 100 MeV, which is almost 3 orders of magnitude greater than what was used in the current study.

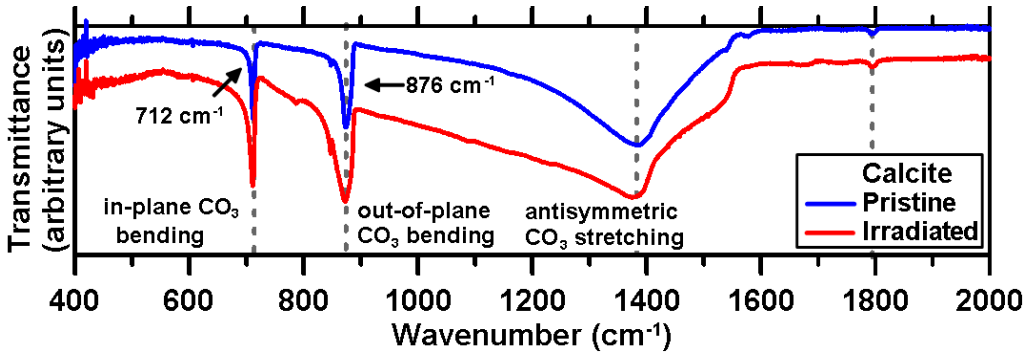

(a)

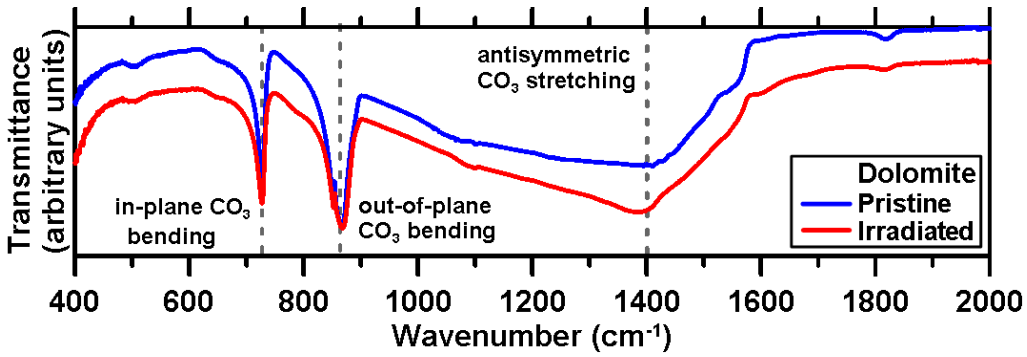

(b)

Figure 4-5: Representative FTIR spectra of **(a)** calcite and **(b)** dolomite in the 2000-400 cm^{-1} wavenumber region, before and following irradiation.

The Raman spectra of calcite and dolomite before and following irradiation, are shown in Figure 4-6. It is noted that similar to the FTIR observations, the positions and intensities of the 6 major peaks that characterize the chemical bonding of the carbonates remained fairly unchanged.[194, 195] These peaks which are described in Table 4-2 include: a major peak located at 1085 cm^{-1} (calcite) or 1100 cm^{-1} (dolomite), which reflects the symmetric CO_3^{2-} stretching (v_1),[194] two medium peaks at 280 (calcite) / 304 (dolomite) and 154 (calcite) / 179 (dolomite) cm^{-1}, which are assigned to external CO_3^{2-} rotational and translational modes, respectively,[194]and two weak peaks at 710 (calcite) / 725 (dolomite) and 1434 (calcite) / 1445 (dolomite) cm^{-1}, which are related to symmetric CO_3^{2-} deformation (v_4) and antisymmetric CO_3^{2-} stretching (v_3).[196] In addition, a peak located at 1747 (calcite) / 1765 (dolomite) cm^{-1} corresponds to a CO_3^{2-} internal mode that originates from the out-of-plane CO_3^{2-} ions bending (v_2) .[194, 196] Our data suggest that both the pristine and irradiated materials share similar chemical bonding modes on their surface, i.e., CO_3^{2-} stretching, rotation, translation, or bending. Therefore, the results of both the Raman and the FTIR spectra show that irradiation did not significantly alter the structure of carbonates, consistent with the results of Pignatelli *et al*., which employed cross-sectional transmission electron microscopy / selected area electron diffraction (SAED).[11]

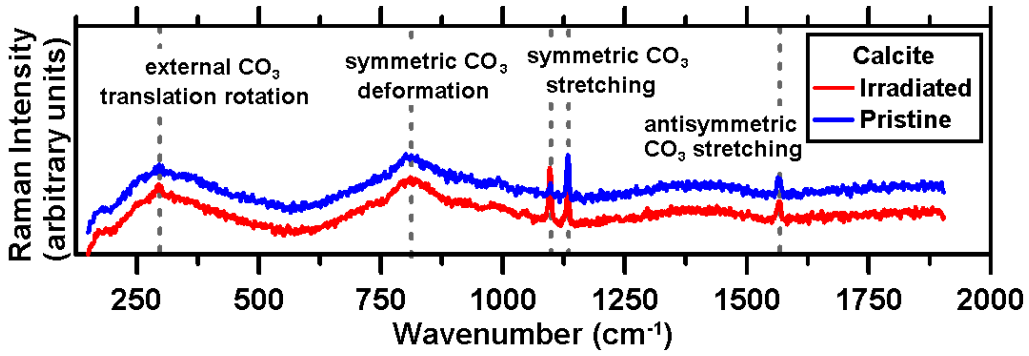

(a)

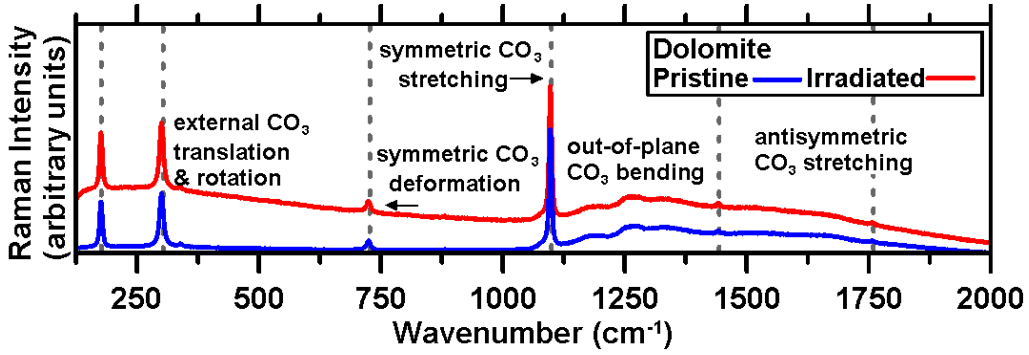

(b)

Figure 4-6: Representative Raman spectra of pristine and irradiated **(a)** calcite in the 0–2000 cm^{-1} wavenumber region, and **(b)** dolomite in the 125–2000 cm^{-1} wavenumber region. The peaks are essentially similar before and following irradiation. Fluorescence is more obvious when using a 532 nm laser as typical for a lower wavelength laser source. Although use of a lower wavelength source induced greater fluorescence, this source probes the depth of the material corresponding to the zone affected by irradiation.

Table 4-2: Relevant Raman peak positions and their corresponding vibration modes for calcite and dolomite. v_i denotes the various modes of vibration, where i = 1, 2, 3, 4)		
Calcite peaks (cm^{-1})	**Dolomite peaks (cm^{-1})**	**Vibrational mode**
154	179	External CO_3^{2-} translational modes[194]
280	304	External CO_3^{2-} rotational modes[194]
710	725	Symmetric CO_3^{2-} deformation (ν_4)[196]
1085	1100	Symmetric CO_3^{2-} stretching (ν_1)[194]
1434	1445	Antisymmetric CO_3^{2-} stretching (ν_3)[196]
1747	1765	Out-of-plane CO_3^{2-} ions bending (ν_2)[194]

4.3.3. New insights from molecular dynamics simulations into structure and reactivity

Molecular dynamics simulations provide direct insight into the effects of irradiation (ballistic impacts) on the structures of calcite and dolomite. For example, first, Figure 4-7(a) shows the evolution of the density of these two phases upon irradiation. In contrast to the behavior observed in silicates,[11, 120, 157, 197, 198] irradiation did not result in significant changes in the bulk densities of the carbonates. In fact, after deposition of 900×10^{18} keV of total kinetic energy, the simulated densities of calcite and dolomite remained effectively unchanged as compared to their initial (pristine state) values of 2.71 g/cm^3 and 2.89 g/cm^3, respectively, in agreement with previous observations.[168, 190, 199] In contrast, quartz has been shown to exhibit a 15% decrease in density, and complete amorphization, at the same radiation exposure conditions.[11] The significant volume expansion, and implied density reduction, that was indicated via our MD simulations for an incident energy of 1 keV[11] was later found to be an artifact stemming from an insufficient system size and relaxation time, which resulted in damage saturation of the system after a small number of high-energy collision cascades. This issue was avoided in the current study by using a larger system size, as demonstrated by Krishnan et al.,[171] or a smaller incident energy (600 eV). The electron paramagnetic/spin resonance (EPR/ESR) studies from Kabacińska *et al.* [200] indicate that changes in the hardness or elastic

modulus of materials may arise from electron spinning. Although our MD simulations do not take electronic behavior into account, the lack of change in the density as ascertained herein does not contradict the results of Kabacińska *et al.*[200], e.g., since density does not always scale with hardness as suggested previously.[201, 202] Furthermore, and in agreement with the vibrational spectroscopy observations, careful inspection of the simulated atomic structures – following irradiation – also did not reveal major structural damage in the calcite or dolomite structures. For example, only subcritical structural modifications (e.g., defect reorganization or distortion) were observed as indicated in Figure 4-5. As such, the substantial resistance of carbonate minerals to irradiation can be attributed to the non-directional nature of the ionic bonds (e.g., Ca–O and Mg–O bonds) in these minerals which can readily recover their initial geometry after radiation exposure, i.e., cessation of the ballistic cascade.[11] In general, the resistance to radiation-induced atomic alterations is dominated by the competition between the short-range covalent bonds (i.e., that induce localized electronic charge between neighboring atoms) and the long-range ionic bonds (i.e., that produce a collection of electrostatically-charged spherical ions).[203] As such, following exposure to ballistic collisions, the amount of structural alterations that result depends on the ability of the system to rapidly recrystallize; a process which is facilitated in primarily ionic systems which are able to rapidly regain their pristine – most thermodynamically favorable – structure.[203] This nature of rapid reorganization to the pristine state is hindered in dominantly covalently bonded systems, since the directional nature of atomic bonds prevents local structural reorganizations, thereby hindering the tendency for recrystallization resulting in the accumulation of atomic defects.[203, 204]

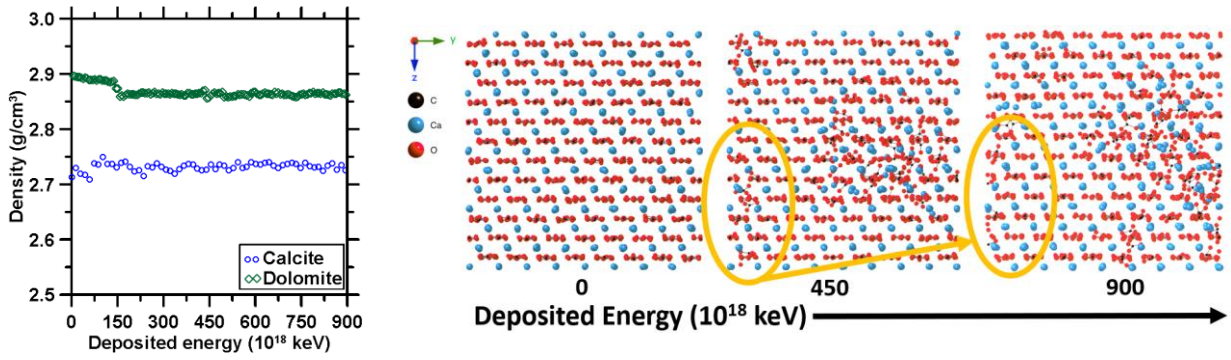

(a) **(b)**

Figure 4-7: (a) The simulated evolution of the density of calcite and dolomite as a function of the deposited energy, and **(b)** The transformation of calcite's atomic structure with increasing radiation exposure showing the atoms recrystallized (circled) after exposure to radiation.

Coming back to the issue of chemical durability (dissolution rates), recently Pignatelli *et al.* and Hsiao *et al.* have shown that mineral and glass dissolution rates are, to the first order, controlled by the topology of their atomic networks.[108, 120] Specifically, it has been highlighted that dissolution rates, for a given solution composition, are determined by the number of topological constraints per atom (n_c, unitless) as represented by an Arrhenius-like function:[108, 148, 205, 206] $D_r = D_{r0}\exp\left(\frac{-n_c E_0}{RT}\right)$, where D_r is the dissolution rate, D_{r0} is a rate constant that depends on the solution chemistry, R is the gas constant, E_0 is the energy required to break a unit topological constraint and T is the thermodynamic temperature. As such, the variation in the dissolution rates before and following irradiation can be expressed as: $\frac{D_r^{\text{irr}}}{D_r^{\text{prist}}} = \exp\left(\frac{-\Delta n_c E_0}{RT}\right)$, where D_r^{irr} and D_r^{prist} are the dissolution rates of the irradiated and pristine solute, respectively, and Δn_c is the variation in the number of topological constraints per atom upon irradiation.[120] By application of this framework, and from knowledge of the pre- and post-

irradiation dissolution rates, it is indicated that the limited change in the dissolution rates of calcite and dolomite, before and following irradiation is likely on account of the small, if any, change in the number of constraints. This conclusion is unsurprising since the MD simulations above also indicate that the connectivity (e.g., coordination numbers) of the atomic networks of calcite and dolomite remained unaffected by irradiation. This analysis confirms that, despite the small and potentially transient structural changes induced upon irradiation (e.g., distortion of the carbonate groups), irradiation does not induce significant permanent changes in the structure, and consequently the chemical durability of carbonates.

4.4. Conclusion

Taken together, by using Ar^+ implantation as a proxy for neutron irradiation, this study evaluates the extent of damage that calcite and dolomite—two archetypical carbonate minerals—experience after irradiation by probing changes in both atomic structure and dissolution kinetics, i.e., reactivity. As such, our results highlight that irradiation induces substantially smaller – and if anything, conservative (i.e., the reactivity reduces) changes – in the chemical durability (i.e., mineral dissolution rates) of carbonates as compared to common silicate minerals (i.e., that are fully polymerized, and in which the silicate-groups are percolating). This can be explained by the fact that the atomic structures and connectivity of the carbonate phases remain broadly unaffected by irradiation. This behavior arises from their non-directional ionic bonds, which can recover their initial geometry after each ballistic cascade. This is why, radiation damage in carbonates, even if induced presents a reversible character.[188] Because the resistance to irradiation-induced structural alternation is controlled by the competition between the covalent bonds and the ionic bonds in the system, the ability for a structure to recrystallize to its

thermodynamically most favored state depends mostly on its ionic nature. Conversely, this recrystallization process is hindered in structures that are covalently bonded, whose directional character inhibit structural reorganizations, thereby retaining structural defects. These conclusions are supported by our MD simulations which reveal no changes in the atomic densities of both calcite and dolomite after exposure to irradiation, in an ideal system (i.e., no impurities or defects),[168, 190, 207] although the sample may indeed experience some form of defect reorganization that could decrease their aqueous dissolution rates. This is unlike the case of framework silicate aggregates whose volumetric expansion, change (reduction) in mechanical properties, and reduced chemical durability render them poorly suited for use in nuclear concrete construction. This suggests that it would be appropriate to especially prescribe and specify the use of (solely) carbonate-based aggregates in the design and construction specifications of nuclear power plants and other relevant facilities.

Chapter 5 Electric Potential–Induced Dissolution Kinetics of Calcite in Salt Solutions

5.1. Introduction and Background

The dissolution kinetics of mineral is of interest to environmental and geochemical communities, so the dissolution rates have been measured for such purposes as the study of sedimentary rock evolution,[208] the pH of sea water,[209] the neutralization of acidic lakes,[210] and natural weathering processes for decades.[210] One way to control mineral dissolution and precipitation kinetic is by exploiting electric field to the mineral surface or in the solvent. The fundamental understanding of potential-induced alteration in dissolution kinetics is important because it can broadly improve engineering applications. For example, calcite ($CaCO_3$) acts as an electrolyte material in mineral based fuel cell (i.e., solid oxide fuel cell (SOFCs)),[211] influences the soil transportation in electrokinetic remediation,[212] and improves the phosphatic fertilizers manufacturing.[213, 214] As well-known, calcite's dissolution kinetic and mechanism are strongly affected by solvent pH,[183, 215, 216] solution saturation condition,[217] solution chemistry,[177] temperature.[215, 216] Although it is well accepted that acidic pH,[215, 218–220] higher electrolyte ionic strength (I),[177] and higher temperature,[215, 216] all increase calcite dissolution rate, the studies of the electric potential effect to mineral dissolution enhancement in the presence of electrolytes are still unidentified.

Earlier study, which was focusing on the electrogenerated proton by water hydrolysis process when applied electric potential into electrolytes, found out that potential-generated protons acidify local solvent around the anode and thus enhanced the calcite dissolution.[221, 222] Although previous investigators recognized the importance of potential induced proton flux on the rate of calcite dissolution, they were more focusing on how to generate the simulation

model, in order to visualize the proton concentration and the diffusive flux of the protons. On the other hand, the discussion regarding potential-induced ion transportation and potential-altered electric double layer (EDL) could be interesting, and also need to be taken into consideration. Since at potentials lower than 1.2 V (i.e., water hydrolysis potential at pH 6.5), where acidification is excluded, a mechanism that enhances calcite dissolution is by changing the EDL structure and enhancing the ion transportation. The mineral dissolution is controlled by two processes that commonly occur in sequence: (1) The dissolution reaction at the interface between solid and liquid (i.e., surface reactions), and (2) the diffusion of reactive species (i.e., dissolved ions, ions from electrolyte solutions) in the aqueous phase to and from the interface. Barton *et al.* concluded that the dissolution of limestone in sulfuric acid solution in the pH range 2-6 was controlled by proton diffusion to the surface.[223] Rickard *et al.* (1983) and Sjoberg *et al.* (1984) demonstrated that the rate of surface reaction for calcite dissolution in solutions of intermediate to alkaline pH can be considered to reaction-controlled.[215, 224] Building on these prior studies, the present paper provides an analysis of how electric potential affects mineral dissolution, especially for calcite (i.e., diffusion-controlled at acidic to neutral pH environment).

Ion transport in electrolytes under electric potential has recently received increasing attention for mineral dissolution, therefore it is critical to understand the potential-induced ion transportation in nanoscale (i.e., within EDL or solutions) or in the bulk solution. In view of this, the purpose of the present study is to study and investigate the nature of ion transport-induced mineral dissolution under an electric field. As solid surfaces contact with electrolyte solutions, the EDL formed. The origin of this EDL is due to the adsorption of ions to mineral surface, and the ions attracted by the Columbic force from the surface charged sites, in order to maintain the electroneutrality of the surface.[144, 225] Figure 5-1 schematically illustrates the general

structure of EDL. If we assumed the surface is negatively charged (i.e., calcite), a layer of protons or hydroxyl ions in the solution are rigidly adsorbed on the surface, and create a compact layer of relatively immobile ions, which is also known as Inner Helmholtz Plane (IHP), on the mineral surface.[144] The excess ions that are attracted by Coulombic force beyond the Inner Helmholtz Plane (IHP) are able to diffuse and be affected by electric field since those attracted ions are loosely bonded.[144, 226] For this reason, the movement of ions and the properties (i.e., compactness, thickness, surface potential) of the EDL are worth to be discussed and addressed. Nernst-Planck equation is used to quantify the potential-induced ion transportation (i.e., ion diffusion) that would potentially affect mineral dissolution. Up to now, a comprehensive dissolution kinetics theory regarding the effect of the electric potential on minerals is poorly established.

In this work, we first induce the changes in the ion concentrations in the bulk solution and the changes in the EDL structure near the solid-liquid interface by varying the solution ionic strength, and evaluate the effect of such change to the enhanced mineral dissolution, mostly calcite without applying electric potential. Then, the potential-induced ion transportation was examined by accessing the calcite dissolution rates under varying solvent pHs and also on orthoclase ($KAlSi_3O_8$) dissolution (i.e., surface controlled at room temperature),[227] so as to validate that the dissolution mechanism should be taken into consideration for potential-induced dissolution rates. The Nernst–Planck equation was used to describe the effect of potential-induced ion transportation to mineral dissolution.[228] After that, the enhancements of potential-induced calcite dissolution rates are compared between different solution ionic strengths (I), since the ion diffusivities are dependent on solution ionic strength (i.e., the solution viscosity) following Stokes-Einstein Equation.[229] Furthermore, the effect of external potential

under different temperatures was investigated, in order to examine whether the similar phenomena happens in all ranges of temperatures, and also help estimate the activation energy needed for dissolution process under applied potentials. Overall, this work clarifies the external potential effect to calcite dissolution kinetics under different ionic strength of electrolytes, solvent pHs and temperatures.

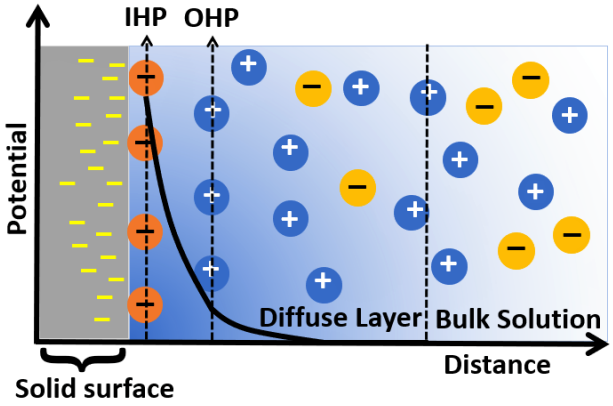

Figure 5-1: Illustration of the electrical double layer (EDL) near the mineral surface (i.e. calcite). The inner Helmholtz plane (IHP) is the plane cutting through the center of the chemically adsorbed species, and the outer Helmholtz plane (OHP) is the plane cutting through the closest ions that is attracted. The concentration of ions in the diffuse layer decreases as the distance departs away from the surface, and the zeta potential (ζ) is defined as the potential difference between OHP and the bulk solution. The ions beyond OHP are able to move freely.

5.2. Materials and Methods

5.2.1. Materials

Pure natural Iceland spar calcite was sourced from Ward's Science Company.[230] The bulk samples were powdered using ball mill and successively sieved through the No. 140 sieve (106 μm). The particle size distributions (PSDs) of the calcite particulates were determined by static light scattering (SLS, LS13-320, Beckman Coulter).[231] The mixture of isopropyl alcohol (IPA) and calcite particulates was ultrasonicated for 30 seconds prior the measurements to ensure the solids are well suspended. The particle size analysis indicates a median diameter (d_{50}) is of 101.10 μm, and the specific surface area (SSA) of calcite was calculated to be 244.90 cm^2/g.

The selected concentrations of electrolyte solutions (0.001, 0.01, 0.1 and 1 M) used for dissolution experiments were prepared by adding reagent grade sodium chloride (NaCl) into Milli-Q deionized (DI) water (>18 MΩ·cm) and adjusted to the desired pH (pH 4, 8 and 10) with hydrochloric acid (HCl) and sodium hydroxide (NaOH), respectively. The solution pH was measured using a ThermoFisher Scientific Orion Versa Star Pro pH Benchtop Multiparameter Meter calibrated over $2 \leq pH \leq 13$ at 22 ± 1 °C.

5.2.2. Zeta potential measurement

The zeta potential measurements were carried out by first suspending 1 g of calcite particulates ($d_{50} \approx 100$ μm) in 100 mL DI water mixed with saturated calcite solution to prevent further dissolving during measurement, and 0.5 mL of the suspension was added into 100 mL NaCl electrolyte solutions with the selected ionic strength of 0.001, 0.01, 0.1 and 1 M NaCl. The test solutions were ultrasonicated for 1 minute before which 1.5 mL of suspension was placed into a cuvette for zeta potential measurement. The zeta potentials were measured using a ZetaPALS Potential Analyzer from Brookhaven Instruments Corp.[127] For each measurement,

10 replicates were obtained and then averaged to obtain representative data. The value presented here was at least repeated for 3 times, thus 30 points were measured.

5.2.3. Measuring calcite dissolution rates using inductively coupled plasma – optical emission spectrometry (ICP-OES)

To investigate the electrical potential effect on mineral dissolution, 3–electrode system attached with a potentiostat (VersaSTAT 4, Princeton Applied Research)[232] was adopted. The working electrode is a platinum (Pt) wire (probe radius: 0.5 mm, length: 32 mm, CH Instruments, Inc.),[233] reference electrode is a Ag/AgCl wire (probe radius: 0.5 mm) in a 4 mm diameter glass tube containing 1 M potassium chloride solution (CH Instruments, Inc.),[233] and the counter electrode is a steel foil with the dimension of 1 cm × 3 cm. The working electrode and reference electrode were aligned and the distance between is set to 0.5 cm. Illustration of the experimental setting system is shown in Figure 5-2.

For dissolution experiments, the 100 mL jacketed reaction beaker was connected to water circulating bath (Polyscience)[234] to sustain the experimental temperatures (20°C, 40°C and 60°C). 0.1 g calcite was uniformly dispersed in 50 mL NaCl solution (solid-to-liquid ratio of 1:500) with the 3 electrodes (working, reference and counter electrodes), and afterwards a constant potential of 0, 0.001, 0.01, 0.1, 0.2, 0.3, and 0.4 V versus reference electrode were applied during the total dissolution duration (12 min for calcite and 2.5 hours for orthoclase). The initial dissolution rates of minerals were determined from the slope of dissolved ions concentrations (e.g. Ca for calcite and Si for orthoclase)-time curve from 0 to 12 minutes (or 2.5 hours) using inductively coupled plasma-optical emission spectrometry (ICP-OES, PerkinElmer Avio 200) in axial view,[235] and then normalized by the initial surface area that is determined

by static light scattering. The solvent solutions were collected every 3 minutes (i.e., 0, 3, 6, 9 and 12 minutes of reaction) for calcite, or every 0.5 hours (i.e., 0.5, 1, 1.5, 2 and 2.5 hours of reaction) for orthoclase. A small quantity (~1.2 mL) of the solution was passed through 0.2 μm nylon syringe filter, and later diluted 2× with 5% by volume nitric acid for ICP-OES analyses. For each tested condition, at least 3 replications were obtained. In order to compare with the electric potential-induced dissolution rates, a set of controlled experiments (i.e., dissolution rates measured without potential in selected electrolyte concentrations) were designed and conducted. In addition, thermodynamic simulation (i.e., solution saturation index (SI), solubility product constant (Ksp)…etc.) were conducted using PHREEQC, and suggesting that all the solutions are undersaturated during the dissolution process with respect to calcite phases. SI calculated using PHREEQC simulation by inputting the final ion concentration in solvents measured using ICP-OES were all around the value of -5, which are then suggested to be within transition equilibrium state (-60 kJ/mol < ΔG < -25 kJ/mol). Though the solution does not maintain in far from equilibrium state at the end of measurement due to the rapid carbonate dissolution, we make sure the solution does not end up in near-equilibrium condition to filter out the influence of solution when applied electric potential. In our experimental setting, the dissolution of the minerals results in a maximum increase in the ionic strength of 0.01 M under applying electric potential.

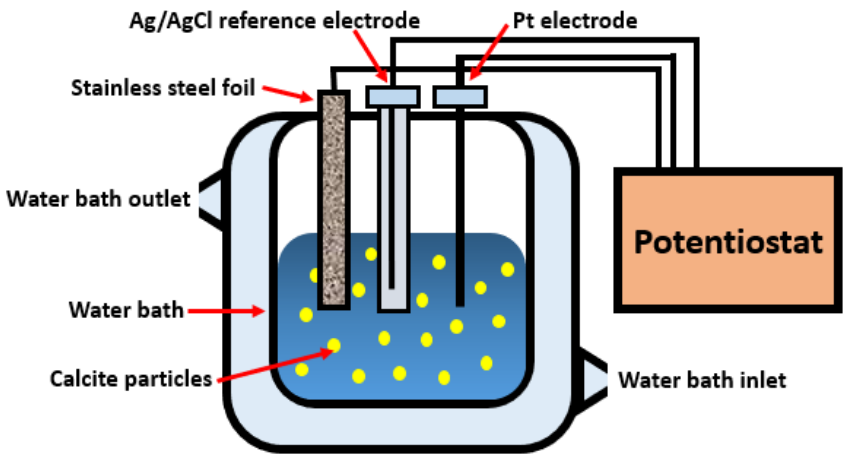

Figure 5-2: An illustration of the experimental setup (3-electrode system with a potentiostat). The working electrode is a Pt wire, reference electrode is a Ag/AgCl wire in a glass tube containing 1 M KCl solution, and the counter electrode is a sheet of steel foil. The water bath is applied to sustain the experimental temperature (e.g. 20°C, 40°C and 60°C).

5.3. Results and Discussion

5.3.1. The effect of ionic strength on calcite dissolution kinetics

By varying the solution ionic strength, we noted that calcite dissolution rates increased a factor of 2.2 (see Figure 5-3(a)) at 1 M NaCl. Since NaCl is fully dissociated in aqueous solutions, adjusting its concentration influences calcite dissolution mainly through the solvent ionic strength (I).[236] Rickard *et al.* previously measured the calcite dissolution rates in different ionic strengths of KCl and NaCl solutions, and suggesting that calcite dissolution rate is determined by the ion activities in the solutions (i.e., solution saturation state) using the equation of

$$\text{Rate} = kA(\sqrt{K_{sp}}\text{-}\{Ca^{2+}\}^{0.5}\{CO_3^{2-}\}^{0.5}) \qquad \text{Eq. (5-1)}$$

, where k is the rate constant, A represents the surface area, K_{sp} stands for the solubility product constant of calcite (e.g. log(K_{sp}) = -8.46 at room temperature calculated from PHREEQC simulation),[87] and $\{Ca^{2+}\}$ and $\{CO_3^{2-}\}$ are the activities of Ca^{2+} and CO_3^{2-} in the bulk solution.[224] The ionic strength influences the activities of each type of ions individually and thus the calcite dissolution rates. As the activities of Ca^{2+} and CO_3^{2-} decreased with ionic strength, the difference between $\sqrt{K_{sp}}$ and $\{Ca^{2+}\}^{0.5}\{CO_3^{2-}\}^{0.5}$ becomes greater in higher ionic strength solutions, which generate a larger driving force for dissolution process.[236] From our calculation using PHREEQC, with the *pitzer.dat* database, the activities of Ca^{2+} and CO_3^{2-} in NaCl electrolytes with the ionic strength range of I = 0.0 to 0.1 M decreased from 1.11×10^{-4} to 9.45×10^{-5} for Ca^{2+}, and increased from 3.75×10^{-5} to 4.42×10^{-5} for CO_3^{2-}, respectively. The ion activity coefficient (γ) for Ca^{2+} and CO_3^{2-} are also suggested to decrease with ionic strength.[237] According to Eq. 1, this range of ionic strength (e.g. 0 to 0.1 M) is equivalent to a rate enhancement of 2%, which is lower than our experimental results (i.e., more than 2 times higher at 0.1 M than 0 M). As a result, the ion saturation state (i.e., ion activities from the bulk solvents) may not be sufficient to fully explain the enhancement in dissolution rates when increasing ionic strength in Figure 5-3(a).

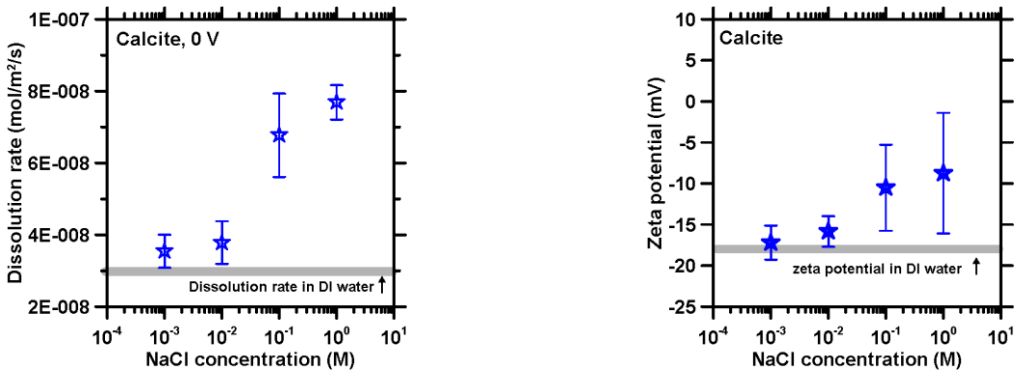

(a) **(b)**

Figure 5-3: (a) Dissolution rates and the **(b)** zeta potential of calcite measured in NaCl solutions with the presence of 0.001 to 1 M NaCl at room temperature, showing that the trend of calcite dissolution rates follows the evolution of zeta potential of calcite particles in varying ionic strength (I) of NaCl solutions.

Besides, altering the solution ionic strength influences the structure and the interactions of ions inside the EDL of calcite as well. The influence of ionic strength on the EDL can be inferred from zeta potential measurements. We observed that the absolute value of our measured zeta potential decreased with solution ionic strength from -18 mV at 0.001 M to -5 mV at 1 M, similar to previous measurements (i.e., -14 mV at 0.04 M NaCl and -4 mV at 3 M NaCl from Mahrouqi *et al.*).[238, 239] The published zeta potential on calcite are not consistent, and the large discrepancy of the previous measured value (i.e., magnitude and the sign of the zeta potential) depends on the measurement conditions (i.e., streaming potential or static potential) and the source of materials.[240] The larger error bar in higher ionic strength (1 M) from our measurement (Figure 5-3(b)) is due to the short Debye length. The Debye length is crucial when measuring zeta potential, especially in high ionic strength, the compression of the diffuse layer in high ionic strength solution makes it harder to determine the spatial distribution and

concentration of the ions in the EDL.[241] Unlike in silica, the zeta potential-determining ions for calcite are not protons (H^+) or hydroxyl ions (OH^-), but Ca^{2+}, CO_3^{2-}, HCO_3^- and $H_2CO_3^0$ in the solutions.[242] At the solid-liquid interface, ions are chemically bonded to the surface sites, and create surface sites such as $CaOH_2^{+0.5}$, $CaOH^{-0.5}$, or $CO3^{-0.5}$, which are the species affecting the value of the zeta potential for calcite. Zeta potential decreases in magnitude with increasing concentration of ions such as Na^+ or Cl^-, reflecting a shrinkage of the thickness of EDL.[238, 243] From the discussion above, the crowding of both anions and cations in the EDL in high ionic strength solution increases the interaction between ions, as shown in Figure 5-4. A large volume of ions is attracted on the mineral surface, resulting a more compact EDL and a smaller absolute value of the zeta potential (Figure 5-4). The reduction in zeta potential is well in agreement with the reduction in particle stability, which eases aggregation to happen.[244] Although the zeta potential value we obtained are all within the range that particles are likely to aggregate ($-30\ mV < \zeta < +30\ mV$), the attraction force between particles are greater in higher ionic strength solution.[245] Under this circumstance, the greater driving force at high ionic strength solution increases the mobility of calcite particles that would further enhance the calcite dissolution rate (e.g. mass transport controlled). On the other hand, ions in a dilute solution have less interaction and tend to disperse uniformly, so a thicker diffuse layer of the EDL persists. To sum up, increasing ionic strength results in dissolution rate enhancement through increasing undersaturation, and destabilization of the EDL.

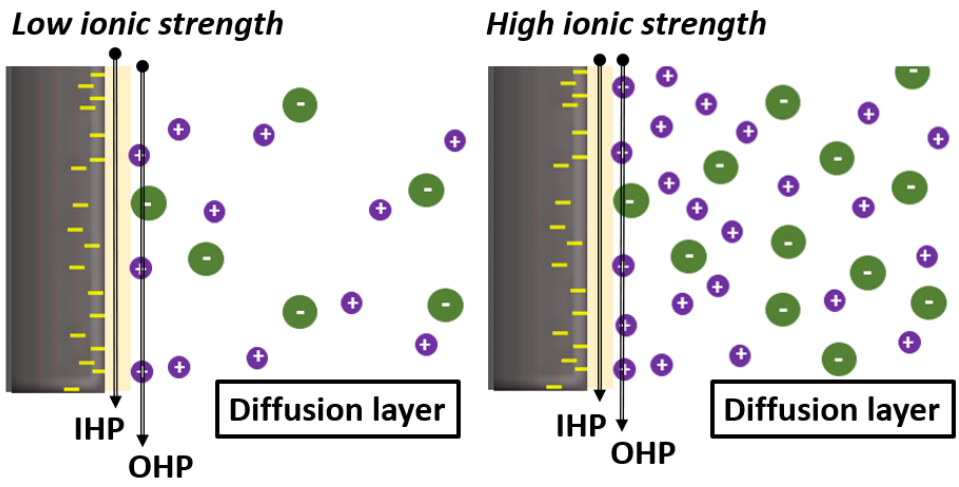

Figure 5-4: Illustration of calcite surface in low and high ionic strength NaCl solutions. Part of the ions are specifically adsorbed on the calcite surface at the inner Helmholtz plane (IHP, yellow region). The ions (Na^+, Cl^-) locate beyond IHP are attracted by the surface charge by Coulombic force only, which are moveable as applying electrical potential. Model is taken from Stipp *et al.* for surface speciation and Bazant *et al.* for the structure of EDL.[242, 246] **(**Shown in the schematic are Na^+ (purple), Cl^- (green), surface adsorbed ions layer (yellow).)

5.3.2. Effect of applied potential on surface- and transport-controlled dissolution

The effect of applied potential was then investigated by fixing the solution ionic strength at 0.01 M and altering the solvent pH from 4 to 10. The alteration of calcite's EDL structure by varying the solvent pH is assumed to be relatively negligible, since the published calcite's zeta potential within this pH range (pH 4-10) are less than 10 mV,[247] and the corresponding calcite dissolution rates to this range of zeta potential are around 2.2× (e.g. measured from Sec. 3.1), which is much less than the calcite dissolutions that varies by solvent pH from 4 to 10. Calcite dissolution rate increased about one order of magnitude from pH 4 to pH 6.5. From Figure 5-5, we noted that dissolution rates of calcite are stimulated by external electric potential in acidic to

neutral pH environment (pH 4-6.5), while the rates remain constant in pH 10. Within this pH range, calcite dissolution is considered as mass-transport controlled (pH 4) and mix-kinetic controlled (pH 6.5),[215, 248] therefore, the potential-enhanced ion transportation (i.e., ion flux) in the electrolyte is able to increase calcite dissolution rates.[249] On the other hand, calcite dissolution remains constant at pH 10, due to the interface-controlled dissolution at solvent pH higher than 8.[183, 250]

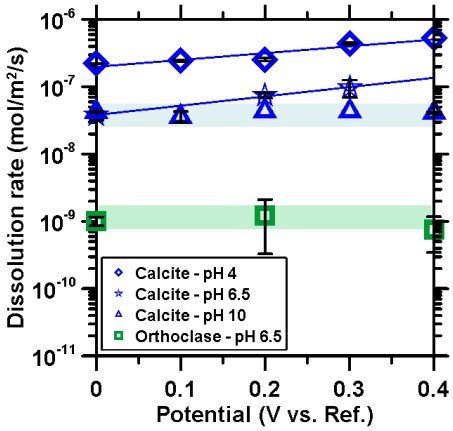

Figure 5-5: The logarithm dissolution rates of calcite and orthoclase across a wide range of applied electric potential at pH 4, 6.5 and 10, showing that only the calcite dissolution rates at acidic to neutral regime are increased (i.e., mass diffusion controlled), whereas adding electrical potential does not influence calcite dissolution rates at pH 10, and the dissolution rates of orthoclase (i.e., surface reaction- controlled).

The general principles of mass transfer theory are based on the existence of a diffusion boundary layer. A concentration gradient is confined to the boundary layer, and the mass transfer rate is approximately proportional to the concentration difference across the boundary layer.

$$j = k_t(c_b - c_s) \qquad \text{Eq. (5-2)}$$

, where j equals to ion diffusion flux density, k_t is the mass transport constant, and c_b, c_s are the concentration at the bulk and surface in the solution. For dissolution from a surface of area A into a fluid of volume V, mass balance dictates that the rate of change of concentration (c) in the bulk solution is

$$\frac{dc}{dt} = \frac{A}{V} j \qquad \text{Eq. (5-3)}$$

The ion motion can be estimated using "Nernst–Planck equation", as expressed in Equation (5-4). Ion diffusion flux density (j) is determined by both the gradient of ion concentration gradient and the electric field (i.e., the first and the second term on the right-hand side of Equation (5-4), respectively). The second term, electric field ($E = -\nabla\varphi$), is added to represent the electrostatic force that is caused by the external electric potential.[228]

$$j = -\left[D\nabla c + \frac{Dze}{k_B T} c(\nabla\varphi)\right] \qquad \text{Eq. (5-4)}$$

, where D is the ion diffusivity, z is the valence of ionic species, e is the elementary charge, k_B is the Boltzmann constant, and T is the temperature. Equation (5-4) is based on the assumption of fluid velocity equals to zero (i.e., only the motion of ion species) and the external electric potential is steady state.[228] From the Nernst–Planck equation, we noted that ion flux (j) is proportional to the external electric field ($E = -\nabla\varphi$). Additionally, we noted that the ion flux is proportional to mineral dissolution rate from Equation (5-3). Therefore, greater ionic flux stimulated by electric potential may enhance the dissolution rates, and also the motion of ions (i.e., potential-induced ion flux). Besides, the extent of the potential-induced ion transportation speed in the electrolyte follows the same trend of the voltage generated by the electric field in our study. The calcite dissolution rates are greater at 0.4 V than 0.1 V (Figure 5-5). During surface-controlled dissolution (pH 10), calcite dissolution rates in the alkaline solutions (pH 10)

are not influenced by external electric potential.[248, 251] A similar observation (i.e., non-changing dissolution rates as electric potential) was obtained for orthoclase ($KAlSi_3O_8$), see Figure 5-5, a mineral of moderate dissolution rate compared to quartz (SiO_2) and which also features a surface-controlled dissolution at pH 6 under room temperature.[227] As a result, alternating the external potential simply affects the ion mass transport in the liquid, and suggests that silicate dissolution rates which are controlled by surface reactions, are not affected. However, the potential induced ion motion depends also on the ionic solution, solution viscosity, and solution temperature as well, which will be discussed in detail later (Sec. 3.3 and Sec. 3.4).

5.3.3. Effect of ionic strength on potential-enhanced transport-controlled or mix kinetic-controlled dissolution

In Figure 5-6(a), the measured calcite dissolution rates are plotted as a function of E based on the relationship between the ion flux (j) (i.e., dissolution rate) and the electric potential (E) by using Equation (5-3) and (5-4). We observed that calcite dissolution rates did not significantly affected by applied potential over the range of 0.001–0.01 V for a fixed I (not shown in Figure 5-6(a)), whereas increased dramatically as the electric potential starting from 0.1 V at all NaCl concentrations (e.g. 0.01–1 M, Figure 5-6(a)). In addition, although calcite dissolution rates generally increased with electric potential, the extent of enhancement of calcite dissolution rate (i.e., ratio of dissolution rates at 0.4 V to 0.1 V) decreased with solution ionic strength (Figure 5-6(b)). That is, the potential induced dissolution rate is more dramatic in solution with lower ionic strength (0.01 M) than in the one with higher ionic strength electrolyte (1 M).

In Figure 5-6(b), the dissolution rate enhancement is plotted as a function of ion

diffusivity, which is calculated using "Stokes-Einstein Equation" (Equation (5-5))[229] under each specific solution ionic strength.

$$D = \frac{k_B T}{6\pi\eta_s R} \quad \text{Eq. (5-5)}$$

, where k_B is Boltzmann constant (1.38×10^{-23} $m^2\cdot kg/s^2\cdot K$), η_s stands for solvent viscosity (e.g. NaCl solution), R corresponds to solute radius (i.e., average ion radius Na^+ and Cl^- = 0.142 nm), and T is the temperature. The viscosity values of NaCl solution (i.e., from 0.01 M to 1 M) are attained from Ozbek *et al.*, in which the published data shows that the relative solution viscosity (η_r) increases with the NaCl molarity (M) (e.g. $\eta_r = 1 + A\sqrt{M} + BM + CM^2$, A, B, C are temperature dependent coefficients),[252] and is assumed not to alter over time during calcite dissolution. Since a stronger ionic strength solution results in a higher solution viscosity and a lower ion diffusivity, we noted that the calculated ion diffusivities decrease around 1.7× as the solution molarity increased one order of magnitude for the case of NaCl (i.e., the x-axis in Figure 5-6(b)). The calculated diffusivities are 2.0×10^{-7} m^2/s at 0.01 M, 1.2×10^{-7} m^2/s at 0.1 M, and 6.0×10^{-8} m^2/s at 1 M, which is a factor of 2.89× (e.g. 1.7×1.7) decrease in diffusivity from 0.01 M to 1 M. Moreover, the dissolution rate enhancement under different solution ionic strength is perfectly aligned with the calculated ion diffusivity, as shown in Figure 5-6(b). Looking back into the Nernst–Planck equation (Equation (5-4)), if the comparison of the same applied potential is made, the potential-induced ion flux is proportional to the ion diffusivity that is controlled by the solution ionic strength. As a result, smaller ion diffusivity that is induced by ion crowding in high ionic strength electrolyte decays the dissolution rate enhancement while applying electric potential.

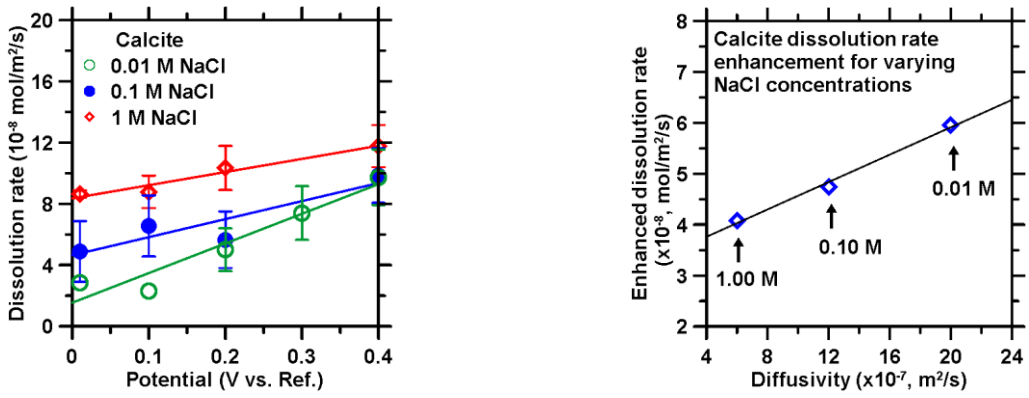

(a) **(b)**

Figure 5-6: (a) The dissolution rates of calcite as a function of electric field (E versus the 1 M KCl reference electrode) at varying ionic strength solution, showing that significant increase in dissolution rates take place in 0.01 M NaCl solution, whereas the dissolution rates increase slowly in 1 M NaCl electrolytes. The initial solvent pH is measured to be around 6.3, which is suggested to be in mixed kinetic regime. **(b)** The dissolution rate enhancements of calcite with varying calculated diffusivity that is controlled by ionic strength (i.e., solution viscosity), showing that adding electric potential affects low ionic strength solution greater.

5.3.4. Temperature-dependence of rate enhancement

In Figure 5-7(a), we observed that the calcite dissolution rates increased more than one order of magnitude as applied potential under room temperature at the potential of 0.4 V. However, the electric potential influences greater at room temperature than in high temperature, and the calcite dissolution rates even remain constant under high temperature. By combining Equation (5-4) and (5-5),

$$j = -\left[\left(\frac{k_B T}{6\pi\eta_s R}\right)\nabla c + \frac{ze}{6\pi\eta_s R}c(\nabla\varphi)\right] \qquad \text{Eq. (5-6)}$$

the temperature is only controlling the first term on the right-hand side of Equation (5-6). As the temperature increases, the ion flux that is induced by electric potential decreases, because the first term on the right-hand site (e.g. $(\frac{k_B T}{6\pi\eta_s R})\nabla c$) in Equation (5-6) will be the dominant term that contributes the ion flux at high temperature, not the electric potential. Therefore, this may be the reason why potential effect is less noticeable in high temperature. Accordingly, applied electric potential to mass transport-controlled mineral dissolution process potentially provides energy (e.g. driving force) to increase the motions of ions. However, the energy contributed by electric potential is limited compared to the temperature effect, so the rate enhancement by applied potential not significant at high temperature.

We also observed that the equivalent calcite dissolution rates at an extreme acidic (pH 2 HCl) and high temperature (60°C) conditions when applied electric potential. Under these two circumstances, where calcite dissolution rates are highly regarded as mass-transport controlled,[248] further supporting that once the ion transportation speed is fast enough (i.e., thermal energy provided by temperature), the calcite dissolution rates are not influenced by external electric potential. Although the calcite solubility is suggested to decrease with temperature (i.e., K_{sp} changes from -8.45 (20°C) to -8.76 (60°C) from PHREEQC simulation),[253, 254] the saturation indexes (SI) calculated using PHREEQC using the concentrations of dissolved ion species are ranging from -4 to -5.33, indicating that the solutions are still under saturation. In addition, the corresponding Gibbs free energies (ΔG) are ranging from -30 to -25 kJ/mol as the temperatures varying from 20°C to 60°C, thus suggesting the dissolution process is within transition equilibrium state range.[89]

The activation energies (Ea) were acquired by fitting the measured potential-induced calcite dissolution rates with a range of temperatures using Arrhenius relation (Figure 5-7),[255]

which provides insights regarding the energy needed for potential-induced dissolution process. The calculated activation energy at 0 V (Ea = 47 kJ/mol) is in agreement with the literatures,[215, 251] whereas decreased with external potentials (0.1, 0.2, 0.3 and 0.4 V) as shown in Figure 5-7(b), the value reduced from 46 kJ/mol to 26 kJ/mol, which is more than 40 percent. Though no further evidence showing how the activation energy decreased when applied electric potential at room temperature, the fact that applied potential to electrolyte suspension ease the calcite dissolution reaction is demonstrated, and the activation energies needed to initiate dissolution process are measured to be reduced.

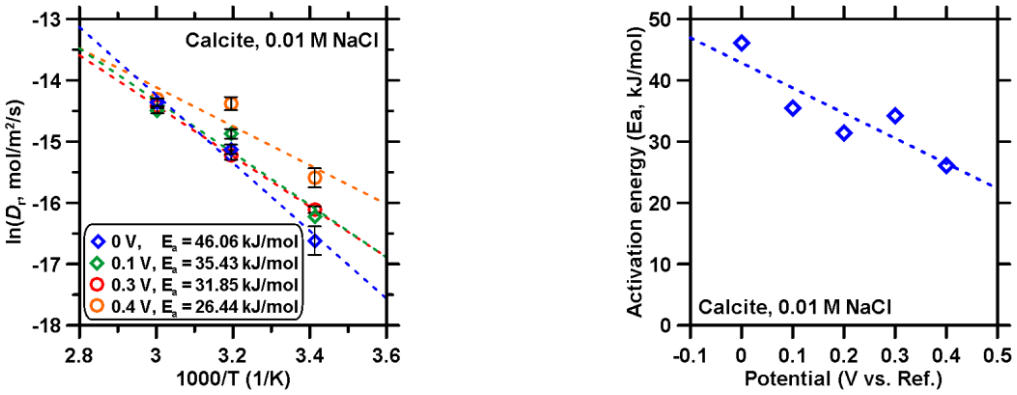

(a) **(b)**

Figure 5-7: (a) Calcite dissolution rates with temperatures 20°C, 40°C and 60°C under external potential (from 0 V to 0.4 V), indicating that electric potential affects significantly at room temperature. The solvent pH is measured to be around 8.2–8.4 during the dissolution process. **(b)** The activation energies (E_a) calculated from Figure 5-7. **(a)** decrease with the external potential.

5.4. Conclusion

This study demonstrates that electric potential has significant effect on calcite dissolution in electrolyte solutions at the salt concentration lower than 0.1 M at room temperature. Calcite dissolution rate depends on ion diffusion (i.e., mass transport–controlled) below pH 8. Applied electric potental is able to alter the ion transportation, while the extent of dissolution rate enhancement is controlled by solution ionic strength. Calcite dissolution rates with varying solvent pH shows that calcite dissolution rates are simply influenced at low pH, and remain constant at high pH. In addition, the silicate dissolution rates under the same applied potential as calcite were assessed, it's dissolution kinetic does not altered by potential since its' rates is controlled by surface reaction at room temperature. For calcite, we also ascertain that the potential effect is significant in low ionic strength electrolyte compared to high ionic strength due to the ion crowding effect in the EDL, which caused lower diffusivity and higher viscosity. Moreover, the activation energy of the calcite dissolution decreases with the voltages of the electrical field, indicating that stimulating the suspension using potential actually eases the dissolution process. These findings are generally applicable to enhance mineral dissolution if their dissolution process is known as diffusion-controlled such as for most of the carbonates. This has implications on developing new method for accelerating mineral dissolution rates in applications such as electrokinetic remediation or mineral based fuel cell.

Chapter 6 Summary and Future Work

6.1. Summary and Conclusions

The primary objective of this dissertation is to clarify the effect of irradiation (i.e., in the form of Ar^+ ion implantation), and electric potential to mineral's chemical reactivity (i.e., dissolution rates were measured by using VSI and ICP-OES in this study). The irradiation-induced alterations in atomic structure and chemical reactivity are investigated for silicates and carbonates, which are typically found in aggregates used in nuclear power plant (NPP) concrete. In this work, we have shown that the radiation damage on the atomic structures of silicates such as quartz or albite (i.e., highly polymerized silicates) are more severe than in carbonates, i.e., calcite and dolomite. This can be explained by the fact that the atomic structures and connectivity of the carbonate phases remains broadly unaffected by irradiation. This behavior arises from their non-directional ionic bonds, which can recover to their initial geometry after each ballistic cascade. Further, we have demonstrated that mineral dissolution rates are strongly correlated with the alteration in atomic structure and the rigidity of the structural network as defined by the change in the number of constraints per atom, Δn_c (see Table 6-1).

Smaller enhancements in dissolution rates are observed for the other silicates: anorthite, and almandine. This can be explained by the presence of cations including Na, Al, Ca, and Fe, and results in a relative decreased percentage of covalent bonds and increase in ionic bonding. The unique behavior of almandine can be explained by its crystallographic structure as well. Indeed, unlike albite, anorthite, and quartz wherein the silicate tetrahedral groups are arranged in a three-dimensional framework structure, almandine comprises silicate groups that are isolated from each other. Our experimental data suggest that the degree of connectivity of the structure, i.e., degree of polymerization, affects the mineral's susceptibility for structural alterations.

Specifically, a higher extent of polymerization results in a higher degree of radiation damage due to the higher packing density, which favors radiation-induced structural changes.

The outcomes of the study have important implications on the selection of aggregates in concretes for nuclear power plant applications, and thus reveal that silicate minerals are expected to dissolve incrementally faster after irradiation. However, irradiation induces a substantially lower degree of alteration in both the structure and reactivity of carbonates as compared to common silicate minerals—particularly those silicates that feature a framework structure (i.e., that are fully polymerized). Although the reaction products (i.e., ASR gels) generated from both alkali-silica reaction (ASR) for siliceous aggregates or alkali-carbonate reaction (ACR) for carbonate aggregates are expansive, the comparisons of their expanding rates are still unclear. Commonly, the dissolution rates of silicates are around 2-to-3 orders lower than those of carbonates. Hence, in the absence of any irradiation exposure, selecting silicate aggregates may be more appropriate. In contrast, in the case of prolonged neutron radiation exposure, selecting carbonate-rich aggregates (i.e., limestone) over silicate aggregates (e.g., quartz or albite) may be beneficial in minimizing its degradation. Importantly, this consideration will also need to be compared to the respective volume expansions that can also induce cracking and affect the concrete's structural integrity.

Table 6-1: Summary of all the work done for irradiated mineral aggregate dissolution.

		Crystallographic structure	**Chemical composition**	**Δn_c [T2]**	**D_r [T3]**
Carbonate	**Calcite**	Trigonal (R3c)	$CaCO_3$	0	Nearly unchanged
	Dolomite	Trigonal (R3)	$CaMg(CO_3)_2$	0	Nearly unchanged
Silicate	**Quartz**	Trigonal (P321)	SiO_2	-0.617	Increased 10^3 times
	Albite	Triclinic (C1)	$NaAlSi_3O_8$	-0.307	Increased 15-20 times
	Anorthite	Triclinic (P1)	$CaAl_2Si_2O_8$	0.113	Slightly increased 1.3-1.5 times
	Almandine	Cubic (Ia3d)	$Fe_3Al_2Si_3O_{12}$	-0.650	Increased 1.5-2 times

In Chapter 5, this study demonstrates that electric potential has significant effect on calcite dissolution in electrolyte solutions at the salt concentration lower than 0.1 M at room temperature. Calcite dissolution rate depends on ion diffusion (i.e., mass transport–controlled) below pH 8. Applied electric potential is able to alter the ion transportation, while the extent of dissolution rate enhancement is controlled by solution ionic strength. Calcite dissolution rates with varying solvent pH shows that calcite dissolution rates are simply influenced at low pH, and remain constant at high pH. In addition, the silicate dissolution rates under the same applied potential as calcite were assessed, it's dissolution kinetic does not altered by potential since its' rates is controlled by surface reaction at room temperature. For calcite, we also ascertain that the potential effect is significant in low ionic strength electrolyte compared to high ionic strength due to the ion crowding effect in the EDL, which caused lower diffusivity and higher viscosity. Moreover, the activation energy of the calcite dissolution decreases with the voltages of the electrical field, indicating that stimulating the suspension using potential actually eases the dissolution process. These findings are generally applicable to enhance mineral dissolution if their dissolution process is known as diffusion-controlled such as for most of the carbonates. This has implications on developing new method for accelerating mineral dissolution rates in applications such as electrokinetic remediation or mineral based fuel cell.

6.2. Future works

By applying the topological constraint theory (TCT), the mineral dissolution rate can be estimated by using a mineral kinetic model, which is similar to the format of Arrhenius relation, that is proposed by Pignatelli *et al.* (see equation below):

$$D_R = D_{R0} \exp\left(-\frac{n_c E_0}{RT}\right) \qquad \text{Eq. (6-1)}$$

, where n_c, R and T are the number of constraints, the gas constant and the temperature in Kelvin, respectively, D_{R0} stands for the pre-exponential factor, which is simply related to solution chemistry, and E_0 is the energy required to break one number of constraints. This equation can be considered and discussed from two different perspectives. The dissolution constant, D_{R0} depends only on solution phase chemistry, whereas the second part of the equation, $\exp\left(-\frac{n_c E_0}{RT}\right)$, is determined by the solid material properties (i.e., atomic network, hardness…etc.). In order to further validate this model, additional experiments with broader ranges of materials and solution compositions are required, since parts of the correlation between the equation parameters and environmental conditions are still unidentified. The energy needed to break one constraint (n_c) was determined as $E_0 = 25.5 kJ/mol$ for silicate minerals at this point, however, this value my alter from materials to materials. Further measurements on a variety of minerals would probably provide detailed evidence to evaluate and modify this model.

The future study can address the following questions in order to generate a more comprehensive dissolution kinetics model that can cover most of the dissolution cases: (1) How will the E_0 change from minerals? What material properties affect the most? To determine the value of E_0, material properties have to be quantified, and is the proposed number of constraint (n_c) enough to cover most of the materials? Also, there is even less information about how D_{R0} evolves as the function of solution chemistry. Hence, developing a mineral dissolution kinetic model which can explain the effects of both the material and the liquid solution is necessary and challenging. The proposed future work can be divided into several parts, and the this kinetic model can be improved by further discussion: (1) The effect of structure and composition, (2) the

effect of disordered (i.e., non-crystalline) structure, (3) the effect of heterogeneous dissolution, and (4) the effect of Solution chemistry on dissolution reactivity.

Appendices

- **Appendix A (Surface topography change assessing by vertical scanning interferometry)**

The dissolution rates of pristine (non-implanted) and irradiated (implanted) albite surfaces were measured using vertical scanning interferometry (VSI), from which quantifications of sub-nanometer alterations of surface height can be obtained. Surface topography parameters (i.e., surface roughness (S_a), surface average height (Δh)) were determined for the unreacted and reacted areas on the surface. The dissolution rates were obtained by dividing the difference in average heights between the reference area (unreacted) and sample area (reacted) by the reaction time (Δt). The analysis of the VSI data was carried out using Gwyddion (version 2.47).

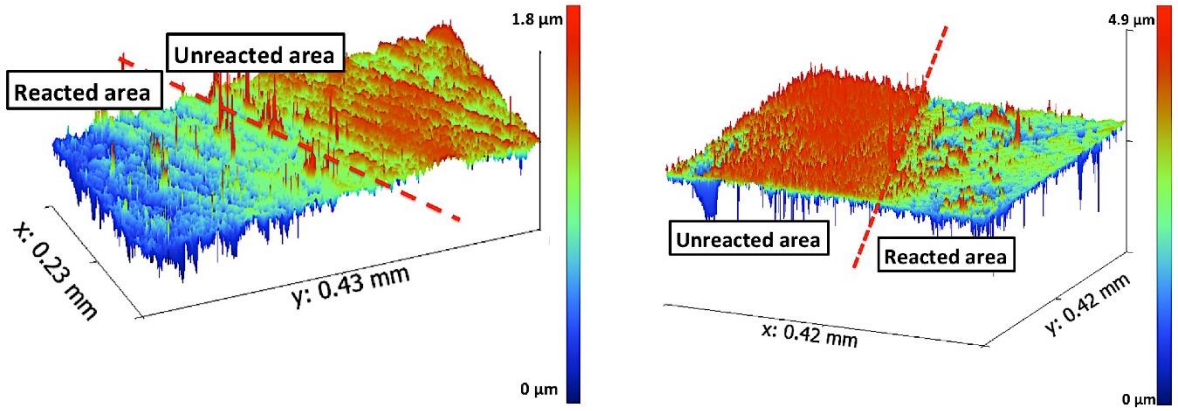

(a) **(b)**

Figure A: Representative VSI images of: **(a)** pristine albite, and, **(b)** irradiated albite, showing distinct average height differences between the unreacted and reacted areas of the surface after 10 days and 8 days of dissolution, respectively. The boundary between these two areas is given by the dashed red line. The surface roughness (S_a) of pristine and irradiated albite is similar as observed by VSI.

A section on the albite surface was covered by an inert silicone mask (Silicone Solutions SS-38) to preserve an unreacted part of the surface, which serves as a reference location to assess the average height change. The mask was peeled off after every measurement and then reapplied at the same position before resuming reaction of the sample with the solution. The mask was found to adhere well to the surface, and the solution did not penetrate under the silicone mask as would be apparent from peeling/swelling of the mask, which was not observed. As shown in Figure A, the boundary between the reacted and unreacted areas remained sharp after extended times (up to 10 days) of exposure to the solution.

- **Appendix B (The dissolution rates of irradiated and pristine albite across a range of pH and temperature)**

Dissolution rates were measured for 2 temperatures (25°C and 45°C) and 3 solution pH levels (pH 10, pH 12 and pH 13). Specifically, 0.1 mM NaOH (pH 10), 10 mM NaOH (pH 12) and 100 mM NaOH (pH 13) were selected to simulate the alkaline conditions offered by the pore solution in concrete. In general, the dissolution rates of irradiated albite are about 20 times higher compared to pristine albite, over the entire range of temperature and pH studied herein, as shown in Figure B and Table B below.

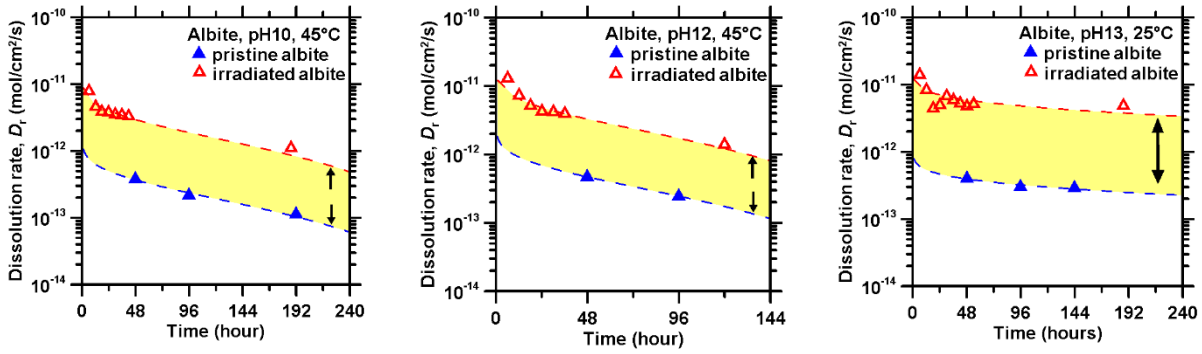

Figure B: The dissolution rates of pristine (solid blue triangles) and irradiated (open red triangles) albite at: **(a)** pH 10, 45°C, **(b)** pH 12, 45°C, and, **(c)** pH 13, 25°C, showing a general enhancement in dissolution rates after radiation, by a factor of about 20.

Table B: The dissolution enhancement ratios (DERs) of irradiated albite as compared to pristine albite upon dissolution in NaOH solutions of different pHs at 25 and 45 °C.

$DER = D_r^{irr} / D_r^{prist}$	**pH 10**	**pH 12**	**pH 13**	**Average**
25°C	22.45 ± 17.62	19.77 ± 5.60	14.49 ± 2.73	16.77 ± 3.52
45°C	14.15 ± 7.99	13.98 ± 8.37	15.79 ± 9.87	

- **Appendix C (Selected environmental conditions for the electric potential induced dissolution experiments)**

Table C: Selected environmental conditions for the experiments to demonstrate the effect of external potential to mineral dissolution rate. (A group is for examining the effect of ionic strength to dissolution rates without external electric potential, B group is designed for potential induced dissolution rates measurement, C set is designed for varying solvent pH, D corresponds to evolving temperatures, and E is related to orthoclase dissolution measurements.)

Sample Number	**Ionic strength (M)**	**Solvent pH**	**Temperature (°C)**	**External electric potential (V)**
Calcite-A-1	0.001	8.0	20	0
Calcite-A-2	0.010	8.0	20	0
Calcite-A-3	0.100	8.0	20	0
Calcite-A-4	1.000	8.0	20	0
Calcite-B-1	0.010	8.0	20	0
Calcite-B-2	0.010	8.0	20	0.001
Calcite-B-3	0.010	8.0	20	0.010

Calcite-B-4	0.010	8.0	20	0.100
Calcite-B-5	0.010	8.0	20	0.200
Calcite-B-6	0.010	8.0	20	0.300
Calcite-B-7	0.010	8.0	20	0.400
Calcite-B-8	0.100	8.0	20	0
Calcite-B-9	0.100	8.0	20	0.001
Calcite-B-10	0.100	8.0	20	0.010
Calcite-B-11	0.100	8.0	20	0.100
Calcite-B-12	0.100	8.0	20	0.200
Calcite-B-13	0.100	8.0	20	0.300
Calcite-B-14	0.100	8.0	20	0.400
Calcite-B-15	1.000	8.0	20	0
Calcite-B-16	1.000	8.0	20	0.001
Calcite-B-17	1.000	8.0	20	0.010
Calcite-B-18	1.000	8.0	20	0.100
Calcite-B-19	1.000	8.0	20	0.200
Calcite-B-20	1.000	8.0	20	0.300
Calcite-B-21	1.000	8.0	20	0.400
Calcite-C-1	0.010	4.0	20	0
Calcite-C-2	0.010	4.0	20	0.100
Calcite-C-3	0.010	4.0	20	0.200
Calcite-C-4	0.010	4.0	20	0.300
Calcite-C-5	0.010	4.0	20	0.400
Calcite-C-6	0.010	10.0	20	0
Calcite-C-7	0.010	10.0	20	0.100
Calcite-C-8	0.010	10.0	20	0.200
Calcite-C-9	0.010	10.0	20	0.300
Calcite-C-10	0.010	10.0	20	0.400
Calcite-D-1	0.010	8.0	40	0
Calcite-D-2	0.010	8.0	40	0.100
Calcite-D-3	0.010	8.0	40	0.200
Calcite-D-4	0.010	8.0	40	0.300
Calcite-D-5	0.010	8.0	40	0.400
Calcite-D-6	0.010	8.0	60	0
Calcite-D-7	0.010	8.0	60	0.100
Calcite-D-8	0.010	8.0	60	0.200
Calcite-D-9	0.010	8.0	60	0.300
Calcite-D-10	0.010	8.0	60	0.400
Orthoclase-E-1	0.010	5.5	20	0
Orthoclase -E-2	0.010	5.5	20	0.200
Orthoclase -E-3	0.010	5.5	20	0.400

Bibliography

[1] Neville AM. *Properties of concrete*. John Wiley & Sons, 1996.

[2] Mehta PK. Concrete. Structure, Properties and Materials(1986, accessed 21 May 2019).

[3] Naus DJ. *Primer on Durability of Nuclear Power Plant Reinforced Concrete Structures - A Review of Pertinent Factors*. ORNL/TM--2006/529, Oak Ridge National Laboratory (United States). Funding organisation: ORNL work for others (United States). Epub ahead of print 2007.

[4] Graves, H., Le Pape, Y., Naus, D., Rashid, J., Saouma, A., Sheikh, A. & Wall., J. In expanded material degradation assessment (EMDA), Vol. 4: Aging of concrete. Technical Report NUREG/CR-7153, ORNL/TM-2011/545. U.S. Nuclear Regulatory Commission (2013).

[5] Hilsdorf HK, Kropp JP, Koch HJ. The effects of nuclear radiation on the mechanical properties of concrete. 1978.

[6] Ichikawa T, Koizumi H. Possibility of radiation-induced degradation of concrete by alkali-silica reaction of aggregates. *Journal of Nuclear Science and Technology* 2002; 39: 880–884.

[7] Ichikawa T, Kimura T. Effect of nuclear radiation on alkali-silica reaction of concrete. *Journal of Nuclear Science and Technology* 2007; 44: 1281–1284.

[8] Field KG, Remec I, Pape YL. Radiation effects in concrete for nuclear power plants – Part I: Quantification of radiation exposure and radiation effects. *Nuclear Engineering and Design* 2015; 282: 126–143.

[9] Le Pape Y, Field KG, Remec I. Radiation effects in concrete for nuclear power plants, Part II: Perspective from micromechanical modeling. *Nuclear Engineering and Design* 2015; 282: 144–157.

[10] Streckeisen A. Classification and nomenclature of plutonic rocks recommendations of the IUGS subcommission on the systematics of Igneous Rocks. *Geol Rundsch* 1974; 63: 773–786.

[11] Pignatelli I, Kumar A, Field KG, et al. Direct experimental evidence for differing reactivity alterations of minerals following irradiation: The case of calcite and quartz. *Sci Rep*; 6. 2016.

[12] Douillard L, Duraud JP. Swift heavy ion amorphization of quartz — a comparative study of the particle amorphization mechanism of quartz. *Nuclear Instruments and Methods in Physics Research Section B: Beam Interactions with Materials and Atoms* 1996; 107: 212–217.

[13] Douillard L, Duraud JP. Amorphization of α-quartz under irradiation. *J Phys III France* 1996; 6: 1677–1687.

[14] Kinchin GH, Pease RS. The displacement of atoms in solids by radiation. *Rep Prog Phys* 1955; 18: 1–51.

[15] Okamoto PR, Lam NQ, Rehn LE. Physics of crystal-to-glass transformations. In: Ehrenreich H, Spaepen F (eds) *Solid State Physics*. Academic Press, pp. 1–135.

[16] Ewing RC. The metamict state: 1993 — the centennial. *Nuclear Instruments and Methods in Physics Research Section B: Beam Interactions with Materials and Atoms* 1994; 91: 22–29.

[17] Ewing RC, Chakoumakos BC, Lumpkin GR, et al. Metamict minerals: Natural analogues for radiation damage effects in ceramic nuclear waste forms. *Nuclear Instruments and Methods in Physics Research B* 1988; 32: 487–497.

[18] Elleuch LF, Dubois F, Rappeneau J. Effects of neutron radiation on special concretes and their components. *SP* 1972; 34: 1071–1108.

[19] Dubrovskii VB, Ibragimov ShSh, Kulakovskii MYa, et al. Radiation damage in ordinary concrete. *At Energy* 1967; 23: 1053–1058.

[20] Primak W. Fast-neutron-induced changes in quartz and vitreous silica. *Phys Rev* 1958; 110: 1240–1254.

[21] Raju KS. Radiation effects in calcite. *Pramana - J Phys* 1977; 8: 266–275.

[22] Venkateshwar Rao E, Ramakrishna Murthy M. Ion beam modifications of defect sub-structure of calcite cleavages. *Bull Mater Sci* 2008; 31: 139–142.

[23] Luthra JM. X-ray studies on pile-irradiated calcite.. *Indian J Pure Appl Phys; 1969,* 7: 444

[24] Wittels MC. Structural behaviou of neutron irradiated quartz. *The Philosophical Magazine: A Journal of Theoretical Experimental and Applied Physics* 1957; 2: 1445–1461.

[25] Zubov VG, Ivanov AT. Expansion of quartz caused by irradiation with fast neutrons. *Soviet Phys-Cryst (Engl Transl), 11: 372-4(Nov-Dec 1966)*,

[26] ASTM International, Annual book of ASTM Standards; 2012.

[27] Glasser FP. Chemistry of the alkali-aggregate reaction. *The Alkali-Silica Reaction in Concrete*. September 1991.

[28] Powers TC, Steinour HH. An interpretation of some published researches on the alkali-aggregate reaction Part 1-The chemical reactions and mechanism of expansion. *JP* 1955;

51: 497–516.

[29] Brady PV, Walther JV. Controls on silicate dissolution rates in neutral and basic pH solutions at 25°C. *Geochimica et Cosmochimica Acta* 1989; 53: 2823–2830.

[30] Knauss KG, Wolery TJ. Dependence of albite dissolution kinetics on ph and time at 25°c and 70°c. *Geochimica et Cosmochimica Acta* 1986; 50: 2481–2497.

[31] Molchanov VS, Prikhidko NE. Corrosion of silicate glasses by alkaline solutions. *Russ Chem Bull* 1957; 6: 1179–1184.

[32] Gaboriaud F, Chaumont D, Nonat A, et al. Study of the influence of alkaline ions (Li, Na and K) on the structure of the silicate entities in silico alkaline sol and on the formation of the silico-calco-alkaline gel. *Journal of Sol-Gel Science and Technology* 1998; 13: 353–358.

[33] Brantley SL (ed). *Kinetics of water-rock interaction*. New York, NY: Springer, 2008.

[34] Rajabipour F, Giannini E, Dunant C, et al. Alkali–silica reaction: Current understanding of the reaction mechanisms and the knowledge gaps. *Cement and Concrete Research* 2015; 76: 130–146.

[35] Katayama T. The so-called alkali-carbonate reaction (ACR) — Its mineralogical and geochemical details, with special reference to ASR. *Cement and Concrete Research* 2010; 40: 643–675.

[36] Swenson, E. G., A Reactive Aggregate Undetected by ASTM Tests, Bulletin No. 226, American Society for Testing and Materials, pp. 48-5 1, (1957).

[37] Gillott JE. Mechanism and kinetics of expansion in the alkali-carbonate rock reaction. *Can J Earth Sci* 1964; 1: 121–145.

[38] Hadley DW. Alkali reactivity of dolomitic carbonate rocks. *Highway Research Record*, , 1964.

[39] Swenson EG, Gillott JE. Alkali-carbonate rock reaction. *Highway Research Record*, 1964.

[40] Tong L, Tang M. Expandability of solid-volume-reducing reactions of alkali-magnesite and alkali-dolomite. *Cement Concrete and Aggregates* 1997; 19: 31–37.

[41] Tong L, Tang M. Correlation between reaction and expansion of alkali-carbonate reaction. *Cement and Concrete Research* 1995; 25: 470–476.

[42] Lasaga AC. *Kinetic Theory in the Earth Sciences*. Princeton University Press, 2014.

[43] Burton W. K., Cabrera N., Frank F. C., et al. The growth of crystals and the equilibrium structure of their surfaces. *Philosophical Transactions of the Royal Society of London*

Series A, Mathematical and Physical Sciences 1951; 243: 299–358.

[44] Lasaga AC, Lüttge A. A model for crystal dissolution. *European Journal of Mineralogy* 2003; 15: 603–615.

[45] Aharoni C, Levinson S, Ravina I, et al. Kinetics of soil chemical reactions: Relationships between empirical equations and diffusion models. *Soil Science Society of America Journal* 1991; 55: 1307–1312.

[46] Stillings LL, Brantley SL, Machesky ML. Proton adsorption at an adularia feldspar surface. *Geochimica et Cosmochimica Acta* 1995; 59: 1473–1482.

[47] Walther JV, Brantley SL, Stillings LL. Feldspar dissolution at 25 degrees C and low pH; discussion and reply. *American Journal of Science* 1997; 297: 1012–1032.

[48] Fry RA, Tsomaia N, Pantano CG, et al. 19F MAS NMR Quantification of accessible hydroxyl sites on fiberglass surfaces. *Journal of the American Chemical Society* 2003; 125: 2378–2379.

[49] Wieland E, Wehrli B, Stumm W. The coordination chemistry of weathering: III. A generalization on the dissolution rates of minerals. *Geochimica et Cosmochimica Acta* 1988; 52: 1969–1981.

[50] Amrhein C, Suarez DL. The use of a surface complexation model to describe the kinetics of ligand-promoted dissolution of anorthite. *Geochimica et Cosmochimica Acta* 1988; 52: 2785–2793.

[51] Plummer LN, Wigley TML, Parkhurst DL. The kinetics of calcite dissolution in CO 2 - water systems at 5 degrees to 60 degrees C and 0.0 to 1.0 atm CO 2. *American Journal of Science* 1978; 278: 179–216.

[52] Plimpton S. Fast parallel algorithms for short-range molecular dynamics. *Journal of Computational Physics* 1995; 117: 1–19.

[53] Wang B, Yu Y, Pignatelli I, et al. Nature of radiation-induced defects in quartz. *The Journal of Chemical Physics* 2015; 143: 024505.

[54] Berendsen HJC, Postma JPM, van Gunsteren WF, et al. Molecular dynamics with coupling to an external bath. *The Journal of Chemical Physics* 1984; 81: 3684–3690.

[55] Mir AH, Toulemonde M, Jegou C, et al. Understanding and simulating the material behavior during multi-particle irradiations. *Scientific Reports* 2016; 6: 30191.

[56] Manzano H, Moeini S, Marinelli F, et al. Confined water dissociation in microporous defective silicates: Mechanism, dipole distribution, and impact on substrate properties. *Journal of the American Chemical Society* 2012; 134: 2208–2215.

[57] Du J, Cormack AN. The medium range structure of sodium silicate glasses: a molecular

dynamics simulation. *Journal of Non-Crystalline Solids* 2004; 349: 66–79.

[58] Raiteri P, Demichelis R, Gale JD. Thermodynamically consistent force field for molecular dynamics simulations of alkaline-earth carbonates and their aqueous speciation. *The Journal of Physical Chemistry C* 2015; 119: 24447–24458.

[59] Phillips JC, Thorpe MF. Constraint theory, vector percolation and glass formation. *Solid State Communications* 1985; 53: 699–702.

[60] Maxwell JC. L. On the calculation of the equilibrium and stiffness of frames. *The London, Edinburgh, and Dublin Philosophical Magazine and Journal of Science* 1864; 27: 294–299.

[61] Ichikawa T, Miura M. Modified model of alkali-silica reaction. *Cement and Concrete Research* 2007; 37: 1291–1297.

[62] Varshneya AK. *Fundamentals of Inorganic Glasses*. Elsevier, 2013.

[63] Seabrook ASR-monitoring and building deformation aging management programs adult report, United States Nuclear Regulatory Commission (NRC) report, Washington, D.C. 20555-0001, Dec. 21, 2006.

[64] Concrete degradation by alkali-silica reaction, United States Nuclear Regulatory Commission (NRC) report, Washington, D.C. 20555-0001, Nov. 18, 2016.

[65] Haha MB, Gallucci E, Guidoum A, et al. Relation of expansion due to alkali silica reaction to the degree of reaction measured by SEM image analysis. *Cement and Concrete Research* 2007; 37: 1206–1214.

[66] Momma K, Izumi F. VESTA 3 for three-dimensional visualization of crystal, volumetric and morphology data. *Journal of Applied Crystallography* 2011; 44: 1272–1276.

[67] Aggregates approved material list, Rev. 03-30-17, State of Louisiana Department of Transportation and Development, 2017.

[68] Langer WH, Knepper DH, Geologic characterization of natural aggregate. *US Department of the Interior U.S. Geological Survey;* US Department of the Interior, 1995.
[69] Kosmatka SH, Kerkhoff B, Panarese WC. *Design and Control of Concrete Mixtures.* Portland Cement Association, 2003; Chapter 5.

[70] Luettge A. An interferometric study of the dissolution kinetics of anorthite; The role of reactive surface area. *American Journal of Science* 1999; 299: 652–678.

[71] Kumar A, Reed J, Sant G. Vertical scanning interferometry: A new method to measure the dissolution dynamics of cementitious minerals. *Journal of the American Ceramic Society* 2013; 96: 2766–2778.

[72] Hamilton JP, Pantano CG, Brantley SL. Dissolution of albite glass and crystal.

Geochimica et Cosmochimica Acta 2000; 64: 2603–2615.

[73] https://www.wardsci.com/store/.

[74] https://mibl.engin.umich.edu/.

[75] Stoller RE, Toloczko MB, Was GS, et al. On the use of SRIM for computing radiation damage exposure. *Nuclear Instruments and Methods in Physics Research Section B: Beam Interactions with Materials and Atoms* 2013; 310: 75–80.

[76] Snead LL, Zinkle SJ, Hay JC, et al. Amorphization of SiC under ion and neutron irradiation. *Nuclear Instruments and Methods in Physics Research Section B: Beam Interactions with Materials and Atoms* 1998; 141: 123–132.

[77] Ribbe PH, Megaw HD, Taylor WH, et al. The albite structures. *Acta Cryst B* 1969; 25: 1503–1518.

[78] The international centre for diffraction data (ICDD).

[79] Salje EKH. Phase transitions and vibrational spectroscopy in feldspars. *In Feldspars and their Reactions*. Parsons, I., Ed.; Kluwer Academic Publishers: Dordrecht: Springer Netherlands, *1993,* pp. 103–160.

[80] Atkinson AJ, Carpenter MJ, Salje EKH. Hard mode infrared spectroscopy of plagioclase feldspars. *European Journal of Mineralogy* 1999; 11: 7–21.

[81] Makreski P, Jovanovski G, Kaitner B. Minerals from Macedonia. XXIV. Spectra-structure characterization of tectosilicates. *Journal of Molecular Structure* 2009; 924–926: 413–419.

[82] Vollpracht A, Lothenbach B, Snellings R, et al. The pore solution of blended cements: a review. *Materials Structures* 2016; 49: 3341–3367.

[83] http://siliconesolutions.com/.

[84] Chou L, Wollast R. Steady-state kinetics and dissolution mechanisms of albite. *American Journal of Science* 1985; 285: 963–993.

[85] Yamamoto-Kawai M, McLaughlin FA, Carmack EC, et al. Aragonite undersaturation in the arctic ccean: Effects of ccean acidification and sea ice melt. *Science* 2009; 326: 1098–1100.

[86] Nečas D, Klapetek P. Gwyddion: an open-source software for SPM data analysis. *Open Physics* 2011; 10: 181–188.

[87] Parkhurst DL, Appelo CAJ. *Description of input and examples for PHREEQC version 3: a computer program for speciation, batch-reaction, one-dimensional transport, and inverse geochemical calculations*. USGS Numbered Series 6-A43, Reston, VA: U.S.

Geological Survey.

[88] Lüttge A. Crystal dissolution kinetics and Gibbs free energy. *Journal of Electron Spectroscopy and Related Phenomena* 2006; 150: 248–259.

[89] Beig MS, Lüttge A. Albite dissolution kinetics as a function of distance from equilibrium: Implications for natural feldspar weathering. *Geochimica et Cosmochimica Acta* 2006; 70: 1402–1420.

[90] Oelkers EH, Schott J, Devidal J-L. The effect of aluminum, pH, and chemical affinity on the rates of aluminosilicate dissolution reactions. *Geochimica et Cosmochimica Acta* 1994; 58: 2011–2024.

[91] Hellmann R, Tisserand D. Dissolution kinetics as a function of the Gibbs free energy of reaction: An experimental study based on albite feldspar. *Geochimica et Cosmochimica Acta* 2006; 70: 364–383.

[92] Blum A, Lasaga A. Role of surface speciation in the low-temperature dissolution of minerals. *Nature* 1988; 331: 431.

[93] Yang Y, Min Y, Lococo J, et al. Effects of Al/Si ordering on feldspar dissolution: Part I. Crystallographic control on the stoichiometry of dissolution reaction. *Geochimica et Cosmochimica Acta* 2014; 126: 574–594.

[94] MacDonald SA, Schardt CR, Masiello DJ, et al. Dispersion analysis of FTIR reflection measurements in silicate glasses. *Journal of Non-Crystalline Solids* 2000; 275: 72–82.

[95] Burns A, Brack HP, Risen WM. Dielectric and infrared reflectance studies of inorganic oxide glasses. *Journal of Non-Crystalline Solids* 1991; 131–133: 994–1000.

[96] Matson DW, Sharma SK, Philpotts JA. The structure of high-silica alkali-silicate glasses. A Raman spectroscopic investigation. *Journal of Non-Crystalline Solids* 1983; 58: 323–352.

[97] Husung RD, Doremus RH. The infrared transmission spectra of four silicate glasses before and after exposure to water. *Journal of Materials Research* 1990; 5: 2209–2217.

[98] Bykov VN, Denisov AV, Dubrovskii VB, et al. Effect of irradiation temperature on the radiation expansion of quartz. *Soviet Atomic Energy* 1981; 51: 593–595.

[99] Bauchy M. Structural, vibrational, and elastic properties of a calcium aluminosilicate glass from molecular dynamics simulations: The role of the potential. *The Journal of Chemical Physics* 2014; 141: 024507.

[100] Bauchy M, Qomi MJA, Ulm F-J, et al. Order and disorder in calcium–silicate–hydrate. *The Journal of Chemical Physics* 2014; 140: 214503.

[101] Bauchy M, Guillot B, Micoulaut M, et al. Viscosity and viscosity anomalies of model

silicates and magmas: A numerical investigation. *Chemical Geology* 2013; 346: 47–56.

[102] Wang B, Krishnan NMA, Yu Y, et al. Irradiation-induced topological transition in SiO2: Structural signature of networks' rigidity. *Journal of Non-Crystalline Solids* 2017; 463: 25–30.

[103] Phillips JC. Topology of covalent non-crystalline solids I: Short-range order in chalcogenide alloys. *Journal of Non-Crystalline Solids* 1979; 34: 153–181.

[104] Bauchy M. Topological Constraints and Rigidity of Network Glasses from Molecular Dynamics Simulations. *arXiv:150606483 [cond-mat]*.

[105] Thorpe MF. Continuous deformations in random networks. *Journal of Non-Crystalline Solids* 1983; 57: 355–370.

[106] Wang F, Mamedov S, Boolchand P, et al. Pressure Raman effects and internal stress in network glasses. *Physical Review B* 2005; 71: 174201.

[107] Chubynsky MV, Brière M-A, Mousseau N. Self-organization with equilibration: A model for the intermediate phase in rigidity percolation. *Physical Review E* 2006; 74: 016116.

[108] Pignatelli I, Kumar A, Bauchy M, et al. Topological control on silicates' dissolution kinetics. *Langmuir* 2016; 32: 4434–4439.

[109] Bauchy M, Qomi MJA, Bichara C, et al. Rigidity transition in materials: Hardness is driven by weak atomic constraints. *Physical Review Letters* 2015; 114: 125502.

[110] Mascaraque N, Bauchy M, Smedskjaer MM. Correlating the network topology of oxide glasses with their chemical durability. *The Journal of Physical Chemistry B* 2017; 121: 1139–1147.

[111] Oey T, Timmons J, Stutzman P, et al. An improved basis for characterizing the suitability of fly ash as a cement replacement agent. *Journal of the American Ceramic Society* 2017; 100: 4785–4800.

[112] Ghent ED, Stout MZ. Geobarometry and geothermometry of plagioclase-biotite-garnet-muscovite assemblages. *Contributions to Mineralogy and Petrology* 1981; 76: 92–97.

[113] Cressey G. Exsolution in almandine-pyrope-grossular garnet. *Nature* 1978; 271: 533.

[114] Keesmann I, Matthes S, Schreyer W, et al. Stability of almandine in the system FeO-(Fe2O3)-Al2O3-SiO2-(H2O) at elevated pressures. *Contributions to Mineralogy and Petrology* 1971; 31: 132–144.

[115] Banerjee G. Beach and minerals: A new material resource for glass and ceramics. *Bulletin of Materials Science* 1998; 21: 349–354.

[116] Conley WR, Hsiung K. Design and application of multimedia filters. *Journal (American*

Water Works Association) 1969; 61: 97–101.

[117] Barcova K, Mashlan M, Martinec P. Mössbauer study of the thermal behaviour of garnets used in high-energy water jet technologies. In: *Industrial Applications of the Mössbauer Effect*. Springer, Dordrecht, pp. 463–469.

[118] Kulekci MK. Processes and apparatus developments in industrial waterjet applications. *International Journal of Machine Tools and Manufacture* 2002; 42: 1297–1306.

[119] Olsen DW. Garnet, Industrial, U.S. Geological Survey Publications, 2002.

[120] Hsiao Y-H, La Plante EC, Krishnan NMA, et al. Effects of Irradiation on Albite's Chemical Durability. *The Journal of Physical Chemistry A* 2017; 121: 7835–7845.

[121] Crundwell FK. The mechanism of dissolution of forsterite, olivine and minerals of the orthosilicate group. *Hydrometallurgy* 2014; 150: 68–82.

[122] Casey WH. Westrich, H.R.; Control of dissolution rates of orthosilicate minerals by divalent metal-oxygen bonds, Nature 1992, 355, 6356.

[123] Westrich HR, Cygan RT, Casey WH, Zemitis C, Arnold GW. The dissolution kinetics of mixed-cation orthosilicate minerals, *American Journal of Science* 1993; 293: 869-893.

[124] Dove PM. The dissolution kinetics of quartz in aqueous mixed cation solutions. *Geochimica et Cosmochimica Acta* 1999; 63: 3715–3727.

[125] Armbruster T, Geiger CA, Lager GA. Single-crystal X-ray structure study of synthetic pyrope almandine garnets at 100 and 293 K. *American Mineralogist* 1992; 77: 512–521.

[126] http://www.leica-microsystems.com/home/.

[127] https://www.brookhaveninstruments.com/.

[128] Bio-Rad. http://weww.bio-Rad.com/.

[129] Velbel MA. Natural weathering mechanisms of almandine garnet. *Geology* 1984; 12: 631–634.

[130] Walther JV. Relation between rates of aluminosilicate mineral dissolution, pH, temperature, and surface charge. *American Journal of Science* 1996; 296: 693–728.

[131] Carroll-Webb SA, Walther JV. A surface complex reaction model for the pH-dependence of corundum and kaolinite dissolution rates. *Geochimica et Cosmochimica Acta* 1988; 52: 2609–2623.

[132] Wieland E, Stumm W. Dissolution kinetics of kaolinite in acidic aqueous solutions at 25°C. *Geochimica et Cosmochimica Acta* 1992; 56: 3339–3355.

[133] Casey WH, Westrich HR. Control of dissolution rates of orthosilicate minerals by divalent metal–oxygen bonds. *Nature* 1992; 355: 157.

[134] Yu Y, Wang M, Zhang D, et al. Stretched exponential relaxation of glasses at low temperature. *Physical Review Letters* 2015; 115: 165901.

[135] Vegard L. Die Konstitution der Mischkristalle und die Raumfüllung der Atome. *Z Physik* 1921; 5: 17–26.

[136] Lasaga AC. Chemical kinetics of water-rock interactions. *Journal of Geophysical Research: Solid Earth* 2012; 4009–4025.

[137] Stumm W, Morgan JJ. *Aquatic Chemistry: Chemical Equilibria and Rates in Natural Waters*. John Wiley & Sons, 2012.

[138] Parks GA. Aqueous surface chemistry of oxides and complex oxide minerals. In: *Equilibrium Concepts in Natural Water Systems*. American Chemical Society, pp. 121–160.

[139] Brady PV, Walther JV. Kinetics of quartz dissolution at low temperatures. *Chemical Geology* 1990; 82: 253–264.

[140] Dzombak DA, Morel F, Morel. *Surface Complexation Modeling: Hydrous Ferric Oxide*. John Wiley & Sons, 1990.

[141] Kristiansen K, Valtiner M, Greene GW, et al. Pressure solution – The importance of the electrochemical surface potentials. *Geochimica et Cosmochimica Acta* 2011; 75: 6882–6892.

[142] Greene GW, Kristiansen K, Meyer EE, et al. Role of electrochemical reactions in pressure solution. *Geochimica et Cosmochimica Acta* 2009; 73: 2862–2874.

[143] Valtiner M, Kristiansen K, Greene GW, et al. Effect of surface roughness and electrostatic surface potentials on forces between dissimilar surfaces in aqueous solution. *Advanced Materials* 2011; 23: 2294–2299.

[144] Hunter RJ. *Zeta Potential in Colloid Science: Principles and Applications*. Academic Press, 2013.

[145] Ohshima H, Makino K. *Colloid and Interface Science in Pharmaceutical Research and Development*. Elsevier, 2014.

[146] Debye, P., Hfickel, E. The interionic attraction theory of deviations from ideal behavior in solution, *Physikalische Zeitschrift* 1923; 24: 185.

[147] Bauchy M, Micoulaut M. Percolative heterogeneous topological constraints and fragility in glass-forming liquids. *Europhysics Letters* 2013; 104: 56002.

[148] Mascaraque N, Bauchy M, Fierro JLG, et al. Dissolution kinetics of hot compressed oxide glasses. *The Journal of Physical Chemistry B* 2017; 121: 9063–9072.

[149] Loewenstein W. The distribution of aluminum in the tetrahedra of silicates and aluminates. *American Mineralogist* 1954; 39: 92–96.

[150] Tossell JA. A theoretical study of the molecular basis of the Al avoidance rule and of the spectral characteristics of Al-O-Al linkages. *American Mineralogist* 1993; 78: 911–920.

[151] Morse JW, Mackenzie FT. *Geochemistry of Sedimentary Carbonates*. Elsevier, 1990.

[152] Naik Tarun R. Sustainability of Concrete Construction. *Practice Periodical on Structural Design and Construction* 2008; 13: 98–103.

[153] Solís-Carcaño R, Moreno EI. Evaluation of concrete made with crushed limestone aggregate based on ultrasonic pulse velocity. *Construction and Building Materials* 2008; 22: 1225–1231.

[154] Aquino C, Inoue M, Miura H, et al. The effects of limestone aggregate on concrete properties. *Construction and Building Materials* 2010; 24: 2363–2368.

[155] Poitevin P. Limestone aggregate concrete, usefulness and durability. *Cement and Concrete Composites* 1999; 21: 89–97.

[156] Maruyama I, Kontani O, Takizawa M, et al. Development of soundness assessment procedure for concrete members affected by neutron and gamma-ray irradiation. *Advanced Concrete Technology* 2017; 15: 440–523.

[157] Hsiao Y-H, La Plante EC, Krishnan NMA, et al. Role of Electrochemical Surface Potential and Irradiation on Garnet-type Almandine's Dissolution Kinetics. *The Journal of Physical Chemistry C* 2018.

[158] Naus DJ, Oland CB, Ellingwood BR, et al. Summary and conclusions of a program addressing aging of nuclear power plant concrete structures. *Nuclear Engineering and Design* 1999; 194: 73–96.

[159] Ichikawa T, Koizumi H. Possibility of radiation-induced degradation of concrete by alkali-silica reaction of aggregates. *Journal of Nuclear Science and Technology* 2002; 39: 880–884.

[160] Ichikawa T, Kimura T. Effect of nuclear radiation on alkali-silica reaction of concrete. *Journal of Nuclear Science and Technology* 2007; 44: 1281–1284.

[161] Handin J, Higgs DV, Lewis DR, et al. Effects of gamma radiation on the experimenal deformation of calcite and certain rocks. *Geological Society of America Bulletin* 1957; 68: 1203–1224.

[162] Nagabhushana H, Prashantha SC, Nagabhushana BM, et al. Damage creation in swift

heavy ion-irradiated calcite single crystals: Raman and Infrared study. *Spectrochimica Acta Part A: Molecular and Biomolecular Spectroscopy* 2008; 71: 1070–1073.

[163] Wencka M, Lijewski S, Hoffmann SK. Dynamics of CO 2 − radiation defects in natural calcite studied by ESR, electron spin echo and electron spin relaxation. *Journal of Physics: Condensed Matter* 2008; 20: 255237.

[164] Chou L, Garrels RM, Wollast R. Comparative study of the kinetics and mechanisms of dissolution of carbonate minerals. *Chemical Geology* 1989; 78: 269–282.

[165] Pokrovsky OS, Golubev SV, Schott J. Dissolution kinetics of calcite, dolomite and magnesite at 25 °C and 0 to 50 atm pCO2. *Chemical Geology* 2005; 217: 239–255.

[166] Tribble JS, Arvidson RS, Lane M, et al. Crystal chemistry, and thermodynamic and kinetic properties of calcite, dolomite, apatite, and biogenic silica: applications to petrologic problems. *Sedimentary Geology* 1995; 95: 11–37.

[167] Markgraf SA, Reeder RJ. High-temperature structure refinements of calciteand magnesite. *American Mineralogist* 1985; 70, 590-600.

[168] Krivokoneva G, Ikhonina Y, Solntseva L, et al. Effects of Mg-Ca substitution on radiation resistance of calcite structures Radiography of Mineral Resources. *Radiography of Mineral Resources* 1977; 2: 82–87.

[169] Swanson ML, Parsons JR, Hoelke CW. Damaged regions in neutron-irradiated and ion-bombarded Ge and Si. *Radiation Effects* 1971; 9: 249–256.

[170] Cuomo JJ, Rossnagel SM (International BMC, Kaufman HR (Front RR and CSC (US)). *Handbook of ion beam processing technology*.

[171] Krishnan NMA, Wang B, Yu Y, et al. Enthalpy Landscape Dictates the Irradiation-Induced Disordering of Quartz. *Physical Review X* 2017; 7: 031019.

[172] Averback RS, Benedek R, Merkle KL. Correlations between ion and neutron irradiations: Defect production and stage I recovery. *Journal of Nuclear Materials* 1978; 75: 162–166.

[173] Vandeginste V, John CM. Influence of climate and dolomite composition on dedolomitization: insights from a multi-proxy study in the central Oman Mountains. *Journal of Sedimentary Research* 2012; 82: 177–195.

[174] Wang J, Becker U. Structure and carbonate orientation of vaterite (CaCO3). *American Mineralogist* 2009; 94: 380–386.

[175] Buhmann D, Dreybrodt W. The kinetics of calcite dissolution and precipitation in geologically relevant situations of karst areas. *Chemical Geology* 1985; 48: 1-4.

[176] Compton RG, Brown CA. The inhibition of calcite dissolution/precipitation: Mg2+ cations. *Journal of Colloid and Interface Science* 1994; 165: 445–449.

[177] Ruiz-Agudo E, Kowacz M, Putnis CV, et al. The role of background electrolytes on the kinetics and mechanism of calcite dissolution. *Geochimica et Cosmochimica Acta* 2010; 74: 1256–1267.

[178] Ruiz-Agudo E, Putnis CV, Jiménez-López C, et al. An atomic force microscopy study of calcite dissolution in saline solutions: The role of magnesium ions. *Geochimica et Cosmochimica Acta* 2009; 73: 3201–3217.

[179] Shiraki R, Rock PA, Casey WH. Dissolution kinetics of calcite in 0.1 M NaCl solution at room temperature: An atomic force microscopic (AFM) study. *Aquatic Geochemistry* 2000; 6: 87–108.

[180] Dolgaleva IV, Gorichev IG, Izotov AD, et al. Modeling of the effect of pH on the calcite dissolution kinetics. *Theoretical Foundations of Chemical Engineering* 2005; 39: 614–621.

[181] Busenberg E. A comparable study of the dissolution and crystal growth kinetics of calcite and aragonite. *U S Geological Bull* 1986; 1578: 139–168.

[182] Pierre A, Lamarche JM, Mercier R, et al. Calcium as potential determining ion in aqueous calcite suspensions. *Journal of Dispersion Science and Technology* 1990; 11: 611–635.

[183] Sjöberg EL, Rickard DT. Calcite dissolution kinetics: Surface speciation and the origin of the variable pH dependence. *Chemical Geology* 1984; 42: 119–136.

[184] Arvidson RS, Ertan IE, Amonette JE, et al. Variation in calcite dissolution rates:: A fundamental problem? *Geochimica et Cosmochimica Acta* 2003; 67: 1623–1634.

[185] Busenberg E, Plummer N. The kinetics of dissolution of dolomite in CO2-H2O systems at 1.5 to 65oC and 0 to 1 atm PCO2. *American Journal of Science* 1982; 282: 45–78.

[186] Pokrovsky OS, Schott J. Kinetics and Mechanism of Dolomite Dissolution in Neutral to Alkaline Solutions Revisited. *American Journal of Science* 2001; 301: 597–626.

[187] Foreman AJE, Makin MJ. Dislocation movement through random arrays of obstacles. *The Philosophical Magazine: A Journal of Theoretical Experimental and Applied Physics* 1966; 14: 911–924.

[188] Raju KS. Radiation effects in calcite. *Pramana – Journal of Physics* 1977; 8: 266–275.

[189] Meike A. A micromechanical perspective on the role of dislocations in selective dissolution. *Geochimica et Cosmochimica Acta* 1990; 54: 3347–3352.

[190] Wong CF. Neutron radiation damege in some birefringent crystals. *Physics Letters A* 1974; 50: 346.

[191] Ali SM, Bonnier F, Lambkin H, et al. A comparison of Raman, FTIR and ATR-FTIR

micro spectroscopy for imaging human skin tissue sections. *Analytical Methods* 2013; 9..

[192] HuaNc CK, Konn PF, Liniaersity C, et al. Infrared study of the carbonate minerals. The American Mineralogist 1960; 45: 311-324.

[193] Lane MD, Christensen PR. Thermal infrared emission spectroscopy of anhydrous carbonates. *Journal of Geophysical Research: Planets* 1997; 102: 25581-25592..

[194] Edwards HGM, Villar SEJ, Jehlicka J, et al. FT–Raman spectroscopic study of calcium-rich and magnesium-rich carbonate minerals. *Spectrochimica Acta Part A: Molecular and Biomolecular Spectroscopy* 2005; 61: 2273–2280.

[195] Rutt HN, Nicola JH. Raman spectra of carbonates of calcite structure. *Journal of Physics C: Solid State Physics* 1974; 7: 4522.

[196] Bischoff WD, Sharma SK, Mackenzie FT. Carbonate ion disorder in synthetic and biogenic magnesian calcites: Raman structral study. American Mineralogist 1985; 70: 581-589.

[197] Krishnan NMA, Le Pape Y, Sant G, et al. Effect of irradiation on silicate aggregates' density and stiffness. *Journal of Nuclear Materials* 2018; 512: 126–136.

[198] Krishnan NMA, Ravinder R, Kumar R, et al. Density-stiffness scaling in minerals upon disordering: Irradiation vs. vitrification. *Acta Materialia* 2018.

[199] Denisov AV, Dubrovskii VB, Krivokoneva GK. Radiation changes in minerals of concrete aggregates and their analytical determination. *Issues of Nuclear Science and Technology* 1979; 18: 31.

[200] Kabacińska Z, Yate L, Wencka M, et al. Nanoscale effects of radiation (UV, X-ray, and γ) on calcite surfaces: Implications for its mechanical and physico-chemical properties. *The Journal of Physical Chemistry C* 2017; 121: 13357–13369.

[201] Smedskjaer MM, Bauchy M, Mauro JC, et al. Unique effects of thermal and pressure histories on glass hardness: Structural and topological origin. *The Journal of Physical Chemistry* 2015; 143: 164505.

[202] Youssef KM, Zaddach AJ, Niu C, et al. A novel low-density, high-hardness, high-entropy alloy with close-packed single-phase nanocrystalline structures. *Materials Research Letters* 2015; 3: 95–99.

[203] Trachenko K, Pruneda JM, Artacho E, et al. How the nature of the chemical bond governs resistance to amorphization by radiation damage. *Physical Review B* 2005; 71: 184104.

[204] Trachenko K. Understanding resistance to amorphization by radiation damage. *Journal of Physics: Condensed Matter* 2004; 16: R1491.

[205] Mascaraque N, Bauchy M, Smedskjaer MM. Correlating the network topology of oxide glasses with their chemical durability. *The Journal of Physical Chemistry B* 2017; 121: 1139–1147.

[206] Oey T, Frederiksen KF, Mascaraque N, et al. The role of the network-modifier's field-strength in the chemical durability of aluminoborate glasses. *Journal of Non-Crystalline Solids* 2019; 505: 279–285.

[207] Denisov A, Dubrovskii V, Solovyov V. Radiation resistance of mineral and polymer construction materials. *ZAO MEI Publishing House*.

[208] Morse JW, Arvidson RS. The dissolution kinetics of major sedimentary carbonate minerals. *Earth-Science Reviews* 2002; 58: 51–84.

[209] Hales B, Emerson S. Evidence in support of first-order dissolution kinetics of calcite in seawater. *Earth and Planetary Science Letters* 1997; 148: 317–327.

[210] Schnoor JL, Stumm W. The role of chemical weathering in the neutralization of acidic deposition. *Schweiz Z Hydrol* 1986; 48: 171–195.

[211] Xia C, Cai Y, Ma Y, et al. Natural mineral-based solid oxide fuel cell with heterogeneous nanocomposite derived from hematite and rare-earth minerals. *ACS Applied Materials & Interfaces* 2016; 8: 20748–20755.

[212] López-Vizcaíno R, dos Santos EV, Yustres A, et al. Calcite buffer effects in electrokinetic remediation of clopyralid-polluted soils. *Separation and Purification Technology* 2019; 212: 376–387.

[213] Mishra SK. The electrokinetics of apatite and calcite in inorganic electrolyte environment. *International Journal of Mineral Processing* 1978; 5: 69–83.

[214] Amankonah JO, Somasundaran P. Effects of dissolved mineral species on the electrokinetic behavior of calcite and apatite. *Colloids and Surfaces* 1985; 15: 335–353.

[215] Sjöberg EL, Rickard DT. Temperature dependence of calcite dissolution kinetics between 1 and 62°C at pH 2.7 to 8.4 in aqueous solutions. *Geochimica et Cosmochimica Acta* 1984; 48: 485–493.

[216] Alkattan M, Oelkers EH, Dandurand J-L, et al. An experimental study of calcite and limestone dissolution rates as a function of pH from −1 to 3 and temperature from 25 to 80°C. *Chemical Geology* 1998; 151: 199–214.

[217] Teng HH. Controls by saturation state on etch pit formation during calcite dissolution. *Geochimica et Cosmochimica Acta* 2004; 68: 253–262.

[218] Nierode DE, Williams BB. Characteristics of acid reaction in limestone formations. *Society of Petroleum Engineers Journal* 1971; 11: 406–418.

[219] Berner RA, Morse JW. Dissolution kinetics of calcium carbonate in sea water; IV, Theory of calcite dissolution. *American Journal of Science* 1974; 274: 108–134.

[220] Plummer LN, Busenberg E. The kinetics of dissolution of dolomite in CO2-H2O systems at 1.5 to 65 degrees C and 0 to 1atm pCO2, evaluation of the aqueous model for the system CaCO3-CO2-H2O. *American Journal of Science* 1982; 282: 45–78.

[221] Jones CE, Unwin PR, Macpherson JV. In situ observation of the surface processes involved in dissolution from the cleavage surface of calcite in aqueous solution using combined scanning electrochemical–atomic force microscopy (SECM-AFM). *ChemPhysChem* 2003; 4: 139–146.

[222] McGeouch C-A, Peruffo M, Edwards MA, et al. Quantitative localized proton-promoted dissolution kinetics of calcite using scanning electrochemical microscopy (SECM). *The Journal of Physical Chemistry C* 2012; 116: 14892–14899.

[223] Barton P, Vatanatham T. Kinetics of limestone neutralization of acid waters. *Environmental Science & Technology* 1976; 10: 262-266.

[224] Rickard D, Sjoeberg EL. Mixed kinetic control of calcite dissolution rates. *American Journal of Science* 1983; 283: 815–830.

[225] Zhao C, Yang C. Advances in electrokinetics and their applications in micro/nano fluidics. *Microfluidics and Nanofluidics* 2012; 13: 179–203.

[226] Delgado AV, González-Caballero F, Hunter RJ, et al. Measurement and interpretation of electrokinetic phenomena. *Journal of Colloid and Interface Science* 2007; 309: 194–224.

[227] Blake RE, Walter LM. Kinetics of feldspar and quartz dissolution at 70–80°C and near-neutral pH: effects of organic acids and NaCl. *Geochimica et Cosmochimica Acta* 1999; 63: 2043–2059.

[228] Kirby BJ. *Micro- and Nanoscale Fluid Mechanics: Transport in Microfluidic Devices*. Cambridge University Press, 2010.

[229] Edward JT. Molecular volumes and the Stokes-Einstein equation. *Journal of Chemical Education* 1970; 47: 261.

[230] https://www.wardsci.com/store/.

[231] https://www.beckmancoulter.com/.

[232] https://www.ameteksi.com/brands/princetonappliedresearch.

[233] https://www.chinstruments.com/.

[234] https://www.polyscience.com/.

[235] http://www.perkinelmer.com/.

[236] Buhmann D, Dreybrodt W. Calcite dissolution kinetics in the system H2O□CO2□CaCO3 with participation of foreign ions. *Chemical Geology* 1987; 64: 89–102.

[237] Berner RA, Principles of chemical sedimentology, McGraw-Hill (1971).

[238] Al Mahrouqi D, Vinogradov J, Jackson MD. Zeta potential of artificial and natural calcite in aqueous solution. *Advances in Colloid and Interface Science* 2017; 240: 60–76.

[239] Mahrouqi DA, Vinogradov J, Jackson MD. Temperature dependence of the zeta potential in intact natural carbonates. *Geophysical Research Letters* 2016; 43: 11,578-11,587.

[240] Moulin P, Roques H. Zeta potential measurement of calcium carbonate. *Journal of Colloid and Interface Science* 2003; 261: 115–126.

[241] Coday BD, Luxbacher T, Childress AE, et al. Indirect determination of zeta potential at high ionic strength: Specific application to semipermeable polymeric membranes - ScienceDirect. *Journal of Membrane Science* 2015; 478: 58–64.

[242] Stipp SLS. Toward a conceptual model of the calcite surface: hydration, hydrolysis, and surface potential. *Geochimica et Cosmochimica Acta* 1999; 63: 3121–3131.

[243] Jaafar MZ, Vinogradov J, Jackson MD. Measurement of streaming potential coupling coefficient in sandstones saturated with high salinity NaCl brine. *Geophysical Research Letters*; 36.

[244] Freitas C, Müller RH. Effect of light and temperature on zeta potential and physical stability in solid lipid nanoparticle (SLN^{TM}) dispersions. *International Journal of Pharmaceutics* 1998; 168: 221–229.

[245] Marsalek R. Particle Size and Zeta Potential of ZnO. *APCBEE Procedia* 2014; 9: 13–17.

[246] Bazant MZ, Kilic MS, Storey BD, et al. Towards an understanding of induced-charge electrokinetics at large applied voltages in concentrated solutions. *Advances in Colloid and Interface Science* 2009; 152: 48–88.

[247] Siffert D, Fimbel P. Parameters affecting the sign and magnitude of the eletrokinetic potential of calcite. *Colloids and Surfaces* 1984; 11: 377–389.

[248] Brantley SL. Kinetics of Mineral Dissolution. In: Brantley SL, Kubicki JD, White AF (eds) *Kinetics of Water-Rock Interaction*. New York, NY: Springer New York, pp. 151–210.

[249] Plummer LN, Wigley TML. The dissolution of calcite in CO2-saturated solutions at 25°C and 1 atmosphere total pressure. *Geochimica et Cosmochimica Acta* 1976; 40: 191–202.

[250] Chou L, Garrels RM, Wollast R. Comparative study of the kinetics and mechanisms of dissolution of carbonate minerals. *Chemical Geology* 1989; 78: 269–282.

[251] Sjöberg EL. A fundamental equation for calcite dissolution kinetics. *Geochimica et Cosmochimica Acta* 1976; 40: 441–447.

[252] Ozbek H, Fair JA, Phillips SL. Viscosity of Aqueous Sodium Chloride Solutions from 0 - 150? C, Lawrence Berkeley National Laboratory 2010. .

[253] Ellis AJ. The solubility of calcite in carbon dioxide solutions. *American Journal of Science* 1959; 257: 354–365.

[254] Plummer LN, Busenberg E. The solubilities of calcite, aragonite and vaterite in CO2H2O solutions between 0 and 9O”C, and an evaluation of the aqueous model for the system CaC03-CO2-H20. *Geochimica et Cosmochimica Acta* 1982; 6: 1011-1040.

[255] Menzinger M, Wolfgang R. The Meaning and Use of the Arrhenius Activation Energy. *Angewandte Chemie International Edition in English* 1969; 8: 438–444.